Transverse Momentum Dependent Parton Distribution Functions from Twisted Mass Lattice QCD

Dissertation
zur
Erlangung des Doktorgrades (Dr. rer. nat.)
der
Mathematisch-Naturwissenschaftlichen Fakultät
der
Rheinischen Friedrich-Wilhelms-Universität Bonn

von
Aniket Sen
aus
Kolkata, India

Bonn, 2024

Angefertigt mit Genehmigung der Mathematisch-Naturwissenschaftlichen Fakultät der Rheinischen Friedrich-Wilhelms-Universität Bonn

Gutachter/Betreuer:	Prof. Dr. Carsten Urbach
Gutachter:	Prof. Dr. Thomas Luu
Tag der Promotion:	27.01.2025
Erscheinungsjahr:	2025

Acknowledgements

First and foremost, I have to thank my supervisors Carsten Urbach and Fernanda Steffens. This work would not be possible without their constant support and guidance. I am immensely grateful to Carsten for giving me the opportunity to pursue my doctoral studies in lattice QCD and also giving me the freedom to explore other areas of research that I find interesting. I owe a great thanks to Fernanda, the principal investigator of my project, for guiding me at every step of the way and for always being there for countless fruitful discussions.

I am thankful to my collaborators in this project: Constantia Alexandrou, Martha Constantinou, Krzysztof Cichy, Gregoris Spanoudes and Simone Bacchio. I have learned a lot from all of them and have found our regular meetings to be extremely helpful. A special thanks to my collaborator and fellow doctoral student Jacopo Tarello for constantly cross checking my results. This research was performed within the Extended Twisted Mass Collaboration (ETMC) and I am profoundly thankful to all the ETMC members for providing the necessary gauge configurations used in this work.

I am thankful to the NSFC and the Deutsche Forschungsgemeinschaft (DFG) for funding this research through the Sino-German Collaborative Research Center TRR110 “Symmetries and the Emergence of Structure in QCD”. I am also thankful for the necessary computing resources provided by the John von Neumann-Institute for Computing on the Juwels booster system at the research center in Juelich, under the project with id TMDPDF1; the High Performance Computing Facility at The Cyprus Institute on the Cyclone cluster, under the project with id p146 and the High Performance Computing and Analytics Lab of the University of Bonn on the Marvin cluster.

Contents

CHAPTER 1

Introduction

Physics is the study of nature. It studies how nature works and in particular the dynamics of matter and energy and their interactions. One of the most fundamental questions that physics tries to answer is the question of what nature is made of. What is the building block of all matter that constitutes our universe?

The idea that all matter is made of some fundamental building blocks, can be traced back to the ancient Greeks around 500 BC, when Leucippus of Miletus and Democritus of Abdera (and later Epicurus) founded the atomist school [1]. In a purely philosophical endeavor, without any experimental evidence, they proposed that all matter is made of indivisible and indestructible atoms. This idea was rejected by Aristotle and the school of Athens in favour of a continuous theory of matter, since the former required a void between atoms which could not be explained at the time.

The concept of matter being made of tiny particles made a resurgence in the 17th century when in 1687 Newton showed that Boyle's law (product of pressure and volume of a gas is constant at constant temperature) could only be explained if one assumes that gas is made of tiny particles [2]. A major theoretical breakthrough followed in 1808 when Dalton proposed that all elements consist of identical atoms [3] and in 1811 when Avogadro suggested that smallest parts of matter may consist of two or more atoms stuck together, which he called molecules [4]. By the end of the 19th century, a lot of progress had been made in the atomic and molecular theory of matter.

Atomic and molecular theory, however, did not answer all questions about the nature of matter. one in particular was the existence of positive and negatively charged matter, which Faraday termed as ions [5]. The existence of something more fundamental than atoms was first found by Thomson in 1897 when he discovered the electron [6]. He found that these charge carrying particles were about 1400 times lighter than the lightest atom. This discovery led him to propose a model of the atom as a positively charged sphere with electrons embedded in it, which he called the plum pudding model. The next big leap in understanding atomic structure came in 1911 when Rutherford discovered the nucleus with his famous gold foil experiment [7]. This resulted in Rutherford's model of the atom where the atom consists of a small, heavy and positively charged nucleus surrounded by a cloud of negatively charged electrons. This followed the atomic model of Bohr in 1913 by proposing quantized shells which explained the stable orbit of electrons around the nucleus [8]. Future formulation of quantum mechanics provided a strong theoretical foundation for the atomic model.

On the other hand, the question of most fundamental building block at the time meant understanding the nucleus itself. Although protons were already observed in 1898 by Wien and in 1910 by Thomson,

it was Rutherford who in 1919 first identified the hydrogen nucleus as an elementary particle and named it proton [9]. While this solved the problem of charge neutrality of the atom, it raised more questions about the nature of the nucleus. One major question was that the next lightest atom (Helium) had a mass 4 times that of hydrogen, while containing only 2 electrons (which meant 2 protons). The problem compounded as one moved to heavier elements. This was solved by the discovery of the neutron by Chadwick in 1932 [10]. The neutron was found to be a neutral particle with mass similar to that of the proton.

The discovery of the proton and neutron as building blocks of the nucleus led to further questions. Chiefly among them were the questions of what binds the protons and neutrons together in the nucleus and what is the structure of the protons and neutrons themselves. The answer to the first question was first proposed by Yukawa in 1935 who suggested the existence of a new short-range force mediated by massive particles which he called mesons [11]. This answer was confirmed by the discovery of the pion in 1947 [12, 13]. The following decade saw the discovery of many different particles, which led to the development of the eight-fold way by Gell-Mann and Ne'eman in 1961 [14, 15]. This described the newly discovered mesons and baryons in terms of multiplets of flavour SU(3). This was the first step towards answering the second question of the structure of protons and neutrons. By 1964, Gell-Mann and Zweig independently proposed the quark model of hadrons [16, 17] which proposed that mesons are bound states of a quark-antiquark pair and baryons are bound states of three quarks. The original quark model could not explain existence of particles such as the $\Delta^{++}(1232)$ which has a symmetric structure of three up quarks, which can not be allowed for fermions. This was solved by the introduction of a new quantum number called color by Greenberg in 1964 [18]. Setting the number of different colors to 3, the quark model was able to explain all the observed hadrons. This led to the foundation of Quantum Chromodynamics (QCD) which is the theory that governs the dynamics and interactions of all particles with color charge.

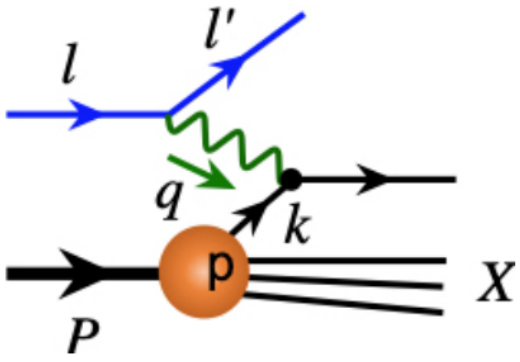

Figure 1.1: Deep inelastic scattering of an electron off a proton. The figure is taken from [19].

Experimental investigation of internal structure of nucleons began as early as the 1950s with the determination of finite size of the proton [20, 21]. In the 1960s, the first experimental evidence of quarks within nucleons was found from the deep inelastic scattering events observed at the Stanford Linear Accelerator Center (SLAC) [22]. In this electron-proton scattering ($e(l) + p(P) \rightarrow e(l') + X$) experiment, as sketched in Figure 1.1, the momentum of the scattered electron l' is observed, which then defines the momentum transfer $q = l - l'$. Assuming $Q \equiv \sqrt{-q^2} \gg 1/R$, where R is the radius of

the proton, DIS provides a short-distance probe of the nucleon structure. Also, since the effective size of the collision is $\sim O(1/Q) \ll R$, the cross-section of the process is dominated by the scattering of a single point-like particle, as the probability of scattering n particles is suppressed by $\sim O(1/(Q^n R^n))$. If we denote the momentum of this point-like particle as $k \approx \xi P \sim Q$ in terms of the momentum fraction ξ, the cross-section can be factorized into a hard scattering partonic cross-section and a parton distribution function (PDF). Let $f_{i/p}(\xi)$ denote the PDF, which is a probability distribution of finding a type i point-like particle inside the proton carrying a momentum fraction ξ. The DIS cross-section can then be expressed as [19]

$$\begin{aligned} E' \frac{d\sigma_{ep\to eX}}{d^3 l'} &\approx \sum_i \int d\xi f_{i/p}(\xi) E' \frac{d\hat{\sigma}_{ep\to eX}}{d^3 l'} \\ &= \sum_i e_i^2 \left\{ \frac{2\alpha^2}{Q^2 s} \left[\frac{1 + (1-y^2)}{y^2} \right] \right\} f_{i/p}(x) \end{aligned} \tag{1.1}$$

where $E' d\hat{\sigma}_{ep\to eX}$ is the partonic cross-section, $\alpha = e^2/4\pi$ is the fine structure constant, $s = (P + l)^2$ is the center of mass energy squared, $y = P \cdot q / P \cdot l$ is the inelasticity of the process, and e_i is the fractional charge of the particle type i. $x = Q^2/(2P \cdot q)$ is the Bjorken variable. This is the factorization of the DIS cross-section in terms of the partonic model as proposed by Feynman in 1969 [23].

Since the PDF averages over all degrees of freedom except the longitudinal momentum fraction, it provides a one-dimensional (1-D) picture of the nucleon structure. There are certain important aspects of the nucleon structure that require a three-dimensional (3-D) picture. One such aspect is the so-called "spin puzzle", which describes the discrepancy of the quark contribution to the nucleon spin as measured in polarized deep inelastic scattering and predictions from the quark model. This was first discovered by the European Muon Collaboration (EMC) in 1988 [24]. Later experiments showed that a large contribution comes from the angular momentum of the partons [25]. A full understanding of the orbital angular motion of partons inside nucleons can only be obtained by studying the 3-D structure of the nucleon.

The most general way to describe the nuclear structure is through the Wigner distributions $\rho(x, \boldsymbol{k}_\perp, \boldsymbol{b}_\perp)$. These are 5-dimensional functions that depend on the longitudinal momentum fraction x, transverse momentum component $\boldsymbol{k}_\perp$ and the transverse position $\boldsymbol{b}_\perp$ of the partons inside the nucleon. Since these depend on both $\boldsymbol{k}_\perp$ and $\boldsymbol{b}_\perp$ simultaneously, there exists no observable that can provide a direct experimental measurement of these distributions. So to arrive at some measurable quantities, one has to integrate over one these degrees of freedom. Integrating over the transverse momentum leads to the generalized parton distributions (GPDs), and integrating over the transverse position leads to the transverse momentum dependent distributions (TMDs). These are the two most general distribution functions that encode the 3-D structure of the nucleon. In Figure 1.2, we show the relation between the different parton distribution functions.

In inclusive DIS experiments, the momentum transfer $Q \gg 1/R$ is so large that the hard probe is not very sensitive to the physics at the scale of $\Lambda_{\mathrm{QCD}} \sim 1/R$ which includes the confined transverse motion (both in $\boldsymbol{k}_\perp$ and $\boldsymbol{b}_\perp$) of the partons [19]. For a 3-D understanding of the nucleon structure, one needs another soft momentum scale Q_s such that $Q_s \ll Q$. One possibility of such a scale is the transverse momentum $P_{h\perp}$ of the final state hadron that is observed in semi-inclusive DIS (SIDIS) experiments ($e(l) + p(P) \to e(l') + h(P_h) + X$). The process is sketched in Figure 1.3. The SIDIS

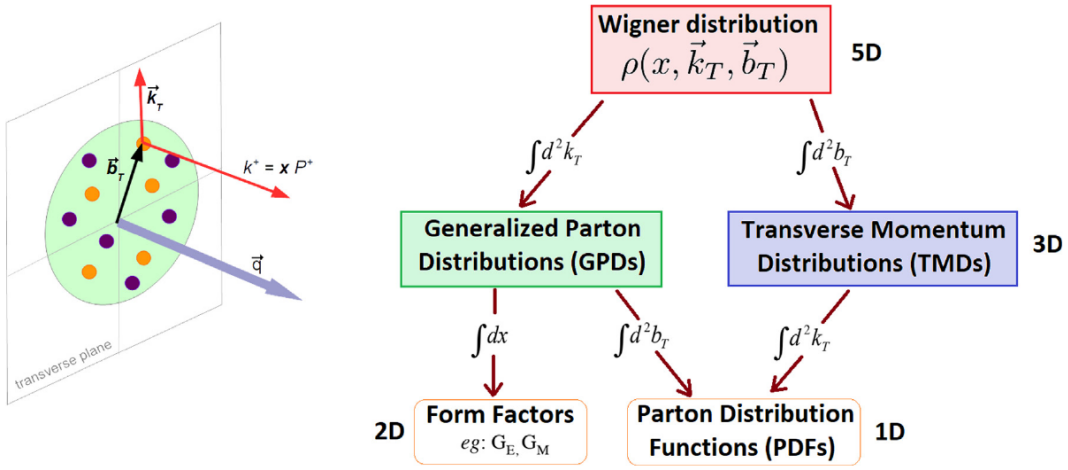

Figure 1.2: Experimental access to the 3D structure via GPDs and TMDs and their relation to form factors and PDFs. The figure is taken from [26].

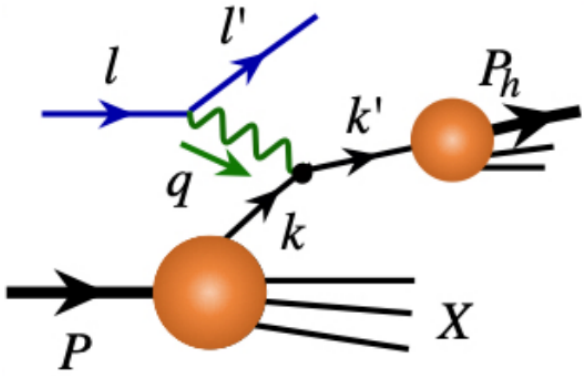

Figure 1.3: Semi-inclusive deep inelastic scattering of an electron off a proton. The figure is taken from [19].

cross-section can be factorized as [19]

$$E' E_h \frac{d\sigma_{ep\to ehX}}{d^3 l' d^3 P_h} \approx f_1 \otimes D_{h/q} \otimes \hat{\sigma} \tag{1.2}$$

where $f_1(\xi, k_\perp)$ are the transverse momentum dependent parton distribution functions (TMDPDFs) and $D_{h/q}(\zeta, k'_\perp)$ are the transverse momentum dependent fragmentation functions (TMDFFs). TMDFFs describe the hadronization of a quark of flavour q into the final observed hadron h carrying a momentum fraction ζ of the fragmenting quark momentum. Similar to collinear PDFs, TMDPDFs describe the probability of finding a parton with a longitudinal momentum fraction ξ and a transverse momentum $\boldsymbol{k}_\perp$ inside the nucleon. Based on the polarization of the quark and the colliding nucleon, there are 8 possible TMDPDFs. These are summarized in Figure 1.4. TMDPDFs can also be extracted from Drell-Yan (DY) processes, however it is more difficult to disentangle the different TMDs as listed

in Figure 1.4 from DY processes alone.

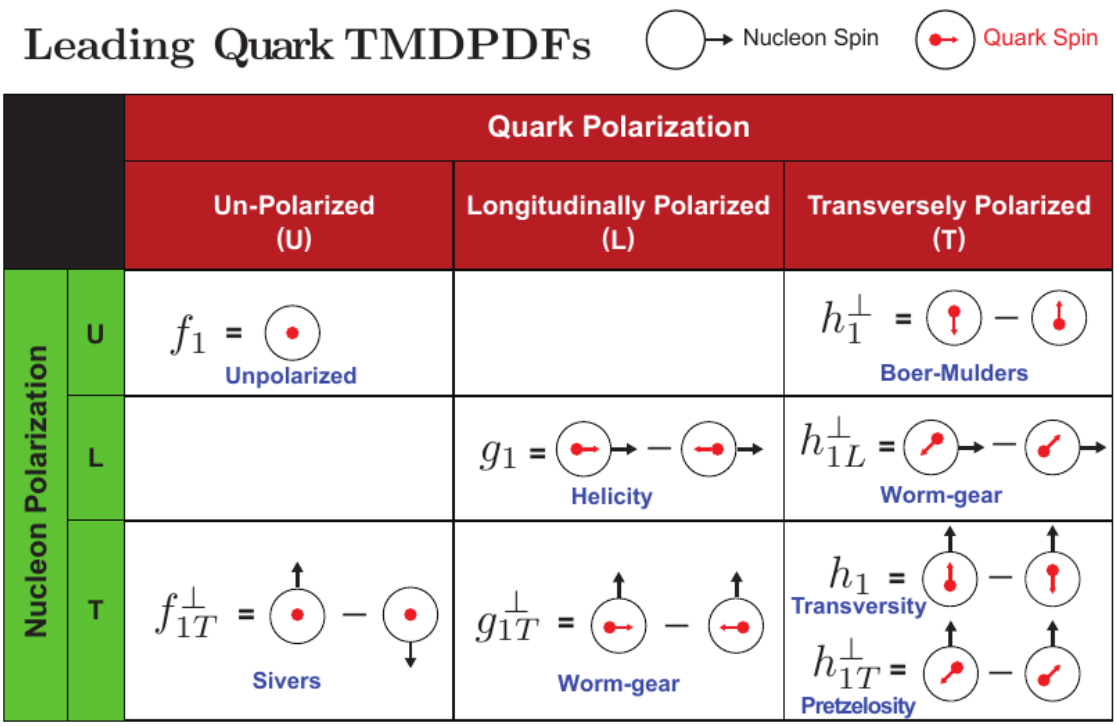

Figure 1.4: Leading power spin dependent quark TMDPDFs. The figure is taken from [19].

TMDPDFs can be obtained through phenomenological studies using data from experiments such as HERMES [27] and COMPASS [28]. In recent years, there have been several studies that have extracted TMDPDFs from global fits to existing data [29–33]. However the results from these studies have notable discrepancies between them despite using a similar dataset. The precision of these extractions are also not as good as in the case of collinear PDFs. This is expected to improve with future data from existing experiments and in particular the future Electron-Ion Collider (EIC) [34]. A theoretical calculation of TMDPDFs will provide a crucial input to future global fit studies for a more precise determination of the internal structure of nucleons.

A direct theoretical determination of TMDPDFs however is a challenging task. The internal strong dynamics of QCD takes place at the scale of $1/R \sim 200\,\text{MeV} \sim \Lambda_{\text{QCD}}$. At such large distances, QCD is strongly nonperturbative. Hence for a calculation of TMDPDFs in QCD, one needs a nonperturbative approach. Historically, the most successful nonperturbative approach to QCD has been lattice QCD. This was first proposed by Wilson in 1974 [35] and has since then been used to calculate many properties of hadrons. A brief overview of lattice QCD is given in Chapter 2. However, all kinds of parton distributions have been inaccessible in lattice QCD due to the correlators being defined on the light-cone. For a long time most lattice QCD studies of parton physics were limited to $\langle x^n \rangle$ weighted Mellin moments of the PDFs. And for TMDPDFs, they were limited to ratios of moments of TMDPDFs [36–38]. Over the years, various approaches have been proposed and investigated to tackle this problem [39–45]. In the last decade, the development of the large momentum effective theory (LaMET) [46, 47] has resulted in a new wave of studies to calculate partonic physics observables on

the lattice through the quasi-PDF approach. This has also stimulated other approaches such as the pseudo-PDFs [48, 49], the hadronic tensor method [40, 50], good lattice cross sections method [51, 52] etc.

In recent years, there have been several theoretical developments that have provided a framework for calculating TMDPDFs on the lattice using LaMET [53–61]. Under the LaMET framework, the TMDPDFs can be calculated by first computing the quasi-TMDPDFs on the lattice and then matching them to the physical TMDPDFs using perturbation theory. The matching takes the following form [62]

$$f^{TMD}(x,b,\mu,\zeta) = H_f(\frac{\zeta_z}{\mu^2})\, e^{-\ln\left(\frac{\zeta_z}{\zeta}\right)K(b,\mu)}\, S_r^{\frac{1}{2}}(b,\mu)\, \tilde{f}(x,b,\mu,\zeta_z) + O\left(\frac{\Lambda_{QCD}}{\zeta_z}, \frac{M^2}{(P^z)^2}, \frac{1}{b^2\zeta_z}\right) \tag{1.3}$$

This equation will be discussed in more detail in Chapter 3. The key componets are the light-cone TMDPDF $f^{TMD}(x,b,\mu,\zeta)$ (in position space), the quasi-TMDPDF $\tilde{f}(x,b,\mu,\zeta_z)$, the Collins-Soper kernel $K(b,\mu)$, the soft function $S_r(b,\mu)$ and the hard kernel $H_f(\zeta_z/\mu^2)$. The aim of this work is the calculation of the right hand side of the above equation in order to obtain f^{TMD}. Only the hard kernel can be calculated perturbatively. The quasi-TMDPDF, the Collins-Soper kernel and the soft function have to be calculated nonperturbatively on the lattice. In recent years, there have been several calculations of soft function [63–65] and the Collins-Soper kernel [55, 57, 66–71]. And only very recently, a first calculation of the full TMDPDF on the lattice has been presented [72]. In this work, we present an exploratory calculation of the unpolarized TMDPDFs by calculating the individual components of the matching equation, i.e. the quasi-TMDPDF, the Collins-Soper kernel and the soft function, and perform a 1-loop matching to the light-cone TMDPDF. The renormalization of these observables, which contain a staple-shaped Wilson line, is also more involved than the straight Wilson line in the case of quasi-PDFs. Several studies have been performed for the nonperturbative renormalization of the staple-shaped Wilson line on the lattice [66, 73]. In this work, we also perform a study of the renormalization of the staple-shaped Wilson line, which has been published in [74].

The dissertation is organized as follows. In Chapter 2 we briefly describe the lattice QCD formalism. In Chapter 3 we derive a simple definition of unpolarized TMDPDFs from the SIDIS process. We also describe the LaMET framework and the calculation of the TMDPDFs using this framework. In Chapter 4 we describe the nonperturbative renormalization of the quasi-TMDPDFs. In Chapter 5 we describe the lattice ensembles used in this work and all the technical details of calculating the required observables on the lattice. In Chapter 6 we present the results of our calculation and compare them to the existing literature. In Chapter 7 we summarize our work and give an outlook for future work.

CHAPTER 2

Lattice QCD

In this chapter, we will briefly discuss the concepts of Lattice QCD. This chapter is based on a similar chapter from the master thesis of the author [75] which in turn followed the formulation by Gattringer and Lang [76].

2.1 Continuum QCD

2.1.1 The QCD Action

Quantum Chromodynamics is the theory of strong interactions. A theory of fermionic fields that carry a color charge. These fermions are called quarks. Since we observe $N_c = 3$ color charges, QCD is an SU(3) gauge theory. The corresponding gauge bosons are called gluons. These are defined via the 8 generators of SU(3), namely the Gell-Mann matrices. Assuming that the reader is familiar with the quantum field theoretical approach, we define the QCD action as

$$S_{QCD}\left[\psi, \bar{\psi}, A\right] = S_F\left[\psi, \bar{\psi}, A\right] + S_G\left[A\right], \tag{2.1}$$

where S_F is the fermionic part of the action, and S_G is the pure gauge action. The field ψ denotes the fermion field. The conjugate field is defined as $\bar{\psi} = \psi^\dagger \gamma_0$, where γ_0 is the time-related Dirac gamma matrix. Conventions used for these gamma matrices are given in Appendix A. The fermions are described as Dirac-4 spinors $\psi^{(f)}(x)_{\substack{\alpha \\ a}}$. x denotes the spacetime position of the field. $\alpha = 0, 1, 2, 3$ are the Dirac spinor indices. $a = 0, 1, 2$ gives the color index. We will be denoting the Dirac indices with Greek letters and color indices with Roman letters. The fermion also carries a flavor index f, which corresponds to one of the 6 flavors of quarks - up, down, strange, charm, bottom and top. Quite often we work with only the light quarks, and hence only consider $N_f < 6$ flavors. The fields $A_\mu(x)_{cd}$ are the gauge fields with a Lorentz index μ and two color indices. As mentioned earlier, $A_\mu(x)$ are generators of SU(3), and hence are traceless, hermitian 3×3 matrix at each spacetime point x and Lorentz component μ.

The fermionic part of the QCD action is defined as

$$\begin{aligned} S_F\left[\psi,\bar{\psi},A\right] &= \sum_{f=1}^{N_f}\int d^4x\,\bar{\psi}^{(f)}(x)\left(\gamma_\mu(\partial_\mu + iA_\mu(x)) + m^f\right)\psi^{(f)}(x) \\ &= \sum_{f=1}^{N_f}\int d^4x\,\bar{\psi}^{(f)}(x)_{\;c}^{\alpha}\left((\gamma_\mu)_{\alpha\beta}(\delta_{cd}\partial_\mu + iA_\mu(x)_{cd}) + m^{(f)}\delta_{\alpha\beta}\delta_{cd}\right)\psi^{(f)}(x)_{\;d}^{\beta}. \end{aligned} \tag{2.2}$$

Einstein summation convention is assumed for expressions with explicit indices. The mass term $m^{(f)}$ is the mass of the quark flavor f. The γ_μ are the Dirac gamma matrices. We can define the covariant derivative as

$$D_\mu(x) = \partial_\mu + iA_\mu(x). \tag{2.3}$$

In terms of the covariant derivative, one can define the field strength tensor $F_{\mu\nu}(x)$ of the gluons as

$$F_{\mu\nu}(x) = -i\left[D_\mu(x), D_\nu(x)\right] = \partial_\mu A_\nu(x) - \partial_\nu A_\mu(x) + i\left[A_\mu(x), A_\nu(x)\right]. \tag{2.4}$$

Since $SU(3)$ is non-abelian, the last term on the right hand side does not vanish. From the field strength tensor, we can write down the pure gauge action as

$$S_G\left[A\right] = \frac{1}{2g^2}\int d^4x\,tr\left[F^{\mu\nu}(x)F_{\mu\nu}(x)\right], \tag{2.5}$$

where g is the QCD coupling constant.

2.1.2 Gauge Invariance of the QCD Action

Gauge invariance is a fundamental symmetry of QCD. Since QCD has $N_c = 3$ colors, we observe $SU(3)$ gauge symmetry. For this symmetry to hold, the QCD action must be invariant under $SU(3)$ transformations. For any general $\Omega(x) \in SU(3)$, the fermion fields transform as

$$\psi(x) \to \psi'(x) = \Omega(x)\psi(x)\ ,\ \bar{\psi} \to \bar{\psi}'(x) = \bar{\psi}(x)\Omega(x)^\dagger. \tag{2.6}$$

Assuming that the gauge field transforms as $A_\mu(x) \to A'_\mu(x)$, we find the fermionic part of the QCD action transforms to

$$S_F\left[\psi',\bar{\psi}',A'\right] = \int d^4x\,\bar{\psi}(x)\Omega(x)^\dagger\left(\gamma^\mu(\partial_\mu + iA'_\mu(x)) + m\right)\Omega(x)\psi(x). \tag{2.7}$$

Now, for gauge invariance, we require

$$S_F\left[\psi',\bar{\psi}',A'\right] = S_F\left[\psi,\bar{\psi},A\right]. \tag{2.8}$$

Comparing equation 2.2 and 2.7, we see that the mass term does not change. But the covariant derivative term implies

$$\begin{aligned}\partial_\mu + iA_\mu(x) &= \Omega(x)^\dagger \left(\partial_\mu + iA'_\mu(x)\right)\Omega(x) \\ &= \partial_\mu + \Omega(x)^\dagger(\partial_\mu\Omega(x)) + i\Omega(x)^\dagger A'_\mu(x)\Omega(x).\end{aligned} \tag{2.9}$$

For the equality to hold, the gauge field must transform as

$$A_\mu(x) \to A'_\mu(x) = \Omega(x)A_\mu(x)\Omega(x)^\dagger + i(\partial_\mu\Omega(x))\Omega(x)^\dagger. \tag{2.10}$$

We notice that since $A'_\mu(x)$ is also hermitian and traceless, it satisfies the properties for the gauge field. The transformation of the field strength tensor then takes the following form,

$$F_{\mu\nu}(x) \to F'_{\mu\nu}(x) = \Omega(x)F_{\mu\nu}(x)\Omega(x)^\dagger. \tag{2.11}$$

It is straightforward to show that the gauge action as shown in equation 2.5 is invariant under the given transformation of $F_{\mu\nu}$.

2.1.3 Path Integral Formalism

To introduce the path integral formalism as is used in the field theory, let us first consider a simple quantum mechanical system with the transition matrix

$$\langle x', t'|x, t\rangle = \langle x'|e^{-iH(t'-t)}|x\rangle, \tag{2.12}$$

where H is the hamiltonian of the system. Now if we divide the time interval $(t' - t)$ into $n + 1$ equal parts of length ϵ then using completeness relation $\int dx_j\ |x_j, t_j\rangle\langle x_j, t_j| = 1$, we can write the transition matrix as

$$\langle x', t'|x, t\rangle = \lim_{n\to\infty} \prod_{i,j=0}^{n} \int dx_i \langle x_{j+1}, t_{j+1}|x_j, t_j\rangle. \tag{2.13}$$

Let us assume that the Hamiltonian H has the simple form

$$H = \frac{p^2}{2m} + V(x), \tag{2.14}$$

where p is the momentum operator and $V(x)$ is the potential. Using the completeness relation for the momentum ($\int \frac{dp_j}{2\pi}|p_j\rangle\langle p_j| = 1$), we obtain for a short interval ϵ

$$\begin{aligned}\langle x_j, t_j|x_{j-1}, t_{j-1}\rangle &= \langle x_j|e^{-i\epsilon H}|x_{j-1}\rangle = \langle x_j|(1 - i\epsilon H)|x_{j-1}\rangle + O(\epsilon^2) \\ &= \int \frac{dp_j}{2\pi} e^{ip_j(x_j - x_{j-1}) - i\epsilon H(p_j, x_{j-1})} + O(\epsilon^2).\end{aligned} \tag{2.15}$$

Substituting this back into equation 2.13, we get

$$\begin{aligned}\langle x', t'|x, t\rangle &= \lim_{n\to\infty} \int \left(\prod_{j=1}^{n} dx_j\right) \int \left(\prod_{j=1}^{n+1} \frac{dp_j}{2\pi}\right) \exp\left(i \sum_{j=1}^{n+1} (p_j(x_j - x_{j-1}) - H(p_j, x_{j-1})\epsilon)\right) \\ &= \mathcal{N} \lim_{n\to\infty} \int \left(\prod_{j=1}^{n} dx_j\right) \exp\left(i \sum_{j=1}^{n+1} \left(\frac{(x_j - x_{j-1})^2 m}{2\epsilon} - V(x_{j-1})\right)\right) \\ &= \mathcal{N} \int \mathcal{D}x \ \exp\left(i \int_t^{t'} d\tau \left(\frac{\dot{x}^2 m}{2} - V(x)\right)\right) = \mathcal{N} \int \mathcal{D}x \ \exp(iS[x]),\end{aligned} \tag{2.16}$$

where we have used $\int \frac{dp_j}{2\pi} \exp\left(i(p_j \Delta x - \frac{\epsilon p_j^2}{2m})\right) = \sqrt{2\pi \frac{m}{\epsilon}} \exp\left(\frac{\Delta x^2 m}{2\epsilon}\right)$ and we have defined $\mathcal{D}x \equiv \prod_j dx_j$. And finally, $\mathcal{N}$ is a normalization constant.

Generaizing this to more degrees of freedom, and in particular to infinite degrees of freedom, we reach the field theory equivalent. The derivation follows accordingly. For a field ϕ, we have the completenenss relation as $\int \mathcal{D}\phi |\phi\rangle\langle\phi| = 1$. And then analogous to the simple quantum mechanical case, we obtain the transition matrix

$$\langle \phi_b | \phi_a \rangle = \mathcal{N} \int \mathcal{D}\phi \ \exp(iS[\phi]). \tag{2.17}$$

With this formalism, the expectation of any physical observable O, can be written as

$$\langle O \rangle = \langle \Omega | O | \Omega \rangle = \frac{\int \mathcal{D}\phi \ O[\phi] \ \exp(iS[\phi])}{\int \mathcal{D}\phi \ \exp(iS[\phi])}, \tag{2.18}$$

where the denominator is called the partition function and is denoted by Z. The state $|\Omega\rangle$ here denotes the vacuum. In order to calculate correlators, we also need the idea of generating functionals. This is created from the partition function, by adding an external source $J(x)$.

$$W[J] = \int \mathcal{D}\phi \ \exp\left(iS[\phi] + i \int d^4x \ J(x)\phi(x)\right). \tag{2.19}$$

Then the expectation of the field $\phi(x)$ is given by

$$\langle \Omega | \phi(x_1) | \Omega \rangle = -\frac{i}{Z} \frac{\delta W[J]}{\delta J(x_1)}\bigg|_{J=0}. \tag{2.20}$$

This idea can be extended for 2-point, 3-point functions and so on depending on the number of fields under consideration. The path integral formalism plays an important role for quantizing the fields on the lattice. The concepts discussed in this section can be used directly on the lattice. The only difference being that one works with Euclidean spacetime on the lattice. And hence one must use Euclidean path integral.

2.2 QCD on the Lattice

2.2.1 Discretizing the Action

For a lattice formulation of the continuum QCD, we need to introduce a 4D lattice. We usually work with hypercubic lattices. We discretize a 4D box by dividing the spatial coordinates into N discrete points and the time coordinate into N_T. Then the lattice Λ can be defined as

$$\Lambda = \left\{ n = (n_1, n_2, n_3, n_4) \mid n_1, n_2, n_3 = 0, 1, ..., N-1; n_4 = 0, 1, ..., N_T - 1 \right\}. \tag{2.21}$$

The vectors $n \in \Lambda$ label the space-time point on the lattice. We ensure that the separation between these lattice points is a constant in all direction. This constant (usually denoted as 'a') is called the lattice spacing. The fermion fields can be defined on these lattice points as

$$\psi(n),\ \bar{\psi}(n),\ n \in \Lambda. \tag{2.22}$$

The fields carry the spin, color and flavor indices similar to the continuum. In order to discretize the action, we also need to define the covariant derivative on the lattice. First, let us discretize the simple partial derivative with a symmetric expression

$$\partial_\mu \psi(x) \rightarrow \frac{1}{2a} \left(\psi(n + \hat{\mu}) - \psi(n - \hat{\mu}) \right), \tag{2.23}$$

where $\hat{\mu}$ is the unit vector in the μ-direction. Now to get to the covariant derivative, we first need to define the gauge fields on the lattice. This can be easily derived from the idea of gauge invariance. In equation 2.6, the transformation of the fermion fields under a $SU(3)$ rotation were defined. On the lattice, it takes an exactly similar form. If we consider a $\Omega(n) \in SU(3)$ defined at each lattice site n, then the fermion fields transform as

$$\psi(n) \rightarrow \psi'(n) = \Omega(n)\psi(n), \qquad \bar{\psi}(n) \rightarrow \bar{\psi}'(n) = \bar{\psi}(n)\Omega(n)^\dagger. \tag{2.24}$$

One immediate observation is that a term like $\bar{\psi}(n)\psi(n + \hat{\mu})$ is not gauge invariant under such transformation. Since the derivative term on the lattice is non-local, we have to ensure that such terms are gauge invariant. However, such non-local terms are also not gauge invariant in the continuum formulation, since

$$\bar{\psi}(x)\psi(y) \rightarrow \bar{\psi}'(x)\psi'(y) = \bar{\psi}(x)\Omega^\dagger(x)\Omega(y)\psi(y). \tag{2.25}$$

But in the continuum, we already know how to make such a term gauge invariant. We introduce a factor known as the Schwinger line integral, which is defined by [77]

$$U(x, y) = e^{i \int_x^y dz_\mu A_\mu(z)}. \tag{2.26}$$

On the lattice then, one can use a similar idea, and discretize this factor as

$$U(x, x + \epsilon) = e^{i \epsilon \cdot A_\mu(x)}. \tag{2.27}$$

Now, we can define a link variable $U_\mu(n)$ that connects the point n and $n+\hat{\mu}$, as

$$U_\mu(n) = e^{iaA_\mu(n)}, \tag{2.28}$$

where $A_\mu(n)$ are the lattice gauge fields. Under $SU(3)$ rotation, the links transform as

$$U_\mu(n) \to U'_\mu(n) = \Omega(n)U_\mu(n)\Omega(n+\hat{\mu})^\dagger. \tag{2.29}$$

Link variables are also directional, and we can define $U_{-\mu}(n)$ as

$$U_{-\mu}(n) \equiv U_\mu(n-\hat{\mu})^\dagger. \tag{2.30}$$

This directionality is explained in Figure 2.1. Note that since A_μ is an element of the lie algebra, U_μ

Figure 2.1: Directionality of the link variables.

is an element of $SU(3)$. With this definition of the link variables, we can (naively) discretize the fermion action as

$$S_F\left[\psi,\bar{\psi},U\right] = a^4 \sum_{n\in\Lambda} \bar{\psi}(n)\left(\sum_{\mu=0}^{3}\gamma_\mu \frac{U_\mu(n)\psi(n+\hat{\mu}) - U_{-\mu}(n)\psi(n-\hat{\mu})}{2a} + m\psi(n)\right) \tag{2.31}$$

It is quite straightforward to show the gauge invariance of this action. To get the gauge action, one needs to define a quantity called plaquette ($U_{\mu\nu}$) as

$$\begin{aligned} U_{\mu\nu}(n) &= U_\mu(n)U_\nu(n+\hat{\mu})U_{-\mu}(n+\hat{\mu}+\hat{\nu})U_{-\nu}(n+\hat{\nu}) \\ &= U_\mu(n)U_\nu(n+\hat{\mu})U_\mu(n+\hat{\nu})^\dagger U_\nu(n)^\dagger. \end{aligned} \tag{2.32}$$

The plaquette is the shortest, nontrivial closed loop on the lattice. Figure 2.2 shows a diagrammatic representation of the plaquette. Using the Taylor expansion of the link variables, we find that

$$U_{\mu\nu}(n) = exp\left(ia^2F_{\mu\nu}(n) + O(a^3)\right). \tag{2.33}$$

The pure gauge action can then be defined following the continuum action as

$$S_G[U] = \frac{2}{g^2}\sum_{n\in\Lambda}\sum_{\mu<\nu} \mathrm{Re}\,\mathrm{tr}\left[\mathbb{1} - U_{\mu\nu}(n)\right]. \tag{2.34}$$

This is known as the Wilson gauge action [35].

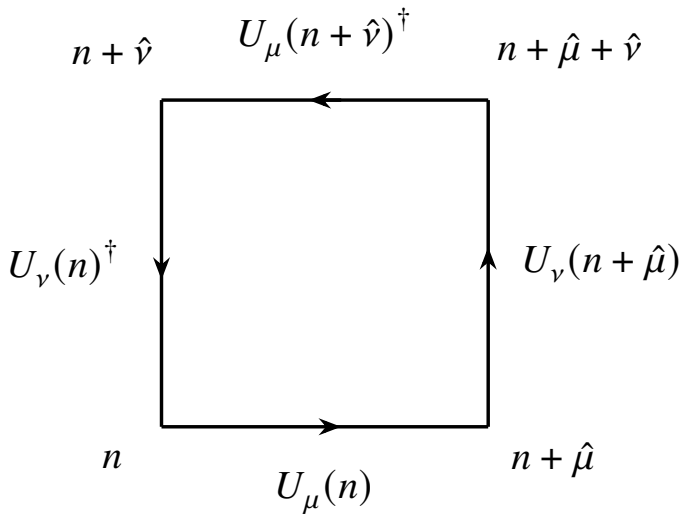

Figure 2.2: Diagrammatic representation of the plaquette $U_{\mu\nu}(n)$.

2.2.2 The Doubling Problem and Wilson Fermion

Let us look at the fermion action that was naively discretized in equation 2.31. Since it is a bilinear in $\bar{\psi}$ and ψ, one can write

$$S_F\left[\psi,\bar{\psi},U\right] = a^4 \sum_{n,m\in\Lambda} \sum_{a,b,\alpha,\beta} \bar{\psi}(n)_{\,a}^{\,\alpha} D(n|m)_{\,ab}^{\,\alpha\beta} \psi(m)_{\,b}^{\,\beta}, \tag{2.35}$$

where the naive Dirac operator D is given by

$$D(n|m)_{\,ab}^{\,\alpha\beta} = \sum_{\mu=0}^{3} (\gamma_\mu)_{\alpha\beta} \frac{1}{2a} \left(U_\mu(n)_{ab} \delta_{n+\hat{\mu},m} - U_{-\mu}(n)_{ab} \delta_{n-\hat{\mu},m} \right) + m\delta_{\alpha\beta}\delta_{ab}\delta_{n,m}. \tag{2.36}$$

Considering only the trivial gauge ($U_\mu = \mathbb{1}\ \forall n \in \Lambda$), we find the Fourier transform of the Dirac operator as

$$\begin{aligned} \tilde{D}(p|q) &= \frac{1}{|\Lambda|} \sum_{n,m\in\Lambda} e^{-ip\cdot na} D(n|m) e^{iq\cdot ma} \\ &= \frac{1}{\Lambda} \sum_{n\in\Lambda} e^{-(p-q)\cdot na} \left(\sum_{\mu=0}^{3} \gamma_\mu \frac{e^{iq_\mu a} - e^{-iq_\mu a}}{2a} + m\mathbb{1} \right) \\ &= \delta(p-q)\tilde{D}(p), \end{aligned} \tag{2.37}$$

where

$$\tilde{D}(p) = m\mathbb{1} + \frac{i}{a} \sum_{\mu=0}^{3} \gamma_\mu \sin(p_\mu a). \tag{2.38}$$

In order to calculate the quark propagator $D^{-1}(n|m)$, one needs to invert $\tilde{D}(p)$ and do an inverse fourier transform. $\tilde{D}^{-1}(p)$ can be calculated as [76]

$$\tilde{D}^{-1}(p) = \frac{m\mathbb{1} - ia^{-1}\sum_\mu \gamma_\mu \sin(p_\mu a)}{m^2 + a^{-2}\sum_\mu \sin^2(p_\mu a)}. \tag{2.39}$$

And finally, performing the inverse Fourier transformation gives,

$$D^{-1}(n|m) = \frac{1}{|\Lambda|}\sum_{p\in\tilde{\Lambda}} \tilde{D}^{-1}(p) e^{ip\cdot(n-m)a}. \tag{2.40}$$

If we consider only the case of the massless fermions ($m = 0$), for a fixed p, we can show that the lattice propagator goes to the correct continuum limit

$$\tilde{D}^{-1}(p)|_{m=0} = \frac{-ia^{-1}\sum_\mu \gamma_\mu \sin(p_\mu a)}{a^{-2}\sum_\mu \sin^2(p_\mu a)} \xrightarrow{a\to 0} \frac{-i\sum_\mu \gamma_\mu p_\mu}{p^2}. \tag{2.41}$$

The last expression has a pole at $p = (0, 0, 0, 0)$, as is expected for a massless fermion in the continuum. On the lattice however, a pole is found whenever all the momentum components are either $p_\mu = 0$ or $p_\mu = \pi/a$. And therefore one gets 15 unphysical poles at

$$p = (\pi/a, 0, 0, 0), (0, \pi/a, 0, 0), ..., (\pi/a, \pi/a, \pi/a, \pi/a). \tag{2.42}$$

These are the so-called fermion doublers. In order to remove them, Wilson suggested a solution by adding an extra term to the momentum space Dirac operator as

$$\tilde{D}(p) = m\mathbb{1} + \frac{i}{a}\sum_{\mu=0}^{3}\gamma_\mu \sin(p_\mu a) + \mathbb{1}\frac{1}{a}\sum_{\mu=0}^{3}(1 - \cos(p_\mu a)). \tag{2.43}$$

This extra term is called the Wilson term. For components with $p_\mu = 0$, it simply vanishes. For each component with $p_\mu = \pi/a$, it provides a contribution of $2/a$. Hence it essentially acts as an additional mass term, and the total mass of the doublers become $m + 2\ell/a$, where ℓ is the number of momentum components with $p_\mu = \pi/a$. In the continuum limit $a \to 0$, the doublers become very heavy and decouple from the theory. This removes the unwanted poles from the propagator. With this extra term, we can write the Wilson's complete Dirac operator in a compact form

$$D^{(f)}(n|m)^{\alpha\beta}_{ab} = \left(m^{(f)} + \frac{4}{a}\right)\delta_{\alpha\beta}\delta_{ab}\delta_{n,m} - \frac{1}{2a}\sum_{\mu=\pm 0}^{\pm 3}(\mathbb{1} - \gamma_\mu)_{\alpha\beta}U_\mu(n)_{ab}\delta_{n+\hat{\mu},m}, \tag{2.44}$$

where we introduce $\gamma_{-\mu} \equiv -\gamma_\mu$. This concludes the Wilson's formulation of Lattice QCD. However, Wilson fermion is not the widely used regualrization in lattice QCD today. The main reason being that the extra term proposed by Wilson, breaks chiral symmetry even in the massless limit. For a long time, this seemed to be the ultimate limitation of QCD on the lattice. Eventually, it was found that exact chiral symmetry can be observed on the lattice if the Dirac operator satisfied the Ginsparg-Wilson relation [78]. This immediately followed formulations such as overlap fermions [79] and fixed point

Dirac operators [80]. For a more detailed discussion, the reader is referred to chapter 7 of Gattringer and Lang [76]. There have been several other formulations for fermions on the lattice, most of which have been based on solving the chiral symmetry problem. Some examples are staggered fermions [81], domain wall fermion [82]. In this thesis, we exclusively work with the twisted mass formalism [83].

2.2.3 Twisted Mass Fermions

Twisted mass Lattice QCD (tmLQCD) is a formulation of QCD with two mass-degenerate quark flavors of Wilson fermions. The Dirac operator is similar to Wilson fermions but with an additional mass term that has a non-trivial isospin structure. This additional mass is the twisted mass term. This is used as an infrared regulator and also this term produces automatic $O(a)$ improvement.

The lattice fermion action for tmLQCD is written as

$$S_F^{tm}[\chi, \bar{\chi}, U] = a^4 \sum_{n,m\in\Lambda} \bar{\chi}(n) \left(D(n|m)\mathbb{1}_2 + i\mu\gamma_5\tau^3\delta_{n,m} \right) \chi(m), \tag{2.45}$$

where $D(n|m)$ is the Wilson Dirac operator as defined in equation 2.44, albeit for a single flavor. The last term $i\mu\gamma_5\tau^3$ is the additional mass term, with μ being the twisted mass and τ^3 is the third Pauli matrix acting on the isospin space. The fermion fields χ and $\bar{\chi}$ are two-component spinors.

For a non-vanishing m (bare mass in Dirac operator) and the twisted mass μ, one defines the polar mass M and the twist angle α as

$$M = \sqrt{m^2 + \mu^2}, \qquad \alpha = \tan^{-1}\left(\frac{\mu}{m}\right). \tag{2.46}$$

Then, the two mass terms in the tmLQCD formulation can be combined as

$$m\mathbb{1}_2 + i\mu\gamma_5\tau^3 = Me^{i\alpha\gamma_5\tau^3} \quad \text{with} \quad m = M\cos(\alpha) \;\text{ and }\; \mu = M\sin(\alpha). \tag{2.47}$$

The case $\alpha = \pi/2$ implies $m = 0$, and is referred to as the maximal twist. Similarly, the case $\alpha = 0$ corresponds to zero twist.

The fermion fields, χ and $\bar{\chi}$, in the twisted basis can be transformed back to the physical basis by defining the rotation

$$\psi = R(\alpha)\chi, \quad \bar{\psi} = \bar{\chi}R(\alpha) \qquad \text{where } R(\alpha) = e^{i\alpha\gamma_5\tau^3/2}. \tag{2.48}$$

Then one can define the fermion action for tmLQCD in this physical basis as

$$S_F\left[\psi, \bar{\psi}, U\right] = a^4 \sum_{n,m\in\Lambda} \bar{\psi}(n) \left(D^{tm}(n|m) + M\mathbb{1}\delta_{n,m} \right) \psi(n), \tag{2.49}$$

where the twisted Dirac operator D^{tm} is now a 2-flavor operator and is given as

$$D^{tm}(n|m) = \frac{4}{a}e^{-i\alpha\gamma_5\tau^3}\delta_{n,m} - \frac{1}{2a}\sum_{\mu=\pm0}^{\pm3}\left(e^{-i\alpha\gamma_5\tau^3} - \gamma_\mu\right)U_\mu(n)\delta_{n+\hat{\mu},m}. \tag{2.50}$$

We observe that only the Wilson term is rotated, which anyway vanishes in the naive continuum limit

($a \to 0$).

This completes a very short introduction to the twisted mass formulation. For a much more detailed discussion, the reader is referred to [84].

$O(a)$ improvements

Automatic $O(a)$ improvement is a very useful property of tmLQCD. At maximal twist, the discretization effects of $O(a)$ vanish, and we are left with leading corrections of $O(a^2)$. For the free case, this can be quite easily shown. Consider the Dirac operator in the momentum space [76]

$$\frac{i}{a}\sum_{\mu}\gamma_{\mu}\sin(p_{\mu}a)+\frac{1}{a}\sum_{\mu}\Big(1-\cos(p_{\mu}a)\Big)+M\cos(\alpha)+iM\sin(\alpha)\gamma_5\tau^3. \tag{2.51}$$

The propagator (which is the inverse of this matrix) is found to be

$$\frac{-\frac{i}{a}\sum_{\mu}\gamma_{\mu}\sin(p_{\mu}a)+\frac{1}{a}\sum_{\mu}(1-\cos(p_{\mu}a))+M\cos(\alpha)-iM\sin(\alpha)\gamma_5\tau^3}{\frac{1}{a^2}\sum_{\mu}\sin^2(p_{\mu}a)+\Big(\frac{1}{a}\sum_{\mu}(1-\cos(p_{\mu}a))+M\cos(\alpha)\Big)^2+M^2\sin^2(\alpha)}. \tag{2.52}$$

One finds the two poles at

$$ip_0=\pm\sqrt{\boldsymbol{p}^2+M^2}\mp a\cos(\alpha)\frac{M^3}{2\sqrt{\boldsymbol{p}^2+M^2}}+O(a^2). \tag{2.53}$$

If we now set $\alpha=\pi/2$ (i.e., maximal twist), the $O(a)$ term vanishes, due to the factor $\cos(\alpha)$, and only corrections of $O(a^2)$ are left. In order to establish this improvement for the full tmLQCD, one can perform the Symanzik improvement program. To have maximal twist in the renormalized theory, one also needs to tune the bare mass parameter m to its critical value m_c, which is obtained by finding the point of vanishing PCAC quark mass.

The $O(a)$ improved effective action for tmLQCD is defined as

$$S_F^{eff}=S_0+S_1+...+O(a^2), \tag{2.54}$$

where

$$S_0=\sum_x\bar{\chi}(x)(D+i\mu\gamma_5\tau^3)\chi(x),\quad S_1=\sum_x\bar{\chi}(x)\,c_{SW}\,\sigma_{\mu\nu}\,F_{\mu\nu}\,\chi(x). \tag{2.55}$$

Here $c_{sw}\,\sigma_{\mu\nu}\,F_{\mu\nu}$ is the well known clover term, with c_{SW} being the Sheikoleslami-Wohlert improvement coefficient [85].

$N_f = 2+1+1$ lattice action

So far we have only talked about mass degenerate light quark doublet $(u\ d)^T$. However, one can add mass nondegenerate heavy quarks to the tmLQCD formulation. In a similar manner to the light quark doublet, one defines a bare heavy quark mass m_h and a corresponding twisted mass μ_σ. In the usual case, it is a mass nondegenerate heavy quark doublet $(s\ c)^T$ with the strange and the charm quark. For this, we also need to add an extra term of the form $\mu_\delta\tau^1$, where τ^1 is the first Pauli matrix, acting in the

flavor space. This term ensures that the required mass splitting between strange and charm is obtained, with the help of μ_δ. This defines the $N_f = 2+1+1$ formulation of tmLQCD. This is of importance to us, since the gauge ensembles we use for our calculation are $N_f = 2+1+1$ Wilson-clover twisted mass gauge ensemble. The lattice action for such a simulation is [86]

$$S = S_g + S^l_{tm} + S^h_{tm}, \tag{2.56}$$

where S_g is the Iwasaki improved gauge action given by

$$S_g = \frac{\beta}{3}\sum_x \left(b_0 \sum_{\mu<\nu}\{1 - \mathrm{ReTr}(U_{\mu\nu}(x))\} + b_1 \sum_{\mu\neq\nu}\{1 - \mathrm{ReTr}(U_{\mu\nu}(x))\}\right), \tag{2.57}$$

with $\beta = 6/g_0^2$, $b_1 = -0.331$ and $b_0 = 1 - 8b_1$. The fermion action with the light quark doublet is of the form

$$S^l_{tm} = \sum_x \bar{\chi}_l(x)\left[D_W(U) + \frac{i}{4}c_{SW}\sigma_{\mu\nu}F_{\mu\nu}(U) + m_l + i\mu_l\gamma_5\tau^3\right]\chi_l(x), \tag{2.58}$$

where $\chi_l = (u\ d)^T$. Here D_W is the massless Wilson Dirac operator. Similarly for the mass nondegenerate heavy quark doublets, we have

$$S^h_{tm} = \sum_x \bar{\chi}_h(x)\left[D_W(U) + \frac{i}{4}c_{SW}\sigma_{\mu\nu}F_{\mu\nu}(U) + m_h - \mu_\delta\tau^1 + i\mu_\sigma\gamma_5\tau^3\right]\chi_h(x), \tag{2.59}$$

where $\chi_h = (s\ c)^T$. One tunes the bare parameters, such that $m_h = m_l = m_c$. This ensures that all physical observables are automatically $O(a)$ improved.

2.2.4 Correlators on the Lattice

The way to calculate physical quantities in lattice QCD is through correlators. For an operator O, a correlator is usually defined as

$$C(n,m) = \langle O(n)\bar{O}(m)\rangle. \tag{2.60}$$

The location m is often called the source and n is called the sink. In practice we set the source at origin and the correlator depends on only one coordinate

$$C(n) = \langle O(n)\bar{O}(0)\rangle. \tag{2.61}$$

The operator O can be simple quarks like $u, d, s\ldots$, or interpolators for mesons or baryons. In this work, we will require both nucleon and pion correlators of different form. In this chapter, we look at the simple meson 2-point correlator. A typical meson interpolator is of the form

$$O_M = \bar{\psi}^{(f_1)}\,\Gamma\,\psi^{(f_2)} \tag{2.62}$$

where Γ can take different Dirac structure depending on the meson that we want to study (see Table 2.1 for examples). To calculate the meson correlators, we first need to define the quark propagator. The

State	Γ	Particles
Scalar	$\mathbb{1}, \gamma_0$	$f_0, a_0, K_0^*, ...$
Pseudoscalar	$\gamma_5, \gamma_0\gamma_5$	$\pi^\pm, \pi^0, \eta, K^\pm, K^0, ...$
Vector	$\gamma_\mu, \gamma_0\gamma_\mu$	$\rho^\pm, \rho^0, \omega, K^*, \phi, ...$
Axial Vector	$\gamma_\mu\gamma_5$	$a_1, f_1, ...$
Tensor	$\gamma_\mu\gamma_\nu$	$h_1, b_1, ...$

Table 2.1: Different forms of Γ for different mesons [76]

fermion action is ususally of the form (ignore the factors of a for now)

$$S_F[\psi, \bar{\psi}, U] = \bar{\psi} D \psi, \tag{2.63}$$

where D is the Dirac operator, which can have different forms based on the discretization. The generating functional for such an action is given as

$$W[\chi, \bar{\chi}] \equiv \int \mathcal{D}\psi \, \mathcal{D}\bar{\psi} \; \exp\left(-\bar{\psi} \, D \, \psi + \bar{\psi}\chi + \bar{\chi}\psi\right). \tag{2.64}$$

Performing a simple transformation of variables, $\psi' = \psi - D^{-1}\chi$ and $\bar{\psi}' = \bar{\psi} - \bar{\chi} D^{-1}$, we obtain

$$W[\chi, \bar{\chi}] = \int \mathcal{D}\psi' \, \mathcal{D}\bar{\psi}' \; \exp\left(-\bar{\psi}' \, D \, \psi'\right) \exp\left(\bar{\chi} \, D^{-1} \, \chi\right). \tag{2.65}$$

Now using the Matthews-Salam formula, which states

$$\int \mathcal{D}\psi \, \mathcal{D}\bar{\psi} \; \exp\left(\bar{\psi} \, D \, \psi\right) = \det[D], \tag{2.66}$$

one gets for the generating functional

$$W[\chi, \bar{\chi}] = \det[D'] \exp\left(\bar{\chi} \, D^{-1} \, \chi\right), \tag{2.67}$$

where $D' \equiv -D$. Then it is straightforward to show that

$$\begin{aligned} \langle \psi\bar{\psi} \rangle_F &= \frac{1}{Z_F} \frac{\partial}{\partial \chi} \frac{\partial}{\partial \bar{\chi}} W[\chi, \bar{\chi}] \Big|_{\chi, \bar{\chi}=0} \\ &= D^{-1}, \end{aligned} \tag{2.68}$$

where $\langle ... \rangle_F$ denotes the fermionic part of the expectation and $Z_F = \int \mathcal{D}\psi \, \mathcal{D}\bar{\psi} \; \exp(-S_F)$ is the fermionic part of the partition function. To obtain the total expectation, one "averages" over all available gauge configuratons.

Hence the inverse of the Dirac operator is known as the quark propagator. On the lattice, it can be denoted as a line connecting the source and the sink. Now going back to the meson correlators, if we

consider the simple iso-triplet operator of the form $O_T = \bar{d}\Gamma u$, we can show that

$$\begin{aligned}
\langle O_T(n)\bar{O}_T(0)\rangle_F &= \langle \bar{d}(n)\Gamma u(n)\bar{u}(0)\Gamma d(0)\rangle \\
&= \Gamma_{\alpha_1\beta_1}\,\Gamma_{\alpha_2\beta_2}\left\langle \bar{d}(n)\,{}^{\alpha_1}_{c_1}\,u(n)\,{}^{\beta_1}_{c_1}\,\bar{u}(0)\,{}^{\alpha_2}_{c_2}\,d(0)\,{}^{\beta_2}_{c_2}\right\rangle_F \\
&= -\Gamma_{\alpha_1\beta_1}\,\Gamma_{\alpha_2\beta_2}\left\langle u(n)\,{}^{\beta_1}_{c_1}\,\bar{u}(0)\,{}^{\alpha_2}_{c_2}\right\rangle_F \left\langle d(0)\,{}^{\beta_2}_{c_2}\,\bar{d}(n)\,{}^{\alpha_1}_{c_1}\right\rangle_F \\
&= -\Gamma_{\alpha_1\beta_1}\,\Gamma_{\alpha_2\beta_2}\,D_u^{-1}(n|0)_{\substack{\beta_1\alpha_2\\ c_1c_2}}\,D_d^{-1}(0|n)_{\substack{\beta_2\alpha_1\\ c_2c_1}} \\
&= -tr\left[\Gamma D_u^{-1}(n|0)\Gamma D_d^{-1}(0|n)\right],
\end{aligned} \tag{2.69}$$

where we have performed fermion contractions according to the Wick's theorem. Since we work in twisted mass, the up and down quarks are mass degenerate. And so for our purpose, we can set $D_u = D_d \equiv D$. One final step is the momentum projection. We want the hadrons to be in definite momentum eigenstates. Hence, the fourier transformation is performed as [76]

$$\tilde{O}(n_t, \boldsymbol{p}) = \frac{1}{\sqrt{|\Lambda_3|}} \sum_{\boldsymbol{n}\in\Lambda_3} O(n_t, \boldsymbol{n}) e^{-i\,a\,\boldsymbol{n}\,\boldsymbol{p}}, \tag{2.70}$$

where Λ_3 is the spatial part of the lattice with spatial components $\boldsymbol{n}$. One usually only momentum projects the interpolator at sink, and the one at source is left in real space. Therefore the final form of the Euclidean hadron correlators is

$$C(n_t, \boldsymbol{p}) = \langle \tilde{O}(n_t, \boldsymbol{p})\bar{O}(0)\rangle. \tag{2.71}$$

In a similar manner, one can calculate the nucleon correlators. Nucleons consist of 3 quarks and for the simplest case of proton and neutron, they form an isospin doublet. In terms of quark fields then, the proton takes the form $p = uud$ and the neutron $n = udd$. Considering only the case of $I_z = +1/2$ (the proton), the nucleon interpolator is of the form

$$O_N = \epsilon^{abc} u^a_\alpha \left(u^{b\,T}_\beta (C\gamma_5)_{\beta\gamma} d^c_\gamma\right), \tag{2.72}$$

which satisfies the correct quantum numbers of the proton. The term in the parantheses is called a diquark, which combines an up and a down quark using the charge conjugation matrix C and γ_5. The diquark has both isospin $I = 0$ and spin $J = 0$. Thus the full interpolator has $I = 1/2$,$I_z = +1/2$ and $J = 1/2$. The final quantum number is parity which in the case of proton is $P = +1$. Under parity, the nucleon interpolator transforms as

$$O^{\mathcal{P}}_N(n_0, \boldsymbol{n}) \rightarrow \gamma_0 O_N(n_0, -\boldsymbol{n}). \tag{2.73}$$

To take this into account, one can define the parity projected nucleon interpolator as

$$O_{N_\pm} = \epsilon^{abc} P_\pm u^a_\alpha \left(u^{b\,T}_\beta (C\gamma_5)_{\beta\gamma} d^c_\gamma\right), \tag{2.74}$$

where the parity projector is defined as

$$P_{\pm} = \frac{1}{2}(1 \pm \gamma_0). \tag{2.75}$$

Here O_{N_+} is the interpolator for the proton and O_{N_-} is the negative parity partner $N(1535)$. In a similar way, one can define the interpolators for other spin-1/2 baryons as [76]

$$\begin{aligned} O_{\Sigma_\pm} &= \epsilon_{abc} P_\pm \Gamma^A u_a \left(u_b^T \Gamma^B s_c\right), \\ O_{\Xi_\pm} &= \epsilon_{abc} P_\pm \Gamma^A s_a \left(s_b^T \Gamma^B u_c\right), \\ O_{\Lambda_\pm} &= \epsilon_{abc} P_\pm \Gamma^A \left(2 s_a \left(u_b^T \Gamma^B d_c\right) + d_a \left(u_b^T \Gamma^B s_c\right) - u_a \left(d_b^T \Gamma^B s_c\right)\right). \end{aligned} \tag{2.76}$$

Here three possible choices for the gamma matrices are $(\Gamma^A, \Gamma^B) = (\mathbb{1}, C\gamma_5)$, (γ_5, C) or $(\mathbb{1}, i\gamma_0 C\gamma_5)$, all of which give rise to $J^P = 1/2^+$ baryons. In this work, we will need nucleon 2-point and 3-point correlators, which are more involved, since they contain more quark fields, which results in more possible Wick contractions. We also work with non-local operators, as will be discussed in the next chapter. This makes the contractions non-trivial. The correlators necessary for this work will be discussed in detail in Chapter 5.

CHAPTER 3

Transverse Momentum Dependent Parton Distribution Functions

The first discussion of the partonic transverse momentum started as early as the 1970s [87–89], shortly after the birth of the parton model. The first analysis showing that transverse momentum is also generated by the radiation of gluons was done in 1979 [90]. A first formal study that put together the perturbative and nonperturbative components of TMDs was done by Collins and Soper in 1981 [91]. Several other studies in the 1980s formalized the TMD factorization to understand the DY processes [92–96]. This was later generalized to the SIDIS processes in [97, 98]. All these various approaches for TMD factorization were reconciled and the modern definition of TMDPDFs can be found in [99–101].

A complete formulation of the TMDPDFs through the TMD factorization of DY and SIDIS processes is beyond the scope of this thesis. In this chapter we will provide a brief overview of the relation between unpolarized TMDPDFs and the SIDIS cross section. We will start with the inclusive DIS and formulate the unpolarized PDF through a collinear factorization. We will then follow a similar procedure for the SIDIS process and formulate the TMDPDF. This formulation closely follows a lecture note by Bacchetta [102]. The reader is referred to this lecture note and also the book by Collins [103] for a significantly more detailed discussion on TMDs.

We will also briefly discuss the LaMET formalism. Then we will discuss the matching between the quasi-TMDPDF and the light-cone TMDPDF, followed by the description of the individual components necessary for the full calculation of the unpolarized TMDPDF.

3.1 Deep inelastic scattering (DIS)

We first consider the deep inelastic scattering (DIS) process, which is the most general method of probing hadron structures by scattering leptons off of nucleons. In inclusive DIS, only the lepton in the final state is observed. Hence the general form of such a process can be written as

$$\ell(l) + N(P) \to \ell(l') + \chi. \tag{3.1}$$

Here ℓ denotes the lepton and N the nucleon, with l and P being the corresponding momenta. ℓ' is the final state lepton that is observed and χ represents the final state hadrons that are not observed by

the detector. Depending on the lepton, the interaction can be mediated by either a photon or a W or Z boson. For simplicity, we only consider the case of an electron-proton scattering here, in which case the interacting boson is a photon. The photon carries a momentum $q = l - l'$.

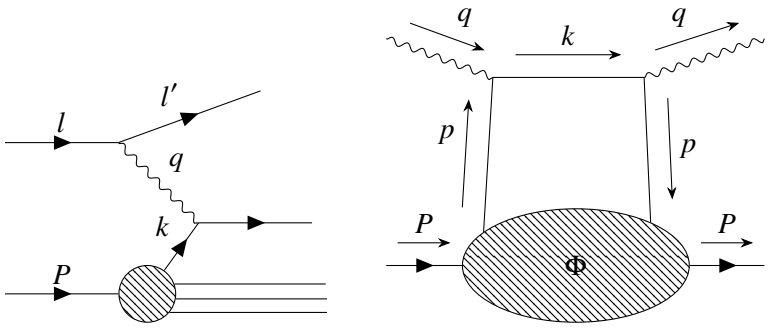

Figure 3.1: Feynman diagram (left) of a deep inelastic scattering process and the corresponding handbag diagram (right) for the hadronic tensor.

The cross-section of such a scattering process can in general be written as a contraction between a leptonic tensor, $L_{\mu\nu}$, and a hadronic tensor, $W^{\mu\nu}$, as

$$\frac{d^3\sigma}{dx_B dy d\phi_S} = \frac{\alpha^2}{2sx_B Q^2} L_{\mu\nu}(l, l', \lambda_e) 2M W^{\mu\nu}(q, P, S). \tag{3.2}$$

Here, $\alpha = \frac{e^2}{4\pi}$ is the electromagnetic fine structure constant, $l = (l + P)^2$ is the square of the center of mass energy. $Q^2 = -q^2$, $y = \frac{P\cdot q}{P\cdot l} = \frac{Q^2}{x_B s}$ and $x_B = \frac{Q^2}{2P\cdot q}$, which is known as the Bjorken scale. S is the spin vector of the target proton and λ_e is the helicity of the electron beam. ϕ_S is the azimuthal angle between the outgoing hadron and the spin of the target, which is defined according to the Trento conventions [104]. M is the proton mass, compared to which the electron mass can be neglected.

The leptonic tensor can be calculated perturbatively using QED. In the massless limit, it can be written as

$$\begin{aligned} L_{\mu\nu} &= \sum_{\lambda'_e} (\bar{u}(l', \lambda'_e)\gamma_\mu u(l, \lambda_e))^* (\bar{u}(l', \lambda'_e)\gamma_\nu u(l, \lambda_e)) \\ &= -Q^2 g_{\mu\nu} + 2(l_\mu l'_\nu + l'_\mu l_\nu) + 2i\lambda_e \epsilon_{\mu\nu\rho\sigma} l^\rho l'^\sigma. \end{aligned} \tag{3.3}$$

The information about the hadronic target is contained in the hadronic tensor $W^{\mu\nu}$. $W^{\mu\nu}$ can not be calculated perturbatively in a similar manner to $L_{\mu\nu}$, since it contains a nonperturbative hadronization process and we do not know the photon-proton vertex. If we consider the hadronization of the photon-proton interaction into all possible final hadron states χ with momentum P_χ, we can write the hadronic tensor as

$$2MW^{\mu\nu}(q, P, S) = \frac{1}{2\pi} \sum_\chi \int \frac{d^3 P_\chi}{(2\pi)^3 2P^0_\chi} (2\pi)^4 \delta^{(4)}(q + P - P_\chi) H^{\mu\nu}(P, S, P_\chi), \tag{3.4}$$

where

$$H^{\mu\nu}(P, S, P_\chi) = \langle P, S | J^\mu(0) | \chi \rangle \langle \chi | J^\nu(0) | P, S \rangle . \tag{3.5}$$

Here J^μ is the electromagnetic current. The integration over P_χ is possible, since in inclusive DIS the final state is undetected.

We can parametrize the hadronic tensor in terms of structure functions. Since this interaction only depends on the momentum transfer q and the proton momentum P, we can decompose the hadronic tensor in terms of all possible Lorentz invariant structures with q and P. For the electromagnetic current the most general form of the hadronic tensor can be written as

$$2MW^{\mu\nu} = 2M\left[Ag^{\mu\nu} + Bq^\mu q^\nu + C\frac{P^\mu P^\nu}{M^2} + D\frac{P^\mu q^\nu + q^\mu P^\nu}{M^2}\right], \tag{3.6}$$

Other possible combinations of P and q can be eliminated using symetries. For example, the term $i\epsilon_{\mu\nu\rho\sigma}P^\rho q^\sigma$ is excluded by parity invariance. One final constraint is the electromagnetic current conservation, which requires that

$$q_\mu W^{\mu\nu} = q_\nu W^{\mu\nu} = 0. \tag{3.7}$$

From this condition, we find

$$D = -\frac{P\cdot q}{q^2}B, \qquad C = -\frac{P\cdot q}{q^2}B + \frac{M^2}{q^2}A. \tag{3.8}$$

So finally, the hadronic tensor can be expressed in terms of two independent structure functions as follows

$$2MW^{\mu\nu}(q,P,S) = \frac{1}{x_B}\left[-g_\perp^{\mu\nu}F_T(x_B,Q^2) + \hat{t}^\mu\hat{t}^\nu F_L(x_B,Q^2)\right], \tag{3.9}$$

where

$$\hat{t}^\mu = \frac{2x_B}{Q\sqrt{1+\gamma^2}}\left(P^\mu - \frac{P\cdot q}{q^2}q^\mu\right), \qquad \gamma = \frac{2Mx_B}{Q}. \tag{3.10}$$

For a partonic approximation, we consider the limit $Q^2 \to \infty$. Under this condition, the hadronic tensor is light-cone dominated [105]. Hence it is useful to define the momenta in the light-cone coordinates as

$$P^\mu = P^+ n_+^\mu + \frac{M^2}{2P^+}n_-^\mu, \tag{3.11}$$

$$q^\mu = x_B P^+ n_+^\mu - \frac{Q^2}{2x_B P^+}n_-^\mu. \tag{3.12}$$

where $n_+^\mu = (1,0,0,1)/\sqrt{2}$ and $n_-^\mu = (1,0,0,-1)/\sqrt{2}$ are the light-cone vectors. In general, for any given vector $v^\mu = (v^0, v^1, v^2, v^3)$, the light-cone components are defined as

$$v^\mu = (v^+, v^-, v^\perp), \tag{3.13}$$

where

$$v^+ = \frac{1}{\sqrt{2}}(v^0 + v^3), \qquad v^- = \frac{1}{\sqrt{2}}(v^0 - v^3), \qquad v^\perp = (v^1, v^2). \tag{3.14}$$

At sufficiently high Q^2, one can assume that the scattering of the electron occurs with a point like quark of mass m inside the proton. The final state χ in Eq. (3.4), can be split into a quark with

momentum k and all possible hadron states X with momentum P_X. Considering the electron quark interaction at tree level, the hadronic tensor can be written as

$$\begin{aligned} 2MW^{\mu\nu} = \frac{1}{2\pi}\sum_q e_q^2 \sum_X \int \frac{d^3\boldsymbol{P_X}}{(2\pi)^3 2P_X^0} \int \frac{d^3\boldsymbol{k}}{(2\pi)^3 2k^0} \delta^{(4)}(P+q-k-P_X) \\ \times \langle P,S|\,\bar{\psi}_i(0)\,|X\rangle\,\langle X|\,\psi_j(0)\,|P,S\rangle\,\gamma^\mu_{ik}(\not{k}+m)_{kl}\gamma^\nu_{lj}. \end{aligned} \tag{3.15}$$

The subscript q denotes the quark flavor and e_q is the fractional charge of the quark. Using the on-shell condition

$$\int \frac{d^3\boldsymbol{k}}{2k^0} \to \int d^4k\,\delta\left(k^2-m^2\right)\theta\left(k^0-m\right), \tag{3.16}$$

and performing the Fourier transform of the Dirac delta function

$$\delta^{(4)}(P+q-k-P_X) = \int \frac{d^4\xi}{(2\pi)^4} e^{-i\xi\cdot(P+q-k-P_X)}, \tag{3.17}$$

the hadronic tesnor can be rewritten as

$$\begin{aligned} 2MW^{\mu\nu}(q,P,S) = \sum_q e_q^2 \sum_X \int \frac{d^3\boldsymbol{P_X}}{(2\pi)^3 2P_X^0} \int d^4k\,\delta\left((p+q)^2-m^2\right)\theta\left(p^0+q^0-m\right) \\ \times \int \frac{d^4\xi}{(2\pi)^4} e^{-i\xi\cdot(P-p-P_X)}\,\langle P,S|\,\bar{\psi}_i(0)\,|X\rangle\,\langle X|\,\psi_j(0)\,|P,S\rangle\,\gamma^\mu_{ik}(\not{p}+\not{q}+m)_{kl}\gamma^\nu_{lj}, \end{aligned} \tag{3.18}$$

where we have introduced the momentum $p = k - q$. Finally, performing the translation of the field operators and using the completeness relation, to eliminate X, we find

$$\begin{aligned} 2MW^{\mu\nu}(q,P,S) = \sum_q e_q^2 \int d^4p\,\delta\left((p+q)^2-m^2\right)\theta\left(p^0+q^0-m\right) \\ \times \mathrm{Tr}\left[\Phi(p,P,S)\gamma^\mu(\not{p}+\not{q}+m)\gamma^\nu\right] \end{aligned} \tag{3.19}$$

where we have introduced the quark-quark correlation function Φ as

$$\begin{aligned} \Phi_{ji}(p,P,S) &= \frac{1}{(2\pi)^4}\int d^4\xi e^{-i\xi\cdot p}\,\langle P,S|\,\bar{\psi}_i(\xi)\psi_j(0)\,|P,S\rangle \\ &= \sum_X \int \frac{d^3\boldsymbol{P_X}}{(2\pi)^3 2P_X^0}\,\langle P,S|\,\bar{\psi}_i(0)\,|X\rangle\,\langle X|\,\psi_j(0)\,|P,S\rangle\,\delta^{(4)}\big(P-p-P_X\big). \end{aligned} \tag{3.20}$$

This factorization can be understood from the handbag diagram for the hadronic tensor, as shown in Figure 3.1. The correlation function, in general depends on the quark flavor q and is denoted as Φ^q. If we parametrize the quark momentum p in the follwoing way

$$p^\mu = \left[xP^+, \frac{p^2+|\boldsymbol{p}_T|^2}{2xP^+}, \boldsymbol{p}_T\right], \tag{3.21}$$

assuming that the quark momentum is soft compared to the hadron momentum, we see that the only relevant component is xP^+. Neglecting terms that are $1/Q$ supressed, we obtain the hadronic tensor as

$$\begin{aligned} 2MW^{\mu\nu}(q,P,S) &\approx \sum_q e_q^2 \int d^2\boldsymbol{p}_T dp^- dx \frac{P^+}{2P\cdot q}\delta(x-x_B) \\ &\quad \times \mathrm{Tr}\left[\Phi^q(p,P,S)\gamma^\mu(\not{p}+\not{q}+m)\gamma^\nu\right] \\ &\approx \sum_q e_q^2 \frac{1}{2}\mathrm{Tr}\left[\Phi^q(x_B,S)\gamma^\mu\gamma^+\gamma^\nu\right]. \end{aligned} \tag{3.22}$$

Here $\Phi^q(x,S)$ now denotes the integrated correlation function

$$\begin{aligned} \Phi^q_{ji}(x,S) &= \int d^2\boldsymbol{p}_T dp^- \Phi^q(p,P,S)\Big|_{p^+=xP^+} \\ &= \int \frac{d\xi^-}{2\pi} e^{-i\xi\cdot p} \langle P,S|\,\bar\psi^q_i(\xi)\psi^q_j(0)\,|P,S\rangle\Big|_{\xi^+=\xi_T=0}. \end{aligned} \tag{3.23}$$

Again, considering the simple unpolarized case, Φ^q can be decomposed into

$$\Phi^q(p,P) = MA_1\mathbf{1} + A_2\not{P} + A_3\not{p} + \frac{A_4}{M}\sigma_{\mu\nu}P^\mu p^\nu, \tag{3.24}$$

where $A_i = A_i(p\cdot P, p^2)$ are real scalar functions. Again, using the parametrization of p given in Eq. (3.21) and keeping only leading terms in $1/P^+$, we obtain

$$\begin{aligned} \Phi^q(p,P) &\approx P^+(A_2+xA_3)\not{n}_+ + P^+\frac{i}{2M}\left[\not{n}_+,\not{p}_T\right]A_4, \\ &= f_1^q(x)\not{n}_+/2, \end{aligned} \tag{3.25}$$

where we have introduced the integrated parton distribution function $f_1^q(x)$. This is the so-called unpolarized parton distribution function (PDF) and is often denoted simply as $q(x)$. The collinear PDF can be obtained from the integrated correlated function through the projection

$$f_1^q(x) = \frac{1}{2}\mathrm{Tr}\left[\Phi^q(x)\gamma^+\right]. \tag{3.26}$$

Using the definition from Eq. (3.20), we obtain the hadronic matrix element of the PDF as

$$f_1^q(x) = \int \frac{d\xi^-}{4\pi} e^{-i\xi\cdot p}\,\mathrm{Tr}\left[\langle P,S|\,\bar\psi^q(\xi)\gamma^+\psi^q(0)\,|P,S\rangle\right]\Big|_{\xi^+=\xi_T=0}. \tag{3.27}$$

This definition, however, is not gauge invariant, since the non-local operator $\bar\psi^q(\xi)\gamma^+\psi^q(0)$ is not invariant under the gauge transformation

$$\psi(\xi)\to e^{i\alpha(\xi)}\psi(\xi), \qquad \bar\psi(\xi)\to\bar\psi(\xi)e^{-i\alpha(\xi)}. \tag{3.28}$$

The solution to this problem is to include a gauge link or Wilson line connecting the two quarks as

follows

$$f_1^q(x) = \int \frac{d\xi^-}{4\pi} e^{-i\xi\cdot p} \,\mathrm{Tr}\left[\langle P,S|\,\bar{\psi}^q(\xi)\gamma^+ W_{n_-}(0,\xi)\psi^q(0)\,|P,S\rangle\right]\Big|_{\xi^+=0}. \tag{3.29}$$

where the gauge link is defined as

$$W_{n_-}(\xi,+\infty) = \mathcal{P}\exp\left[-ig\int_{\infty^-}^{\xi^-} d\eta^- A^+(\eta^-,0,\mathbf{0}_T)\right]. \tag{3.30}$$

3.2 Semi-inclusive deep inealstic scattering (SIDIS)

A semi-inclusive DIS process also involves the detection of a hadron in the final state. The general form of such a process can be written as

$$\ell(l) + N(P) \to \ell(l') + h(P_h) + \chi, \tag{3.31}$$

where all the definitions remain identical as before, with the addition of h being the detected hadron carrying momentum P_h. In the case that the hadron polarization is not detected, we can define $P_{h\perp}$ as the transverse part of P_h with respect to the virtual photon momentum q. The cross section for this one-particle inclusive electron-nucleon scattering process can be written as

$$\frac{2E_h d^6\sigma}{d^3P_h dx_B dy d\phi_s} = \frac{\alpha^2}{2sx_B Q^2} L_{\mu\nu}(l,l',\lambda_e) 2MW^{\mu\nu}(q,P,S,P_h). \tag{3.32}$$

Following an identical procedure as in the inclusive case, the hadronic tensor can be decomposed as

$$2MW^{\mu\nu}(q,P,S,P_h) = \sum_q e_q^2 \int d^4p d^4k \delta^{(4)}(p+q-k)\,\mathrm{Tr}\left(\Phi(p,P,S)\gamma^\mu\Delta(k,P_h)\gamma^\nu\right), \tag{3.33}$$

where Φ is the quark-quark correlation function defined in Eq. (3.20) and Δ is the quark-fragmentation function, which describes the hadronization of a quark with momentum k into a hadron with momentum P_h. This factorization follows from the handbag diagram shown in Figure 3.2.

We focus on the correlation function Φ. Unlike the inclusive case, we can not obtain an integrated correlation function for the SIDIS process. We can only define an "unintegrated" or "transverse momentum dependent" correlation function, which in leading twist (upto $O(1/Q)$) can be expressed by the 8 leading quark TMDPDFs (as shown in Figure 1.4) [106–109]

$$\begin{aligned}\Phi(x,p_T,S) &= \int dp^-\Phi_{ij}(p,P,S)\\ &= \frac{1}{2}\left[f_1\not{n}_- + f_{1T}^\perp\frac{\epsilon_{\mu\nu\rho\sigma}\gamma^\mu n_+^\nu p_{\perp\rho}S_T^\sigma}{M} + \left(S_L g_1 + \frac{p_T,S_T}{M}g_{1T}^\perp\right)\gamma^5\not{n}_+\right.\\ &\quad \left. + h_{1T}i\sigma_{\mu\nu}\gamma^5 n_+^\mu S_T^\nu + \left(S_L h_{1L}^\perp + \frac{p_T S_T}{M}h_{1T}^\perp\right)\frac{i\sigma_{\mu\nu}\gamma^5 n_+^\mu P_\perp^\nu}{M} + h_1^\perp\frac{\sigma_{\mu\nu}p_T^\mu n_+^\nu}{M}\right].\end{aligned} \tag{3.34}$$

In this work, we are interested in calculating $f_1(x,p_T)$, which is the unpolarized TMDPDF.

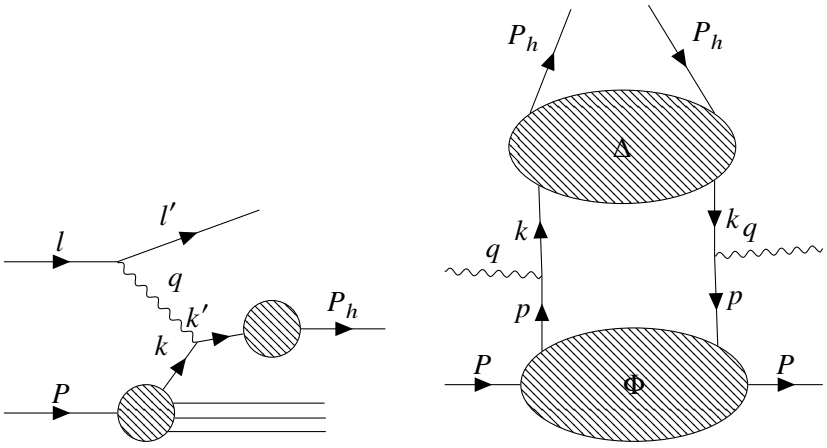

Figure 3.2: Feynman diagram (left) of a semi-inclusive deep inelastic scattering process and the corresponding handbag diagram (right) for the hadronic tensor.

$f_1(x, p_T)$ has a similar hadronic matrix element definition as the collinear PDF. The difference is in the gauge invariant definition, in particular the shape of the gauge link connecting the non-local quark fields. The gauge invariant definition now takes the form [103]

$$f_1(x, p_T) = \int \frac{d\xi^- d^2\xi_T}{(2\pi)^3} e^{-ip\cdot\xi} \operatorname{Tr}\left[\langle P|\,\bar{\psi}(\xi) W'_{n_-}(\xi, +\infty)\gamma^+ W'_{n_-}(+\infty, 0)\psi(0)\,|P\rangle\right]. \tag{3.35}$$

The gauge links here are defined as

$$W'_{n_-}(\xi, +\infty) = W_{n_-}(\xi^-, \infty^-; \boldsymbol{\xi}_T)\, W_T(\boldsymbol{\xi}_T, \boldsymbol{\infty}_T; \infty^-), \tag{3.36}$$

where W_{n_-} is the Wilson line along the minus direction and W_T is the Wilson line along the transverse direction,

$$W_{n_-}(\xi^-, \infty^-; \boldsymbol{\xi}_T) = \mathcal{P} \exp\left[-ig \int_{\infty^-}^{\xi^-} d\eta^- A^+(\eta^-, \boldsymbol{\xi}_T)\right], \tag{3.37}$$

$$W_T(\boldsymbol{\xi}_T, \boldsymbol{\infty}_T; \infty^-) = \mathcal{P} \exp\left[-ig \int_{\boldsymbol{\infty}_T}^{\boldsymbol{\xi}_T} d\boldsymbol{\eta}_T A^+(\infty^-, \boldsymbol{\eta}_T)\right]. \tag{3.38}$$

This gives rise to a staple shaped Wilson line as shown in Figure 3.3.

3.3 Large momentum effective theory (LaMET)

One main feature of the definitions of PDFs and TMDPDFs is that they are defined as light-cone correlation functions. This makes a first principle calculation with lattice QCD nearly impossible. Since Wilson's formulation of lattice QCD is Euclidean, one needs to get rid of the real-time dependence. Over the years, there have been many different approaches to tackle this problem [39–45]. One of the most successful methods, in recent years, have been the development of the large momentum effective theory (LaMET) [46, 47].

The basic idea behind LaMET is to define a relation between an Euclidean observable $\tilde{f}$ defined

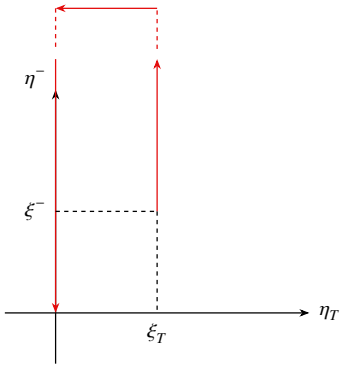

Figure 3.3: Staple shaped Wilson line in the defintion of the gauge invariant TMDPDF.

at a large momenta P^z and its physical counterpart $f(\mu^2)$ which exists on the light cone. Usign the asymptotic freedom and assuming that $P^z >> \Lambda_{QCD}$, one can systematically expand the P^z dependence of $\tilde{f}$ as [46]

$$\tilde{f}\left(x,\mu^2,P^z\right) = \int_x^1 \frac{dy}{y} Z\left(\frac{x}{y},\frac{\mu}{P^z}\right) f\left(y,\mu^2\right) + O\left(\Lambda^2/\left(P^z\right)^2, M^2/\left(P^z\right)^2\right). \tag{3.39}$$

This expansion is similar to the case of heavy quark effective theory (HQET) [110], where one does a similar expansion in terms of a heavy quark mass. With this Ji argues that the parton model as formulated by Feynman could be an effective theory of the hadron moving at large momentum. And the most important point is that the expansion will converge at large enough P^z which then enables us to access observables at infinite P^z by calculating them at large but finite P^z. The matching factor Z is calculable in perturbation theory. $\tilde{f}$ is usually called the quasi-observable. In case of f being the TMDPDF, $\tilde{f}$ would be the quasi-TMDPDF. And this quasi-observable defined at finite P^z can be calculated on the lattice.

The momentum dependence of the quasi-observable can be studied through renormalization group as

$$\frac{\partial \tilde{f}(P^z)}{\partial \ln P^z} = \gamma(\alpha_s)\tilde{f}(P^z) + O\left(\frac{1}{P^z}\right), \tag{3.40}$$

where the anomalous dimension is defined as

$$\gamma(\alpha_s) = \frac{1}{Z}\frac{\partial Z}{\partial \ln P^z}. \tag{3.41}$$

This is the standard setup for effective theory expansion similar to HQET.

The formulation of LaMET then provides us with a recipe for studying parton physics in lattice QCD as follows [47]:

1. Start with a ligh-cone parton observable f.
2. Construct an Euclidean observable $\tilde{f}$, which converges to f under an infinite Lorenzt boost.
3. Calculate the lattice matrix element $\tilde{f}$ for a hadron with large momentum P^z.
4. Use Eq. (3.39) to extract the parton observable f.

The exact expansion of LaMET depends on the observable of interest and has been studied for different kinds of partonic observables. For a more detailed discussion, the reader is referred to the review by Ji *et. al.* [62].

3.4 TMDPDFs on the lattice

Under LaMET, the matching of the TMDPDFs takes the following form [62, 111]

$$f^{TMD}(x,b,\mu,\zeta) = H_f(\frac{\zeta_z}{\mu^2})\, e^{-\ln\left(\frac{\zeta_z}{\zeta}\right)K(b,\mu)}\, S_r^{\frac{1}{2}}(b,\mu)\, \tilde{f}(x,b,\mu,\zeta_z) + O\left(\frac{\Lambda_{QCD}}{\zeta_z}, \frac{M^2}{(P^z)^2}, \frac{1}{b^2\zeta_z}\right). \tag{3.42}$$

Here $f^{TMD}(x,b,\mu,\zeta)$ is the rapidity-independent physical TMDPDF, defined on the position space, with b being the transverse distance. S_r is the reduced soft function, K is the Collins-Soper kernel and H_f is the hard kernel for TMDPDFs. ζ and ζ_z are the Collins-Soper scales for the physical TMDPDF and the quasi-TMDPDF respectively.

The rapidity regularization is necessary for controlling the divergences from light-like Wilson lines in the definition of TMDPDFs. This effectively introduces a rapidity cutoff which depends on the rapifity scale $\zeta = 2(xP^+)^2 e^{2y_\eta}$, where y_η is the rapidity regulator. Several proposals have been made for this rapidity regulator. The most established physics motivated definition [99, 100, 112] is the physical TMDPDF defined here, which turns out to be rapidity regularization independent. Another important part of the LaMET matching is the presence of the soft contribution [53–56] arising from the soft gluon exchange between the Wilson lines. This has to be subtracted in the final factorization formula. This is acheived by the soft function S, which under the same rapidity regularization scheme as the quasi-TMDPDF, makes the physical TMDPDF scheme independent. On the lattice one calculates a rapidity independent reduced soft function S_r [58], which is related to S as [103]

$$S(b,\mu,\zeta,\zeta') = e^{(\zeta+\zeta')K(b,\mu)} S_r^{-1}(b,\mu). \tag{3.43}$$

The final piece of the puzzle is the Collins-Soper kernel $K(b,\mu)$, which governs the rapidity scale evolution of TMDPDFs [91]. On the lattice, we need to calculate the quasi-TMDPDF $\tilde{f}$, the Collins-Soper kernel K and the reduced soft function S_r. The quasi-TMDPDF is defined at a rapidity scale $\zeta_z = (2zP^z)^2$, where P^z is the large but finite boost applied to the quasi-observable. With these 3 quanitites calculated perturbatively, they can be matched to the physical TMDPDF, using the hard matching kernel H_f, which is calculated perturbatively as [59]

$$H_f\left(\frac{\zeta_z}{\mu^2}\right) = 1 - \frac{\alpha_s}{4\pi}C_F\left[-4 + \frac{\pi^2}{6} + 2\ln\left(\frac{\zeta_z}{\mu^2}\right) - \ln^2\left(\frac{\zeta_z}{\mu^2}\right)\right] + O\left(\alpha_s^2\right). \tag{3.44}$$

The TMDPDF defined on Eq. (3.35) can be obtained from f^{TMD} through a Fourier transform,

$$f_1(x,p_T,\mu,\zeta) = \int \frac{d^2\boldsymbol{b}}{(2\pi)^2} e^{i\boldsymbol{b}\cdot\boldsymbol{p}_T} f^{TMD}(x,b,\mu,\zeta). \tag{3.45}$$

In literature, the transverse separation b is often denoted as b_T or $b_\perp$, however we drop the subscript for simplicity and also to avoid confusion with the impact parameter $b_\perp$ of GPDs.

3.4.1 Quasi-TMDPDF

The quasi-TMDPDF is the main component of the TMD factorization on lattice. It is the quasi-observable $\tilde{f}$ defined in Eq. (3.39). So it has a very similar hadronic matrix element definition as the TMDPDF in Eq. (3.35). It is defined as

$$\tilde{f}\left(x, b, \mu, \zeta_z\right) = \int_{-\infty}^{+\infty} \frac{P^z dz}{2\pi} e^{ixzP^z} B\left(z, b, \mu, P^z\right), \tag{3.46}$$

where $B(z, b, \mu, P^z)$ is the so-called quasi-beam function. It contains the fully spatial hadronic matrix element

$$B\left(z, b, \mu, P^z\right) = Z_\Gamma(\mu, P^z) \lim_{l\to\infty} \frac{\left\langle H\left(P^z\right) \left| O_\Gamma(0, \overrightarrow{0}, b, l, z) \right| H\left(P^z\right)\right\rangle}{\sqrt{Z_E(2|l|, |b|)}}. \tag{3.47}$$

Here, $H(P^z)$ is the hadron state with large momentum P^z and $O_\Gamma(0, \overrightarrow{0}, b, l, z)$ is the non-local staple-shaped Wilson line quark bilinear operator (will be referred to as the staple-shaped operator).

$$O_\Gamma(t, \boldsymbol{x}, b, l, z) = \bar{q}\left(t, \boldsymbol{x} + b\hat{n}_T + \frac{z}{2}\hat{n}_z\right) \Gamma \mathcal{W}_{\text{staple}}\left(\boldsymbol{x}, b, l, z\right) q\left(t, \boldsymbol{x} - \frac{z}{2}\hat{n}_z\right). \tag{3.48}$$

Here $\mathcal{W}_{\text{staple}}\left(\boldsymbol{x}, b, l, z\right)$ is the staple-shaped Wilson line connecting the two quark fields.

$$\mathcal{W}_{\text{staple}}\left(\boldsymbol{x}, b, l, z\right) = W_z\left(\boldsymbol{x} + b\hat{n}_T + \frac{z}{2}\hat{n}_z, l - \frac{z}{2}\right) W_T^\dagger\left(\boldsymbol{x} + l\hat{n}_z, b\right) W_z^\dagger\left(\boldsymbol{x} - \frac{z}{2}\hat{n}_z, l + \frac{z}{2}\right). \tag{3.49}$$

The staple-shaped Wilson line is illustrated in Figure 3.4. The major difference from the physical TMDPDF defined in Eq. (3.35) being that the staple in the beam function has a finite length l in the direction of the momentum. This is why the limit of $l \to \infty$ is taken in Eq. (3.47), however, as we will show in Section 6, the beam function is independent of l for large enough l.

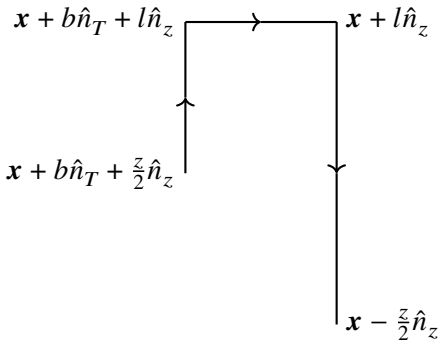

Figure 3.4: Staple-shaped Wilson line defined on the lattice.

The factor $Z_E(2|l|, |b|)$ in the denominator of Eq. (3.47) is a rectangular Wilson loop defined in the plane containing the boost P^z and the transverse separation b.

$$Z_E\left(r_1, r_2\right) = \frac{1}{N_c}\left\langle W_z\left(0, r_1\right) W_T\left(r_1\hat{n}_z, r_2\right) W_z^\dagger\left(r_2\hat{n}_T, r_1\right) W_T^\dagger\left(0, r_2\right)\right\rangle. \tag{3.50}$$

This factor is necessary for canceling the divergences associated to the Wilson lines of the staple-shaped operator. The factor $Z_\Gamma(\mu, P^z)$ is a renormalization factor. Both of these will be discussed in more detail in the following chapter.

3.4.2 Soft function

The soft function is necessary to cancel the soft gluon divergences in the TMDPDFs [58]. Using LaMET, the reduced soft function can be calculated as a ratio of meson form factor and TMD wave function (TMDWF) [58, 62].

$$S_r(b,\mu) = \frac{F_\Gamma\left(b, P, P', \mu\right)}{\mathcal{H}_{F_\Gamma}\left(b, P, P', \mu\right)}. \tag{3.51}$$

The four-point meson form factor contains 2 local currents separated by a transverse separation b inserted between pion external states boosted to momenta P and P'.

$$F_\Gamma\left(b, P, P', \mu\right) = \left\langle \pi\left(P'\right) \left| \bar{q}_2(b)\Gamma q_2(b)\bar{q}_1(0)\Gamma q_1(0) \right| \pi(P) \right\rangle. \tag{3.52}$$

The denominator in Eq. (3.51) contains the quasi-TMDWF $\tilde{\Psi}$.

$$\mathcal{H}_{F_\Gamma}\left(b, P, P', \mu\right) = \int_{-\infty}^{\infty} dx \int_{-\infty}^{\infty} dx' H_{F_\Gamma}\left(x, x', P, P', \mu\right) \tilde{\Psi}^\dagger_{\bar{q}q}\left(x', b, \mu, P'\right) \tilde{\Psi}_{\bar{q}q}(x, b, \mu, P). \tag{3.53}$$

where the quasi-TMDWF in the momentum space is obtained from the spatial quasi-observable $\tilde{\psi}$,

$$\tilde{\Psi}_{\bar{q}q}\left(x, b, \mu, \zeta_z, \bar{\zeta}_z\right) = \int_{-\infty}^{+\infty} \frac{P^z dz}{2\pi} e^{i(x-1/2)zP^z} \tilde{\psi}_{\bar{q}q}\left(z, b, \mu, P^z\right). \tag{3.54}$$

$\tilde{\psi}$ contains a hadronic matrix element similar to the quasi-beam function, except the staple-shaped operator is now inserted between the vacuum and a pion external state with a boost of P^z.

$$\tilde{\psi}_{\bar{q}q}\left(z, b, \mu, P^z\right) = Z_\Gamma(\mu, P^z) \lim_{l\to\infty} \frac{\langle\Omega| O_\Gamma(0, \overrightarrow{0}, b, l, z) |\pi(P^z)\rangle}{\sqrt{Z_E(2|l|, |b|)}}. \tag{3.55}$$

The definitions of the operator and the Wilson loop are identical to the quasi-beam function. Z_Γ is the renormalization factor and will be discussed in the next chapter. And finally, H_{F_Γ} is the hard kernel for the TMDWF, which is calculated in perturbation theory to be [113]

$$\begin{aligned} H_{F_\Gamma}\left(x, x', P, P', \mu\right) =& 1 + \frac{\alpha_s}{4\pi} C_F \left[h_0^\Gamma + 2\pi^2 + \ln^2\left(-\frac{|x'|}{|x|} \mp i\varepsilon\right) + \right. \\ & \left. \ln^2\left(-\frac{|1-x'|}{|1-x|} \mp i\varepsilon\right) + h_1^\Gamma \ln\left(\frac{16|x||1-x|\,|x'|\,|1-x'|\,\left(P^z\right)^4}{\mu^4}\right)\right] + O\left(\alpha_s^2\right). \end{aligned} \tag{3.56}$$

3.4.3 Collins-Soper kernel

The Collins-Soper kernel is the rapidity scale evolution kernel for TMDPDFs. Inverting Eq. (3.42) for the Collins-Soper kernel we get

$$K(b,\mu) = \zeta_z \frac{d}{d\zeta_z} \ln \tilde{f}(x,b,\mu,\zeta_z) + \mathcal{G}(x^2\zeta_z,\mu) + O\left(\frac{1}{\zeta_z}\right) \tag{3.57}$$

where $\mathcal{G}$ is a rapidity dependent perturbative function. Therefore we can extract the Collins-Soper kernel by considering the quasi-TMDPDF at two different rapidity scales. Since the TMDWF has a similar matching formula to that of the TMDPDF, one can use a similar approach with the quasi-TMDWF as well. The Collins-Soper kernel can then be defined as [69]

$$K(b,\mu) = \frac{1}{\frac{1}{2}\ln\left(\frac{\zeta_{z_1}}{\zeta_{z_2}}\right)} \ln\left(\frac{\tilde{\Psi}_{\bar{q}q}\left(x,b,\mu,\zeta_{z_1},\bar{\zeta}_{z1}\right)}{\tilde{\Psi}_{\bar{q}q}\left(x,b,\mu,\zeta_{z_2},\bar{\zeta}_{z2}\right)}\right) - \frac{\alpha_s}{4\pi}C_F\left[4 - \ln\left(\frac{\zeta_{z_1}\zeta_{z_2}\bar{\zeta}_{z_1}\bar{\zeta}_{z_2}}{\mu^8}\right) \mp 4i\pi\right] + O(\alpha_s^2) \tag{3.58}$$

where ζ_{z_1} and ζ_{z_2} are the two different rapidity scales corresponding to two different momentum boosts P_1^z and P_2^z respectively. The other rapidity scale $\bar{\zeta}_z = (2(1-x)P^z)^2$ where $(1-x)$ is the momentum fraction of the incoming antiquark.

CHAPTER 4

Renormalization

This chapter closely resembles our publication [74] on the non-perturbative renormalization of the staple-shaped operator.

The lattice quasi-observables defined in the previous chapter need to be renormalized non-perturbatively and matched to $\overline{\text{MS}}$ through perturbative matching. The renormalization of the meson four point form factor is trivial, since it contains only local currents separated by a transverse distance. Hence it can be renormalized multiplicatively with the factors $Z^{\overline{\text{MS}}}_{S/P/V/A}$ depending on the Γ-structure of the currents under consideration. These factors are scheme- and scale-independent and are calculated on the lattice for a given action and lattice spacing. The case for $b = 0$ is however non-trivial since it contains a contact term and one needs to consider the mixing of a local four-quark operators. But for the purpose of this study, $b = 0$ case is ill-defined and we will not consider it further.

The renormalization of the quasi-TMDPDF and quasi-TMDWF is more involved. Both the matrix elements under consideration contain the same staple-shaped Wilson line quark bilinear operator. The renormalization of this operator is more complex compared to the straight Wilson line in the case of the quasi-PDF. In particular, the staple-shaped Wilson line has three types of divergences, namely

1. linear divergence coming from the Wilson line, which connects the quark fields and which depends on the length of the staple- shaped link,
2. logarithmic divergence coming from the endpoints of the staple link which is similar to the case of the straight gauge links,
3. logarithmic divergences coming from the presence of cusps in the staple.

Moreover, in the case of infinite staple length l, which is the case of interest, pinch-pole singularities arise as positive powers of l, which comes from the gluon exchange between the transverse segments of the staple. Also, operators of different Dirac structures can and will mix on the lattice among certain groups when chiral symmetry is broken. This needs to be studied using discrete symmetries. And as we will show, the mixing pattern of operators can be significantly more involved than in the case of the straight Wilson line.

A first study within lattice perturbation theory to one-loop for the case of the symmetric staple [114] ($z = 0$ in the defintion of the staple) showed mixing between specific pairs of Dirac structures. This mixing cannot be avoided when one is interested in matching bare lattice Green's functions to the

$\overline{\text{MS}}$ scheme (directly or indirectly through an intermediate scheme). The mixing depended solely on the direction of the staple link entering the endpoints of the staple, regardless of the shape of the staple. This implies that the same mixing pattern occurs also for asymmetric staple shapes (which is the case under consideration). In Ref. [115], the mixing pattern of these staple-shaped operators has been studied using symmetry considerations. It was found that more mixing is present than observed in Ref. [114]. This demonstrates that one-loop perturbation theory cannot fully reveal the mixing of the staple-shaped operators, unlike the case of straight Wilson-line operators [116], and a higher-loop computation is needed to confirm the additional mixing patterns found by symmetry arguments. The authors of Refs. [63, 66, 73] consider a maximal RI-type prescription, in which all 16 independent non-local Wilson-line quark bilinear operators are chosen to mix to eliminate all possible mixing effects. While Ref. [66] identified nonzero contributions in several off-diagonal elements of the renormalization matrix, Refs. [63, 73] found negligible contributions, at least at small transverse separations, by setting specific momentum components to be zero. However, we emphasize that not all contributions are necessary for addressing the "unavoidable" mixing among the asymmetric staple-shaped operators on the lattice. Most off-diagonal elements in the 16×16 renormalization matrix are nonzero due to the non-minimal choice of renormalization conditions and not due to the unavoidable mixing. In this sense, it is preferable to construct a minimal intermediate scheme, keeping only the mixing sets that are needed for matching the bare lattice Green's functions to the corresponding $\overline{\text{MS}}$-renormalized Green's functions (as obtained in dimensional regularization). In our study, we consider such a minimal scheme by using symmetry arguments to restrict the operators allowed to mix.

Improving renormalization schemes on the lattice eliminates finite lattice spacing errors, which can come from different Dirac structures in Green's functions under consideration. A way of removing artifacts from all Dirac structures is to consider a wider mixing pattern, where higher dimensional operators multiplied by the appropriate power of the lattice spacing can also mix with the operators under study. This mixing is only present for finite values of the lattice spacing, while it vanishes when taking the continuum limit. The higher-dimensional operators will be higher twist since (by Lorentz invariance) they must have the same spin (with the operators under study), but their dimension will be higher. The unwanted effects of finite lattice spacing errors and higher-twist contributions are however not considered in the current work.

On the other hand, it has been shown [117] that the linear divergence in the lattice spacing a is not fully eliminated when the RI/MOM scheme is used to renormalize a straight Wilson line of length z. Ref. [73] has shown that this residual linear divergence remains in the case of the staple-shaped operator. In this scenario, an alternative approach that one can adopt is the so-called *ratio scheme* as proposed for the quasi-PDF case [48, 49, 118]. In this approach, one subtracts the Ultra-Violet (UV) divergences by taking the ratio with a suitable object at a fixed short distance, where perturbation theory applies. Different choices of suitable objects to be used in the ratio have been proposed in Ref. [119]. The authors of Refs. [73, 120] use ratios of the matrix elements of the operator under study. As the divergences of the staple-shaped operator are independent of the longitudinal momentum of the state, one can use the matrix elements computed at different values of the momentum in order to cancel the divergences. Usually, matrix elements at zero momentum are chosen for the denominator, and such scheme has been named [120] *short distance ratio* (SDR) scheme.

As for the remaining divergences associated with the asymmetric staple-shaped link, one can cancel them by taking an appropriate ratio with the vacuum expectation value of a rectangular Wilson loop [59]. However, we would like to stress that the SDR scheme is valid when operator mixing is

absent or negligible. We check that in the case under study the mixing is indeed negligible and thus, one can employ the ratio scheme. Another option, as proposed in Ref. [115], is to employ RI/MOM in the spirit of the SDR scheme by fixing the dimensions of the staple at a short perturbative range (we will call this scheme *RI-short*).

In this work, we firstly study the mixing of the staple-shaped operator with other operators of same dimension and find the minimal set of operators that are allowed to mix using symmetry arguments. We then proceed with the standard RI/MOM renormalization considering this set of operators and see the effect of mixing. Finding that the mixing is negligible (as will be shown in Chapter 6), we proceed with the SDR and RI-short scheme and compare their results. In the following sections we discuss the operator mixing and then the 3 different renormalization procedures.

4.1 Operator mixing through symmetry

In order to use symmetry arguments to determine which operators mix, we first organize the staple-shaped operator using all possible ways to connect the fermion fields. We show in Fig. 4.1 all the distinct possibilities of connecting a quark and an antiquark field located at a spatial separation of $(0, b, z)$, using an asymmetric staple-shaped Wilson line. Since we build the staples only in the yz-plane, in the following discussion and in Fig. 4.1, we denote the coordinate space (t, x, y, z) as only (y, z). Without loss of generality, we can fix the quark field (q) at $(0, 0)$. Then, the only possibilities for the position of the antiquark field ($\bar{q}$) are (b, z), $(b, -z)$, $(-b, z)$ and $(-b, -z)$. Here, b and z are strictly non-negative. We define the staple-shaped Wilson line connecting q at $(0, 0)$ and $\bar{q}$ at (b, z) as $O^{++}(\Gamma)$. The two plus signs denote the direction of separation of $\bar{q}$ from q. The first sign is for the transverse ($\hat{y}$) and the second sign for the longitudinal ($\hat{z}$) axes. The Γ denotes the insertion gamma matrix as defined in Eq. 3.47. In a similar fashion, the staple-shaped operator in the cases of $\bar{q}$ being located at $(b, -z)$, $(-b, z)$ and $(-b, -z)$ can be defined as $O^{+-}(\Gamma)$, $O^{-+}(\Gamma)$ and $O^{--}(\Gamma)$ respectively. A visual representation of these operators is shown in Fig. 4.1 in black. Due to the asymmetric nature of the staple-shaped Wilson line, there are four more operators that are obtained from the charge conjugation of the above defined four. These are also shown in Fig. 4.1, but in red, with the charge-conjugated version of $O^{\pm\pm}(\Gamma)$ denoted by $O_c^{\pm\pm}(\Gamma)$ and quark/antiquark fields having exchanged positions. For the symmetric case ($z = 0$), the charge-conjugated operators are redundant, since

$$\begin{aligned} O_c^{++} &\equiv O^{-+}, \\ O_c^{+-} &\equiv O^{--}, \\ O_c^{-+} &\equiv O^{++}, \\ O_c^{--} &\equiv O^{+-}. \end{aligned} \tag{4.1}$$

We analyze the symmetry properties using generalized parity ($\mathcal{P}_{F\alpha}^{1,2}$) and time reversal ($\mathcal{T}_{F\alpha}^{1,2}$) transformations with discrete flavor rotation, as well as charge conjugation (C), for the fermion fields in the twisted mass basis, $\chi(x_\alpha, \mathbf{x})$, and with the gauge link, $U(x_\alpha, \mathbf{x}; \alpha)$, in some direction α.The fermion fields in the physical basis, ψ are obtained through the rotation

$$\psi = \exp\left(i\omega\gamma_5\tau^3/2\right)\chi, \qquad \bar{\psi} = \bar{\chi}\exp\left(i\omega\gamma_5\tau^3/2\right). \tag{4.2}$$

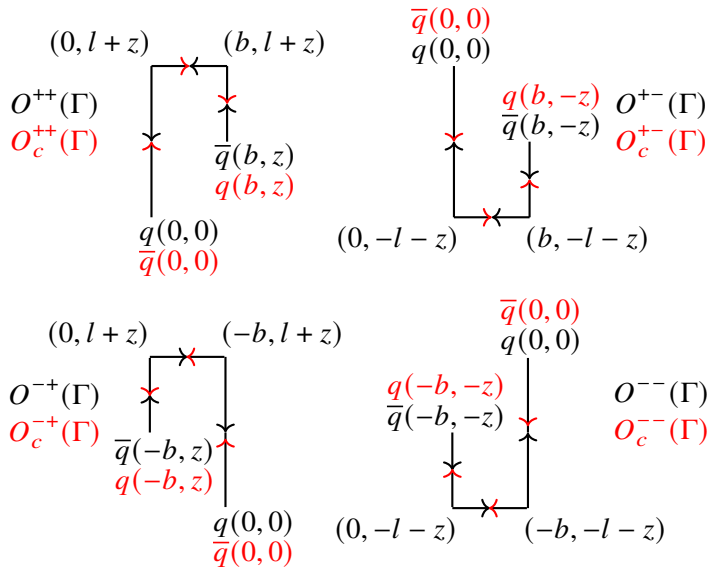

Figure 4.1: All distinct possibilities for an asymmetric staple-shaped Wilson line connecting a quark and an antiquark field spatially separated by $\pm b\hat{y}$ and $\pm z\hat{z}$ ($b, z \geq 0$).

The standard parity transformation $\mathcal{P}$ is defined as

$$\mathcal{P}: \begin{cases} U(x_0, \boldsymbol{x}; 0) \to U(x_0, -\boldsymbol{x}; 0), \\ U(x_0, \boldsymbol{x}; k \in \{1,2,3\}) \to U^{-1}(x_0, -\boldsymbol{x} - a\hat{k}; k \in \{1,2,3\}), \\ \chi(x_0, \boldsymbol{x}) \to \gamma_0 \chi(x_0, -\boldsymbol{x}), \\ \bar{\chi}(x_0, \boldsymbol{x}) \to \bar{\chi}(x_0, -\boldsymbol{x})\gamma_0, \end{cases} \tag{4.3}$$

with $U(x_\alpha, \mathbf{x}; \alpha)$ the gauge link defined in some direction α. In the twisted basis, this is only a symmetry under a discrete flavour rotation $\mathcal{F}^{1,2}$ [84],

$$\mathcal{F}^{1,2}: \begin{cases} \chi(x) \to i\tau^{1,2}\chi(x) \\ \bar{\chi}(x) \to -i\tau^{1,2}\bar{\chi}(x). \end{cases} \tag{4.4}$$

The generalized parity in the α-direction combined with discrete flavor rotation [84] is then given by

$$\mathcal{P}^{1,2}_{F\alpha}: \begin{cases} U(x_\alpha, \mathbf{x}; \alpha) \to U(x_\alpha, -\mathbf{x}; \alpha), \\ U(x_\alpha, \mathbf{x}; \beta \neq \alpha) \to U^{-1}(x_\alpha, -\mathbf{x} - a\hat{\beta}; \beta), \\ \chi(x_\alpha, \mathbf{x}) \to i\gamma_\alpha \tau_{1,2} \chi(x_\alpha, -\mathbf{x}), \\ \bar{\chi}(x_\alpha, \mathbf{x}) \to -i\bar{\chi}(x_\alpha, -\mathbf{x})\tau_{1,2}\gamma_\alpha, \end{cases} \tag{4.5}$$

where the "standard" parity is the one with $\alpha = 0$, and the 3-vector $\mathbf{x}$ is what remains from the 4-vector x after removing x_α. $\tau_{1,2}$ are the Pauli spin matrices in flavor space. Similarly, the generalized time

reversal combined with discrete flavor rotation is given by

$$\mathcal{T}^{1,2}_{F\alpha} : \begin{cases} U(x_\alpha, \mathbf{x}; \alpha) \to U^{-1}(-x_\alpha - a, \mathbf{x}; \alpha), \\ U(x_\alpha, \mathbf{x}; \beta \neq \alpha) \to U(-x_\alpha, \mathbf{x}; \beta), \\ \chi(x_\alpha, \mathbf{x}) \to i\gamma_\alpha\gamma_5\tau_{1,2}\chi(-x_\alpha, \mathbf{x}), \\ \bar{\chi}(x_\alpha, \mathbf{x}) \to -i\bar{\chi}(-x_\alpha, \mathbf{x})\tau_{1,2}\gamma_5\gamma_\alpha. \end{cases} \tag{4.6}$$

Finally, the charge conjugation transformation is given by

$$C : \begin{cases} U(x) \to (U^\dagger(x))^T, \\ \chi(x) \to C^{-1}\bar{\chi}(x)^T, \\ \bar{\chi}(x) \to -\chi(x)^T C. \end{cases} \tag{4.7}$$

The operators $O^{\pm\pm}(\Gamma)$, $O_c^{\pm\pm}(\Gamma)$ do not have definite properties with respect to the symmetries of the lattice action. Instead, one needs to consider their linear combinations, defined by

$$(ijkl)_c = i \cdot O^{++} + j \cdot O^{--} + k \cdot O^{+-} + l \cdot O^{-+} + c \cdot \left(i \cdot O_c^{++} + j \cdot O_c^{--} + k \cdot O_c^{+-} + l \cdot O_c^{-+}\right), \tag{4.8}$$

with $i, j, k, l = \pm 1$ denoting the signs of $O^{++}, O^{--}, O^{+-}, O^{-+}$, and $c = \pm 1$ representing the relative sign of the charge-conjugated versions of $O^{\pm\pm}$.

The only combinations that have definite symmetry properties are:

$$(++++)_c \equiv (----)_c,$$
$$(+-+-)_c \equiv (-+-+)_c,$$
$$(++--)_c \equiv (--++)_c,$$
$$(+--+)_c \equiv (-++-)_c,$$

i.e. the combinations with all signs i, j, k, l reversed are equivalent from the point of view of symmetry transformations, with irrelevant global phase.

As an example, we look at the symmetry properties of γ_0 and $\gamma_0\gamma_3$ given in Tables 4.1 and 4.2, respectively, restricting ourselves here to the flavor non-singlet case, $u - d$ (τ_3 matrix in flavor space). The combinations of operators that mix are those which have all signs equal in the nine rows of Tables 4.1 and 4.2. For example, the symmetry properties of $(++++)_c$ for $\Gamma = \gamma_0$ (second column of Table 4.1) are identical to the ones of the combination $(+--+)_c$ for $\Gamma = \gamma_0\gamma_3$ (last column of Table 4.2). Thus, we conclude that the following mixings occur:

$$(++++)_c \text{ with } (+--+)_c,$$
$$(+-+-)_c \text{ with } (++--)_c,$$
$$(++--)_c \text{ with } (+-+-)_c,$$
$$(+--+)_c \text{ with } (++++)_c,$$

where the first combination in a pair pertains to $\Gamma = \gamma_0$ and the second one to $\Gamma = \gamma_0\gamma_3$. Additional mixings appear with $\Gamma = \gamma_0\gamma_2$ and $\Gamma = \gamma_5\gamma_1$, thus forming a quadruple of operators that mix, $\{\gamma_0, \gamma_0\gamma_2, \gamma_0\gamma_3, \gamma_5\gamma_1\}$.

	$(++++)_c$ $(----)_c$	$(+-+-)_c$ $(-+-+)_c$	$(++--)_c$ $(--++)_c$	$(+--+)_c$ $(-++-)_c$
$\mathcal{P}^{1,2}_{F0}$	-	+	-	+
$\mathcal{P}^{1,2}_{F1}$	+	-	+	-
$\mathcal{P}^{1,2}_{F2}$	+	+	-	-
$\mathcal{P}^{1,2}_{F3}$	+	-	-	+
$\mathcal{T}^{1,2}_{F0}$	+	+	+	+
$\mathcal{T}^{1,2}_{F1}$	-	-	-	-
$\mathcal{T}^{1,2}_{F2}$	-	+	+	-
$\mathcal{T}^{1,2}_{F3}$	-	-	+	+
C	c	c	c	c

Table 4.1: Symmetry properties of operators with $\Gamma = \gamma_0$. The $\pm$ sign for $\mathcal{P}_F/\mathcal{T}_F$ transformations denotes that a given combination of staple-shaped operators is symmetric/antisymmetric with respect to the symmetry transformation given in the first column. The last row indicates symmetry properties with respect to charge conjugation, which depend on the sign c, i.e. $(\cdots)_+$ combinations are symmetric and $(\cdots)_-$ antisymmetric with respect to C in this case.

	$(++++)_c$ $(----)_c$	$(+-+-)_c$ $(-+-+)_c$	$(++--)_c$ $(--++)_c$	$(+--+)_c$ $(-++-)_c$
$\mathcal{P}^{1,2}_{F0}$	+	-	+	-
$\mathcal{P}^{1,2}_{F1}$	-	+	-	+
$\mathcal{P}^{1,2}_{F2}$	-	-	+	+
$\mathcal{P}^{1,2}_{F3}$	+	-	-	+
$\mathcal{T}^{1,2}_{F0}$	+	+	+	+
$\mathcal{T}^{1,2}_{F1}$	-	-	-	-
$\mathcal{T}^{1,2}_{F2}$	-	+	+	-
$\mathcal{T}^{1,2}_{F3}$	+	+	-	-
C	c	c	c	c

Table 4.2: Symmetry properties of operators with $\Gamma = \gamma_0\gamma_3$. See the caption of Fig. 4.1 for explanation.

For the general case, the symmetry properties for all Γ's are summarized in Table 4.3. They imply that the possible mixing is between Γ and $\{\Gamma\gamma_2, \Gamma\gamma_3, \Gamma\gamma_2\gamma_3\}$ in the asymmetric staples case. In turn,

symmetric staples restrict the mixing by eliminating always one member of the mixing quadruple, i.e. $\Gamma = \gamma_{0,1,5}$ mix with $\Gamma\gamma_2$ and $\Gamma\gamma_3$, while $\Gamma = \gamma_{2,3}$ form a triple $\{\gamma_2, \gamma_3, \gamma_2\gamma_3\}$ of operators that mix.

	γ_0	γ_1	γ_2	γ_3	1	γ_5	$\gamma_5\gamma_0$	$\gamma_5\gamma_1$
$\mathcal{P}^{1,2}_{F0}$	$-+-+$	$+-+-$	$+-+-$	$+-+-$	$-+-+$	$+-+-$	$+-+-$	$-+-+$
$\mathcal{P}^{1,2}_{F1}$	$+-+-$	$-+-+$	$+-+-$	$+-+-$	$-+-+$	$+-+-$	$-+-+$	$+-+-$
$\mathcal{P}^{1,2}_{F2}$	$++--$	$++--$	$--++$	$++--$	$--++$	$++--$	$--++$	$--++$
$\mathcal{P}^{1,2}_{F3}$	$+--+$	$+--+$	$+--+$	$-++-$	$-++-$	$+--+$	$-++-$	$-++-$
$\mathcal{T}^{1,2}_{F0}$	$++++$	$----$	$----$	$----$	$----$	$++++$	$----$	$++++$
$\mathcal{T}^{1,2}_{F1}$	$----$	$++++$	$----$	$----$	$----$	$++++$	$++++$	$----$
$\mathcal{T}^{1,2}_{F2}$	$-++-$	$-++-$	$+--+$	$-++-$	$-++-$	$+--+$	$+--+$	$+--+$
$\mathcal{T}^{1,2}_{F3}$	$--++$	$--++$	$--++$	$++--$	$--++$	$++--$	$++--$	$++--$
C	c	c	c	c	$-c$	$-c$	$-c$	$-c$

	$\gamma_5\gamma_2$	$\gamma_5\gamma_3$	$\gamma_0\gamma_1$	$\gamma_0\gamma_2$	$\gamma_0\gamma_3$	$\gamma_1\gamma_2$	$\gamma_1\gamma_3$	$\gamma_2\gamma_3$
$\mathcal{P}^{1,2}_{F0}$	$-+-+$	$-+-+$	$+-+-$	$+-+-$	$+-+-$	$-+-+$	$-+-+$	$-+-+$
$\mathcal{P}^{1,2}_{F1}$	$-+-+$	$-+-+$	$+-+-$	$-+-+$	$-+-+$	$+-+-$	$+-+-$	$-+-+$
$\mathcal{P}^{1,2}_{F2}$	$++--$	$--++$	$--++$	$++--$	$--++$	$++--$	$--++$	$++--$
$\mathcal{P}^{1,2}_{F3}$	$-++-$	$+--+$	$-++-$	$-++-$	$+--+$	$-++-$	$+--+$	$+--+$
$\mathcal{T}^{1,2}_{F0}$	$++++$	$++++$	$++++$	$++++$	$++++$	$----$	$----$	$----$
$\mathcal{T}^{1,2}_{F1}$	$++++$	$++++$	$++++$	$----$	$----$	$++++$	$++++$	$----$
$\mathcal{T}^{1,2}_{F2}$	$-++-$	$+--+$	$-++-$	$+--+$	$-++-$	$+--+$	$-++-$	$+--+$
$\mathcal{T}^{1,2}_{F3}$	$++--$	$--++$	$--++$	$--++$	$++--$	$--++$	$++--$	$++--$
C	$-c$	$-c$	c	c	c	c	c	c

Table 4.3: General symmetry properties of all possible Dirac structures. The first sign of each entry reflects the symmetry properties (+/− − symmetric/antisymmetric) of the combination $(++++)_c$ (or its equivalent $(----)_c$), the second sign concerns $(+-+-)_c$ (or $(-+-+)_c$), the third $(++--)_c$ (or $(--++)_c$) and the fourth $(+--+)_c$ (or $(-++-)_c$). The last row indicates the symmetry properties with respect to charge conjugation that depend on the sign c and are common to all combinations. The combinations that mix have the same signs in a given column (see e.g. the first column of γ_0, the second column of $\gamma_0\gamma_2$, the third column of $\gamma_5\gamma_1$ and the fourth column of $\gamma_0\gamma_3$, representing the quadruple $\{\gamma_0, \gamma_0\gamma_2, \gamma_0\gamma_3, \gamma_5\gamma_1\}$ of operators that mix relevant to this work; note that the mixing with $\gamma_5\gamma_1$ involves the combination $(++--)_{-c}$ with opposite relative sign in front of the charge-conjugated operators).

Based on the symmetry properties, we provide all the mixing sets of asymmetric ($z \neq 0$) staple-shaped operators with different Dirac structures Γ, as dictated by the generalized C, P, T symmetries of Eqs. (4.5 – 4.7), in explicit form:

- $\{1, \gamma_2, \gamma_3, \gamma_2\gamma_3\}$,
- $\{\gamma_5, \gamma_5\gamma_2, \gamma_5\gamma_3, \gamma_0\gamma_1\}$,
- $\{\gamma_0, \gamma_0\gamma_2, \gamma_0\gamma_3, \gamma_5\gamma_1\}$,

- $\{\gamma_1, \gamma_1\gamma_2, \gamma_1\gamma_3, \gamma_5\gamma_0\}$.

In the case of symmetric staple-shaped operators ($z = 0$), the mixing sets are reduced to:

- $\{\gamma_2, \gamma_3, \gamma_2\gamma_3\}$,
- $\{\gamma_5, \gamma_5\gamma_2, \gamma_5\gamma_3\}$,
- $\{\gamma_0, \gamma_0\gamma_2, \gamma_0\gamma_3\}$,
- $\{\gamma_1, \gamma_1\gamma_2, \gamma_1\gamma_3\}$,

while the remaining operators, involving the Dirac structures $1, \gamma_0\gamma_1, \gamma_5\gamma_1, \gamma_5\gamma_0$ are multiplicatively renormalizable.

We point out that different mixing patterns have been considered in recent studies, including mixing among all 16 operators of different Dirac structures [66], or at least mixing in pairs $(\Gamma, \Gamma\gamma_3)$ [115]. In our work, we choose to consider the minimal set of staple-shaped operators (of the same dimension) that are allowed to mix by the above-mentioned C, P, and T symmetries. We have not considered mixing with higher-dimensional operators allowed by Lorentz symmetry (see, e.g., Ref. [121] for the straight Wilson-line case), since it is power suppressed and not relevant when one takes the continuum limit $a \to 0$. Also, in contrast to Ref. [115], in our analysis, the staple line has been chosen to be in a 2D, and not 3D, plane in Euclidean space formed by the transverse ($\hat{y}$) and longitudinal ($\hat{z}$) directions. In this respect, we end up with a basis of 8 (instead of 16) operators, which are eigenstates of C, P and T transformations. We also note that calculations in one-loop lattice perturbation theory [114] show a smaller mixing pattern compared to the symmetries; however, this cannot guarantee a reduced mixing in higher loops.

4.2 RI/MOM

The RI/MOM scheme [122] was first adapted for non-local operators employed in the quasi-distribution approach in Refs. [116, 123]. Since the defintion of the beam function in Eq. (3.47) already contains the rectangular Wilson loop factor Z_E, which cancels the divergence arising from the staple-shaped Wilson line, we define an unsubtracted beam function for the purpose of this renormalization study,

$$B_{0,\Gamma}\left(b, l, z, P^z\right) = \left\langle H\left(P^z\right) \left| O_\Gamma(b, l, z) \right| H\left(P^z\right) \right\rangle . \tag{4.9}$$

The subscript 0 indicates that the beam function is unsubtracted, and any subsequent functions with this subscript will signify the same. The RI/MOM renormalization constants Z_O^{RI} are defined by the condition

$$\frac{Z^{\mathrm{RI}}_{\Gamma\Gamma'}(b, l, z, \mu_0; 1/a)}{Z_q^{\mathrm{RI}}(\mu_0; 1/a)} \frac{1}{12} \mathrm{Tr}\left[\frac{\Lambda_0^\Gamma(b, l, z, p; 1/a)\Gamma'}{e^{ip^z z + ip_\perp b}} \right] \Bigg|_{p=\mu_0} = 1 , \tag{4.10}$$

where Λ_0^Γ is defined in terms of the amputated Green's function

$$\Lambda_0^\Gamma(b, l, z, p; 1/a) = S_q^{-1} G^\Gamma(b, l, z, p; 1/a) S_q^{-1} , \tag{4.11}$$

with S_q the off-shell quark propagator. The Green's function is calculated as

$$G^{\Gamma}(b,l,z,p;1/a) = \langle q(p)|O^{\Gamma}(b,l,z,p;1/a)|q(p)\rangle\,. \tag{4.12}$$

Because G^{Γ}, and thus Λ_0^{Γ}, have the same divergences as $B_{0,\Gamma}$, all the divergences, in principle, cancel in the renormalization procedure. Z_q^{RI} is the quark wave function renormalization defined as

$$Z_q^{\mathrm{RI}}(\mu_0;1/a) = \frac{1}{12}\,\mathrm{Tr}\left[\left(S_q(p;1/a)\right)^{-1} S_q^{\mathrm{Born}}(p)\right]\Bigg|_{p^2=\mu_0^2}, \tag{4.13}$$

and the corresponding renormalized beam function is then

$$B_{\Gamma}^{\mathrm{RI}}(z,b,\mu_0,P^z) = \sum_{\Gamma'} Z_{\Gamma\Gamma'}^{\mathrm{RI}}(b,l,z,\mu_0;1/a) B_{0,\Gamma'}(b,l,z,P^z;1/a)\,. \tag{4.14}$$

Note that the renormalized beam function is independent of l, because the divergence associated to l gets cancelled by $^{\mathrm{RI}}_{\Gamma\Gamma'}$ and the beam function converges for large enough l, as will be shown in Chapter 6.

In principle, one could consider the subtracted beam function (B_{Γ}) for this study, but then one needs to do the similar subtraction for the Green's function. But since it gets inverted in the renormalization factor and the operators in the bare beam function and the renormalization factor have exactly the same shape of the Wilson line, the Wilson loop subtraction would cancel in the end. For this reason, we have considered the unsubtracted beam function in this section.

4.3 Short distance ratio

As we will show in Chapter 6, the effect of mixing under RI/MOM is negligible. Also RI/MOM produces some residual divergences, which make it difficult to renormalize especially at large distances. Therefore, since mixing has no effect, we can adapt a multiplicative renormalization scheme. Here we follow the approach taken in Refs. [73, 120], which they name as the Short Distance Ratio (SDR) scheme.

We first take note of the vacuum expectation value of a rectangular Wilson loop Z_E with sides $2l$ and b,

$$Z_E\,(2l,b) = \frac{1}{N_c}\left\langle W_z\,(0,2l)\,W_T\left(2l\hat{n}_z,b\right)W_z^{\dagger}\left(2l\hat{n}_z+b\hat{n}_T,2l\right)W_T^{\dagger}\left(b\hat{n}_T,b\right)\right\rangle. \tag{4.15}$$

In Figure 4.2, we show the diagrammatic representation of the Wilson loop Z_E, on the left. On the right, we show the loop divided in two parts. The top part in black corresponds exactly to the staple-shaped Wilson link as shown in Figure 3.4. The bottom part in red is identical in shape to the top part, but reflected with respect to the origin. Therefore, by construction, the rectangular loop is a product of the staple shaped link and its reflection, and hence contains twice the divergence associated with the staple-shaped link. Therefore, $\sqrt{Z_E}$ must cancel the divergences from the staple-shaped link. In particular, it should cancel the pinch-pole singularity associated with the length l of the staple, as well as the divergences associated with the cusps. Furthermore, as the sides of Z_E are also dependent on the longitudinal displacement z, the exponential divergence associated with z present

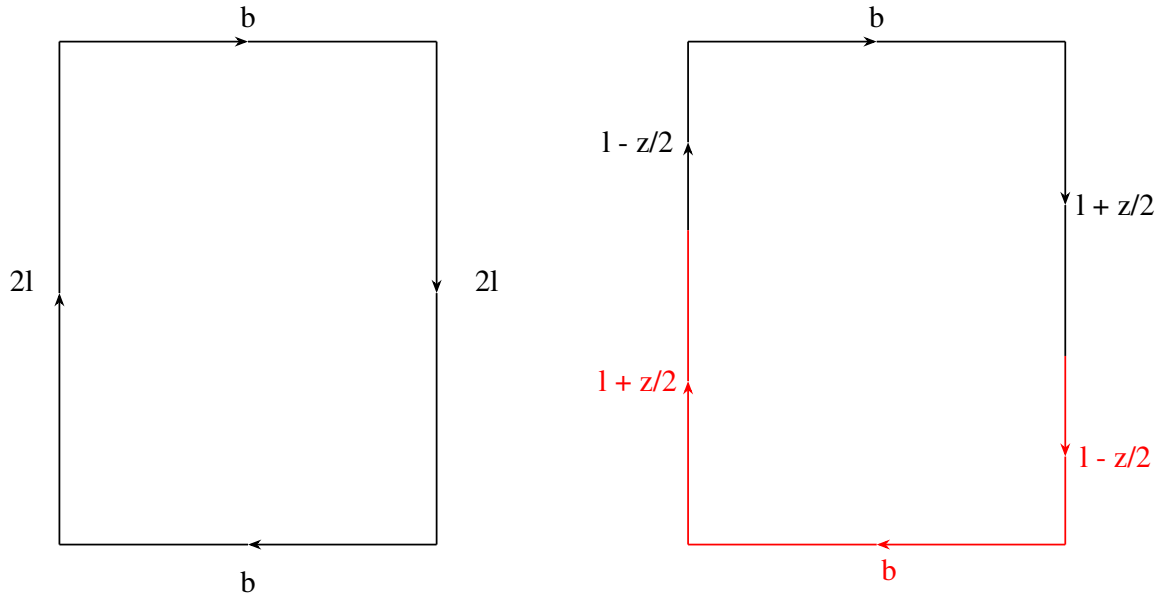

Figure 4.2: Rectangular Wilson loop (left) and the loop as a product of 2 staple-shaped links (right).

in the staple-shaped link must also be cancelled if an appropriated ratio is taken, namely the one proposed in Refs. [58, 73]:

$$B_\Gamma(z, b, P^z; 1/a) = \lim_{L\to\infty} \frac{B_{0,\Gamma}(b, l, z, P^z; 1/a)}{\sqrt{Z_E(2l, b; 1/a)}}. \tag{4.16}$$

After dividing the beam function by the square root of Z_E, the only remaining divergences are the UV divergences associated with the quark field and its end-points connecting to the gauge links. As such, they can be cancelled by taking ratios, as they have a multiplicative nature [57, 124]. Hence, one can define

$$B_\Gamma^{SDR}(z, z_0, b, b_0, P^z) = Z^{SDR}(z_0, b_0; 1/a)\, B_\Gamma(z, b, P^z; 1/a)\,, \tag{4.17}$$

where,

$$Z^{SDR}(z_0, b_0; 1/a) = \frac{1}{B_\Gamma(z = z_0, b = b_0, P^z = 0; 1/a)}\,. \tag{4.18}$$

Because the remaining divergences are independent of the length of the Wilson line, one is free to choose z_0 and b_0. In order to connect these quantities to the $\overline{\text{MS}}$ scheme via a perturbative scheme conversion, z_0 and b_0 should be small enough for perturbation theory to be valid. However, the use of small values for both z_0 and b_0 can introduce sizable discretization errors in the renormalization factors, which can affect the validity of the SDR scheme. To address this issue, different approaches can be employed in order to reduce finite lattice-spacing errors from the non-perturbative data for all values of the staple lengths b/a and z/a. Ideally, the elimination of discretization errors requires calculations of physical matrix elements at different finite values of the lattice spacing a and an extrapolation $a \to 0$. When data for multiple values of a are not available, a number of different approaches can be employed in order to reduce discretization errors at each lattice spacing. A standard

method is to apply an improved discretization, in both the action and the operators under study, using the Symanzik-improvement program [125, 126]. Another way to reduce this kind of systematic error from a lattice calculation is to subtract one-loop artifacts employing lattice perturbation theory to all orders in a, from the non-perturbative vertex functions calculated in lattice simulations. Our group has successfully applied this method to the renormalization of local quark bilinear operators [127–129], and more recently to the renormalization of non-local straight Wilson-line operators for quasi-PDFs [130]. These studies have provided a useful feedback on the effectiveness of artifacts in the renormalization factors for different ranges of the scales entering the renormalization procedure. Since this is our first non-perturbative study considering non-local staple-shaped operators we do not consider finite-a errors, but we intend to apply the method of subtracting one-loop artifacts in a future extension of our study.

The renormalized matrix elements are converted to the $\overline{\text{MS}}$ scheme using perturbation theory. We have computed the vertex, sail, and tadpole one-loop diagrams for external quark states with a general momentum p^z. For $p^z \to 0$, the conversion factor is given by [131]

$$Z^{\overline{\text{MS}},SDR}(z_0, b_0, \mu_0) = 1 + \frac{\alpha_s C_F}{2\pi}\left(\frac{1}{2} + \frac{3}{2}\ln\left(\frac{b_0^2 + z_0^2}{4e^{-2\gamma_E}}\mu_0^2\right) - 2\frac{z_0}{b_0}\arctan\frac{z_0}{b_0}\right), \tag{4.19}$$

which agrees with Eq. (6) of Ref. [73]. Note that this factor equals $B_\Gamma^{\overline{\text{MS}}}(z = z_0, b = b_0, P^z = 0, \mu_0)$. Details of this calculation for a general external momentum are presented in Ref. [131]. The renormalized beam function in the $\overline{\text{MS}}$ scheme is then given by

$$B_\Gamma^{\overline{\text{MS}}}(z, b, P^z) = Z^{\overline{\text{MS}}}(z_0, b_0, \mu_0) B_\Gamma^{SDR}(z, z_0, b, b_0, P^z). \tag{4.20}$$

4.4 RI-short

As will be shown in Chapter 6, the usual RI scheme may be problematic at large z and b as the magnitude of the Z^{RI} factors grows exponentially. Also, as shown in Refs. [73, 117], the usual RI scheme may still contain a residual linear divergence, which may not be properly canceled. On the other hand, as discussed in Section 4.3, the $\sqrt{Z_E}$ factor cancels all divergences in z and b present in the staple. Hence, we can define a vertex function that is free of such divergences,

$$\Lambda^\Gamma(z, b, p; 1/a) = \frac{\Lambda_0^\Gamma(z, b, p; 1/a)}{\sqrt{Z_E(2l, b; 1/a)}}. \tag{4.21}$$

Because the divergences related to the lengths of the Wilson line have been removed, we can compute the renormalization factors as in Section 4.3 at some fixed z_0, b_0 [115]

$$\frac{Z_{\Gamma\Gamma'}^{\text{RI-short}}(z_0, b_0, \mu_0; 1/a)}{Z_q^{\text{RI}}(\mu_0; 1/a)} \frac{1}{12} \text{Tr}\left[\frac{\Lambda^\Gamma(z, b, p; 1/a)\Gamma'}{e^{ip^z z + ibp_\perp}}\right]\Bigg|_{p=\mu_0, z=z_0, b=b_0} = 1\,. \tag{4.22}$$

The $Z^{\text{RI-short}}$ factor defined at fixed z_0 and b_0 is used to renormalize the bare B_{γ_0} defined at arbitrary values of z and b. We have labeled this procedure as RI-short. In principle, the vertex function in the

standard RI/MOM could also be modified by taking its ratio with $\sqrt{Z_E}$. This would reduce the growth of the Z-factors with increasing b. However, when combining $Z^{\rm RI}$ with the bare B_{γ_0}, the $\sqrt{Z_E}$ factors cancel each other, and therefore $\sqrt{Z_E}$ has no effect on the renormalized matrix elements. On the other hand, the $\sqrt{Z_E}$ factor appearing in the vertex function of the RI-short scheme is defined at fixed values of z and b, contrary to the $\sqrt{Z_E}$ factor appearing in the bare B_{γ_0}. Hence the cancellation of the Z_E factors do not happen in the RI-short scheme.

As in Section 4.3, we choose the pair z_0, b_0 to be in the perturbative region in order to make the perturbative conversion to the $\overline{\rm MS}$ scheme reliable. Moreover, the study of possible lattice artifacts associated with the use of small values of z_0/a and b_0/a will be considered in future extensions of our study by using one-loop lattice perturbation theory.

The corresponding renormalized beam function in this scheme is then given by

$$B_{\Gamma}^{\rm RI-short}(z, z_0, b, b_0, \mu_0, P^z) = \sum_{\Gamma'} \left[Z_O^{\rm RI-short}(z_0, b_0, \mu_0; 1/a) \right]_{\Gamma\Gamma'} B_{\Gamma'}(z, b, P^z; 1/a). \tag{4.23}$$

Finally, we can convert $B_{\Gamma}^{\rm RI-short}$ to the $\overline{\rm MS}$ scheme using one-loop perturbation theory,

$$B_{\Gamma}^{\overline{\rm MS}}(z, b, \mu_0, P^z) = \sum_{\Gamma'} \left[Z_O^{\overline{\rm MS},\rm RI-short}(z_0, b_0, \mu_0) \right]_{\Gamma\Gamma'} B_{\Gamma'}^{\rm RI-short}(z, z_0, b, b_0, \mu_0, P^z)\,. \tag{4.24}$$

The conversion matrix $Z_O^{\overline{\rm MS},\rm RI-short}$ is calculated in dimensional regularization for arbitrary values of the momentum scale μ_0. Explicit expressions for all Γ, Γ' are given in Ref. [131]. Similar perturbative studies can be found in Refs. [57, 114].

CHAPTER 5

Lattice setup

5.1 Lattice ensemble

For the lattice calculation, we use $Nf = 2+1+1$ lattice ensembles generated by the Extended Twisted Mass Collaboration (ETMC). The ensembles are generated using the Iwasaki gauge action and the twisted mass fermion action with a clover term. In this work we have used 3 lattice ensembles namely, cA211.53.24, cA211.30.32 and cB211.072.64 [86]. The details of the ensembles are given in Table 5.1. cA211.53.24 and cA211.30.32 have similar lattice spacing but different volume and sea pion masses. cB211.072.64 is at a smaller lattice spacing and is at the physical point. This combination of lattices allows us to explore discretization effects, finite volume effects and pion mass dependence. However, in this exploratory work, we will only compare the results from the different lattices qualitatively and a more systematic study will be done in the future.

name	$L^3 \times T/a^4$	a [fm]	$a\mu_l$	M_π [MeV]	$M_\pi L$	N_{conf}
cA211.53.24	$24^3 \times 48$	0.093	0.0053	350	4	600
cA211.30.32	$32^3 \times 64$	0.091	0.0030	260	4	400
cB211.072.64	$64^3 \times 128$	0.08	0.00072	130	3.6	250

Table 5.1: Details of the lattice ensembles used in this work. The columns give the names, lattice volume, lattice spacing, light quark mass, pion mass and the number of gauge configurations used.

For the quasi-TMDPDF, we will show results from all the ensembles. The quasi-TMDWF and the meson form factor have been calculated on the cA211.53.24 and cA211.30.32 ensembles. Accordingly the soft function, the Collins-Soper kernel and finally the physical TMDPDF have been calculated on these 2 ensembles. The full calculation on the cB211.072.64 ensemble is currently in progress and will soon appear in a future publication.

5.2 Matrix elements on the lattice

5.2.1 Quasi-TMDPDF

The quasi-TMDPDF and in turn the quasi-beam function contains a matrix element of the form

$$\langle N(P^z)|\, O_\Gamma(b,l,z)\, |N(P^z)\rangle\,. \tag{5.1}$$

where $N(P^z)$ is a nucleon interpolator boosted to momentum P^z in the z-direction. $O_\Gamma(b,l,z)$ is the staple-shaped operator as defined in Eq. (3.48). On the lattice, one can extract this matrix element from the ratio of a 3-point and a 2-point correlator defined as

$$\begin{aligned} C^{3pt}(t_s,\tau,0,P^z) &= \mathcal{P}_{\alpha\beta}\sum_{\boldsymbol{x},\boldsymbol{y}} e^{-iP^z x_z}\langle N_\alpha(t_s,\boldsymbol{x})O_\Gamma(\tau,\boldsymbol{y},b,l,z)\bar{N}_\beta(0,\mathbf{0})\rangle, \\ C^{2pt}(t,0,P^z) &= \mathcal{P}_{\alpha\beta}\sum_{\boldsymbol{x}} e^{-iP^z x_z}\langle N_\alpha(t,\boldsymbol{x})\bar{N}_\beta(0,\mathbf{0})\rangle. \end{aligned} \tag{5.2}$$

Here, $N_\alpha(x)$ is the nucleon interpolating operator, which in case of the proton, takes the form

$$N_\alpha(x) = \epsilon^{abc} u^a_\alpha(x)\left(d^{bT}_\beta(x)(C\gamma_5)_{\beta\gamma}u^c_\gamma(x)\right), \tag{5.3}$$

and similarly for the neutron,

$$N_\alpha(x) = \epsilon^{abc} d^a_\alpha(x)\left(u^{bT}_\beta(x)(C\gamma_5)_{\beta\gamma}d^c_\gamma(x)\right), \tag{5.4}$$

where u and d are up and down quark fields respectively. C is the charge conjugation matrix and ϵ^{abc} is the Levi-Civita symbol. This form of the nucleon interpolator comes from taking into account the different quantum numbers of a nucleon. The proton and neutron are isospin doublets with $I^z = +1/2$ and $I^z = -1/2$ respectively. They also are spin $J = 1/2$ states. The u and d combination inside the parenthesis forms a diquark with spin $J = 0$ and isospin $I = 0$. The full nucleon interpolator then has the correct quantum numbers. Summing the color indices with the Levi-Civita symbol makes the interpolator color singlet and therefore gauge invariant. A final quantum number is the parity. Using the parity projector $\mathcal{P}$, the interpolator can be projected to definite parity states $P = \pm 1$. Here we are interested in the unpolarized TMDPDF, therefore we use the parity projector as

$$\mathcal{P} = \frac{1}{2}\left(1+\gamma_0\right). \tag{5.5}$$

The time coordinate t (t_s) is the source-sink separation for the 2-point (3-point) correlator and τ is the time slice at which the operator insertion is performed.

The operator is the staple-shaped operator as defined in Eq. (3.48). In practice, we calculate the flavour non-singlet combination $u - d$, and hence one inserts a τ_3 in the flavour space in the definition

of the operator. The 3-point correlator therefore takes the explicit form

$$\begin{aligned} &C^{3pt}(t_s, \tau, 0, P^z; b, l, z) \\ &= \mathcal{P} \sum_{\boldsymbol{x},\boldsymbol{y}} e^{-iP^z x_z} \langle N(t_s, \boldsymbol{x}) \bar{q}\left(\tau, \boldsymbol{y} + b\hat{n}_T + \frac{z}{2}\hat{n}_z\right) \Gamma \mathcal{W}_{\text{staple}}\left(\boldsymbol{y}, b, l, z\right) \tau_3 q\left(\tau, \boldsymbol{y} - \frac{z}{2}\hat{n}_z\right) \bar{N}(0, \mathbf{0})\rangle. \end{aligned} \tag{5.6}$$

Here, q defines the standard up and down quark doublet. The definition of TMDPDF in Eq. (3.35) contains $\gamma^+ = (\gamma^0 + \gamma^3)/\sqrt{2}$. Therefore on the lattice, the insertion Dirac matrix Γ can be either γ_3 or γ_0, or in general, a combination of both. For the quasi-PDF case it was found that γ_0 does not mix with any other operator, while γ_3 mixes with the scalar operator [116]. This made the choice of γ_0 as the insertion operator quite trivial for the case of quasi-PDF. Here, however, as we have already shown in Sec. 4.1, no such advantage exists in this case. We therefore chose γ_0 since we observe significantly better signal-to-noise ratio compared to γ_3.

Now, we look at the exact form of the correlators at the quark level and how we can build them using individual quark propagators. Firstly, we consider the 2-point correlator.

$$\begin{aligned} C^{2pt}(x;0) &= \mathcal{P}_{\alpha\beta}\langle N_\alpha(x)\bar{N}_\beta(0)\rangle \\ &= -\mathcal{P}_{\alpha\beta}\langle \bar{N}_\beta(x)\bar{N}_\alpha(0)\rangle \\ &= -\varepsilon^{abc}\varepsilon^{a'b'c'}\mathcal{P}_{\gamma\gamma'}\langle\Omega|\bar{d}^a_\alpha(0)\left(C\gamma_5\right)_{\alpha\beta}\bar{u}^{b^T}_\beta(0)\bar{u}^c_\gamma(0) \\ &\qquad u^{a'}_{\gamma'}(x)\, d^{b'^T}_{\alpha'}(x)\left(C\gamma_5\right)_{\alpha'\beta'} u^{c'}_{\beta'}(x)\,|\Omega\rangle \\ &= -\varepsilon^{abc}\varepsilon^{a'b'c'}\left(C\gamma_5\right)_{\alpha\beta}\left(C\gamma_5\right)_{\alpha'\beta'}\mathcal{P}_{\gamma\gamma'} \\ &\quad \left\langle\Omega\left|\bar{d}^a_\alpha(0)\bar{u}^{b^T}_\beta(0)\bar{u}^c_\gamma(0)u^{a'}_{\gamma'}(x)\, d^{b'T}_{\alpha'}(x)\, u^{c'}_{\beta'}(x)\right|\Omega\right\rangle \\ &= \varepsilon^{abc}\varepsilon^{a'b'c'}\left(C\gamma_5\right)_{\alpha\beta}\left(C\gamma_5\right)_{\alpha'\beta'}\mathcal{P}_{\gamma\gamma'}S_d(x;0)^{b'a}_{\alpha'\alpha} \\ &\quad \left[S_u(x;0)^{a'b}_{\gamma'\beta}S_u(x;0)^{c'c}_{\beta'\gamma} - S_u(x;0)^{c'b}_{\beta'\beta}S_u(x;0)^{a'c}_{\gamma'\beta}\right] \end{aligned} \tag{5.7}$$

where $S_q(x)$ is the quark propagator for the quark q. So, the 2-point correlator can be obtained by calculating point-to-all quark propagators for the up and down quarks.

The 3-point correlator is more involved. Since it involves a non-local current insertion, there are more contractions to consider. The actual operator under consideration is quite complex, hence for simplicity, we consider a general operator insertion O of the form

$$O(x) = \bar{u}^a_\alpha(x)X^{ab}_{\alpha\beta}u^b_\beta(x) - \bar{d}^a_\alpha(x)X^{ab}_{\alpha\beta}d^b_\beta(x). \tag{5.8}$$

In the case of the staple-shaped operator, X would contain the Dirac matrix and the staple-shaped Wilson line. Since the internal structure of X does not change the contraction indices, we can use this

generalized approach. The 3-point correlator can then be written as

$$\begin{aligned} C^{3pt}(x,y) =& \mathcal{P}_{\alpha\beta}\langle\Omega|\varepsilon^{abc}u^a_\alpha(x)\left(d^{b^T}(x)C\gamma_5 u^c(x)\right) \\ &\times\left[\bar{u}^f_\mu(y)\,X_{\mu\nu}u^f_\nu(y) - \bar{d}^f_\mu(y)\,X_{\mu\nu}d^f_\nu(y)\right] \\ &\times\varepsilon^{a'b'c'}\left(\bar{d}^{a'}(0)\left(C\gamma_5\right)\bar{u}^{b'^T}(0)\right)\bar{u}^{c'}_\beta(0)|\Omega\rangle \end{aligned} \tag{5.9}$$

Note that for ease of reading, we have only written the open Dirac indices explicitly. Taking all possible Wick contractions into account, we find that the 3-point correlator can be split into 2 parts,

$$C^{3pt}(x,y) = U(x;y) - D(x;y). \tag{5.10}$$

We call them the up-part and down-part based on which current insertion is considered. Both these terms contain fully connected as well as disconnected diagrams. However, due to isospin symmetry, the disconnected parts are identical in U and D. Therefore, they cancel out in the 3-point correlator, and we are left with only the connected parts. The connected part of D is given by

$$\begin{aligned} D_{\text{conn}}(x;y) = \varepsilon^{abc}\varepsilon^{a'b'c'}&\left[(C\gamma_5)^T S_d(x;y)XS_d(y,0)(C\gamma_5)\right]^{ba'}_{\delta\delta'} \\ &\times\mathcal{P}_{\alpha\beta}\left\{S_u(x;0)^{ac'}_{\alpha\beta}S_u(x;0)^{cb'}_{\delta\delta'} - S_u(x;0)^{ab'}_{\alpha\delta'}S_u(x;0)^{cc'}_{\delta\beta}\right\}. \end{aligned} \tag{5.11}$$

One can construct a similar albeit longer expression for the up-part as well. The existence of $S_d(x;y)$ in the expression suggests that one would need to calculate all-to-all propagators for the 3-point function. This is not feasible computationally. We will show an alternative method in section 5.3.3.

One finally obtains the unsubtracted quasi-beam function by taking the ratio of the 3-point and 2-point functions as [72]

$$\frac{C^{3pt}(t_s,t)}{C^{2pt}(t_s)} \approx \frac{B_{0,\Gamma} + c_2(e^{-\Delta E t} + e^{-\Delta E(t_s-t)}) + c_3 e^{-\Delta E t_s}}{1 + c_1 e^{-\Delta E t_s}}, \tag{5.12}$$

where $B_{0,\Gamma} = B_{0,\Gamma}(b,l,z,P^z)$, ΔE is the mass gap between the ground state and the excited state, and c_i are parameters that depend on the excited state contamination.

5.2.2 Quasi-TMDWF

The unsubtracted quasi-TMDWF takes the form

$$\tilde{\psi}_{0,\Gamma}(b,l,z,P^z) = \langle\Omega|\,O_\Gamma(x,b,l,z)\,|\pi(P^z)\rangle\,. \tag{5.13}$$

Here O_Γ is again the staple-shaped operator as defined in Eq. (3.48) and $\pi(P^z)$ is the pion interpolator with momentum P^z in the z-direction. In order to extract this matrix element, we need to construct the following 2-point correlator

$$C^{2pt}_\pi(b,l,z,t,P^z) = \sum_{\boldsymbol{x}} e^{-iP^z x_z}\langle O_\Gamma(x,b,l,z)O^\dagger_\pi(0,P^z)\rangle. \tag{5.14}$$

Here, O_Γ is the staple-shaped operator as defined in the case of quasi-TMDPDF and O_π is pion interpolator defined as

$$O_\pi^\dagger(t, P^z) = \sum_{\boldsymbol{x},\boldsymbol{y}} \bar{u}(t, \boldsymbol{x})\gamma_5 d(t, \boldsymbol{y}) e^{iP^z y_z}. \tag{5.15}$$

These can be calculated from coulomb-gauge-fixed wall sources at fixed time slices. Each of the 2 quarks carry half the momenta ($P^z/2$). The exact contraction of the propagators takes the following form

$$\begin{aligned} C_\pi^{2pt}(b, l, z, t, P^z) =& \frac{1}{L^3}\sum_{\boldsymbol{x}} e^{iP^z x_z} \mathrm{Tr}\Big[S_u^\dagger(t, \boldsymbol{x} + b\hat{n}_T + \frac{z}{2}\hat{n}_z; 0; -P^z/2)\Gamma \\ & \mathcal{W}_{staple}(\boldsymbol{x}, b, l, z) S_u(t, \boldsymbol{x} - \frac{z}{2}\hat{n}_z; 0; P^z/2)\Big]. \end{aligned} \tag{5.16}$$

Similar to the case of the quasi-TMDPDF, the insertion operator Γ can be either $\gamma_5\gamma_0$ or $\gamma_5\gamma_3$, which approaches the $\gamma_5\gamma^+$ in the light-cone limit. The deviation between the two is power-suppressed and one can choose the combination $(\gamma_5\gamma_0 + \gamma_5\gamma_3)/2$ to minimize power corrections [69]. But it was demonstrated in [69] that the corrections are of the order of 5%. Therefore, in this work, we only consider the $\gamma_5\gamma_0$ case.

Finally, the unsubtracted quasi-TMDWF is related to the 2-point correlator as [64, 69]

$$C_\pi^{2pt}(b, l, z, t, P^z) = \frac{A_w(P^z)}{2E}\tilde{\psi}_{0,\Gamma}(b, l, z, P^z) e^{-E_\pi t}[1 + c_0(b, l, z, P^z)e^{-\Delta E_\pi t}], \tag{5.17}$$

where $A_w(P^z)$ is the overlap amplitude of the pion operator and c_0 contains the excited state contributions. Taking a ratio with the ultra-local case, the overlap operator gets cancelled and the quasi-TMDWF can be extracted as

$$\frac{C_\pi^{2pt}(b, l, z, t, P^z)}{C_\pi^{2pt}(0, 0, 0, t, P^z)} \approx \tilde{\psi}_{0,\Gamma}(b, l, z, P^z)[1 + c_0(b, l, z, P^z)e^{-\Delta E_\pi t}]. \tag{5.18}$$

5.2.3 Meson form factor

The 3-point correlator required to extract the meson form factor can be directly derived from the hadronic matrix element as

$$C_\pi^{3pt}(t, t_s, b, P^z) = \sum_{\boldsymbol{x}} e^{-i2P^z x_z}\langle O_\mu(t_s, -P^z)\bar{u}(t, \boldsymbol{x} + b\hat{n}_T)\Gamma u(t, \boldsymbol{x} + b\hat{n}_T)\bar{d}(t, \boldsymbol{x})\Gamma d(t, \boldsymbol{x}) O_\pi^\dagger(0, P^z)\rangle. \tag{5.19}$$

The pion operator O_π is the same as defined in the quasi-TMDWF case. The wick contractions are straight-forward and the 3-point correlator can be written as

$$C_\pi^{3pt}(t_s, \tau, b, P^z) = \frac{1}{L^3}\sum_{\boldsymbol{x}} e^{iP^z x_z}\mathrm{Tr}\Big[S_u^\dagger(t_s, \boldsymbol{x} + b\hat{n}_T; 0; -P^z)\Gamma S_u(t, \boldsymbol{x}; 0; P^z) S_d^\dagger(t_s, \boldsymbol{x}; 0; P^z)\Gamma S_d(t, \boldsymbol{x}; 0; -P^z)\Big]. \tag{5.20}$$

At large time limit ($0 \ll t \ll t_s$), we can extract the meson form factor from the ratio [65]

$$\frac{C_\pi^{3pt}(t_s, \tau, b, P^z)}{2[C_\pi^{2pt}(0, 0, 0, t_s/2, P^z)]^2} = F(b, P^z)\frac{1 + c_1(e^{-\Delta E t} + e^{-\Delta E(t_s - t)})}{1 + c_2 e^{-\Delta E t_s/2}}. \tag{5.21}$$

Ref. [64] showed that one can use a Fierz rearrangement of the four-quark operators to reduce higher twist effects and Ref. [65] showed that the combination $\mathbb{1} - \gamma_5$ has additional UV divergences whereas the combination $\gamma_\perp + \gamma_5\gamma_\perp$ does not. Hence, in this work we have focused on the latter combination for the form factor.

5.3 Propagators

In the previous section we showed how matrix elements can be extracted from 2-point and 3-point correlators in Euclidean field theory. The basic building block of all these correlators are quark propagators. The propagator provides the probability amplitude for a quark to propagate from one point to another. In path integral formalism, it is simply the inverse of the Dirac operator.

$$S^{ab}_{\alpha\beta}(x;y) = {D^{-1}}^{ab}_{\alpha\beta}(x;y) = \langle\Omega|\, \psi^a_\alpha(y)\bar{\psi}^b_\beta(x)\, |\Omega\rangle\,. \tag{5.22}$$

However, calculating the most general quark propagator ($\forall x, y$) is computationally infeasible. Since, if the Dirac spinor has

$$n = V[\text{lattice volume}] \times 4[\text{spin}] \times 3[\text{colour}] \times 2[\text{complex}] \tag{5.23}$$

degrees of freedom, then the Dirac matrix has n^2. Even for the smallest lattice under discussion ($24^3 \times 48$), this results in a system with 10^7 unknowns. Many different methods have been developed to tackle this problem. In the following sections, we will discuss the methods used in this work.

5.3.1 Point-to-all propagators

The simplest method is to use the translational invariance and fix the source of the propagator at fixed spacetime point x. This reduces the task of computing the entire inverse of the Dirac matrix to only solving 12 inversions (4 spin $\times$ 3 color). The 12 linear systems to be solved are of the following form

$$\sum_y D(x;y)^{ab}_{\alpha\beta}\psi(y)^b_\beta[z,\gamma,c] = \xi(x)^a_\alpha[z,\gamma,c], \tag{5.24}$$

where $\xi(x)$ is the point source defined at x with the property

$$\xi(x)^a_\alpha[z,\gamma,c] = \delta^{(4)}(x-z)\delta_{\alpha\gamma}\delta_{ac}. \tag{5.25}$$

The point-to-all propagator is then the inversion ϕ ($\equiv D^{-1}\xi$),

$$S(x;y)^{ab}_{\alpha\beta} = \phi(y)^b_\beta[x,\alpha,a]. \tag{5.26}$$

To reduce statistical uncertainty, one needs to use multiple source positions for each gauge configuration and average over them.

5.3.2 Timeslice-to-all propagators

Another way of calculating propagators is to use a timeslice source instead of a point source. In this case one fixes the source at a single timeslice t_0 instead of a spacetime x. So the propagator can be

calculated from any point $\boldsymbol{x}$ on the timeslice t_0 to any other point y on the lattice. The linear system to be solved is

$$\sum_y D(x;y)^{ab}_{\alpha\beta}\psi(y)^b_\beta[t_0] = \xi(x)^a_\alpha[t_0], \tag{5.27}$$

where $\xi(x)$ is the timeslice source defined at t_0 as

$$\xi(x)^a_\alpha[t_0] = \delta(x_0 - t_0)\eta(\boldsymbol{x})^a_\alpha. \tag{5.28}$$

Here, η are vectors of random number that satisfy the property

$$E\left[\eta^*(\boldsymbol{x})^a_\alpha\eta(\boldsymbol{y})^b_\beta\right] = \delta^{(3)}(\boldsymbol{x}-\boldsymbol{y})\delta_{\alpha\beta}\delta_{ab}. \tag{5.29}$$

Here E denotes the stochastic expectation. A simple choice for η could be $\eta \in \mathbb{Z}_2$ (i.e. ± 1) or $\eta \in \mathbb{Z}_2 \times \mathbb{Z}_2$ (i.e. $(\pm 1 \pm i)/\sqrt{2}$). These choices satisfy the given condition. Hence, one can define a number of time-slice sources for each gauge configuration and average over them to reduce statistical uncertainty.

5.3.3 Sequential propagators

The propagators discussed above are enough for building the 2-point correlators, and also the 3-point function for the form factor. However, the 3-point function necessary for the quasi-TMDPDF is more complex. Due to the momentum projection, we have a sum over all sink ($\boldsymbol{x}$) and insertion ($\boldsymbol{y}$) points and involves propagators like $S_{u/d}(x;y)$. It seems one needs to calculate all-to-all propagators for this case. One solution for this is to use what are called sequential propagators [132].

The basic idea is to consider two propagators which are connected at a single spatial point which is summed over, for example

$$\sum_y S(x;y)\Gamma S(y;z). \tag{5.30}$$

This volume sum can then be carried over through an inversion of the Dirac operator by constructing an appropriate sequential source using the point-to-all propagator. For example we consider the $\bar{d}Xd$ insertion in the 3-point correlator for the quasi-TMDPDF. This corresponds to the down-part as shown in Eq. (5.11). Doing some algebra, we can rewrite the down-part as a product of 2 terms.

$$\sum_{\boldsymbol{xy}} XS_d(y;0)^{da'}_{\mu\nu} S_d(x;y)^{bd}_{\kappa\mu} e^{-i\boldsymbol{P}\cdot\boldsymbol{x}} P(x;0)^{ab'}_{\kappa\nu}, \tag{5.31}$$

where

$$\begin{aligned} P(x;0)^{ba'}_{\kappa\nu} =& \mathcal{P}_{\alpha\beta}\varepsilon^{abc}\varepsilon^{a'b'c'}\left\{\left[(C\gamma_5)S_u(x;0)(C\gamma_5)^T\right]^{cb'}_{\kappa\nu} S_u(x;0)^{ac'}_{\alpha\beta}\right. \\ &\left. - \left[(C\gamma_5)S_u(x;0)\right]^{cc'}_{\kappa\beta}\left[S_u(x;0)(C\gamma_5)^T\right]^{ab'}_{\alpha\nu}\right\}. \end{aligned} \tag{5.32}$$

Using γ_5 hermiticity, we get

$$\sum_{\boldsymbol{xy}} XS_d(y;0)^{da'}_{\mu\nu}\left[\gamma_5 S_u^*(y;x)\right]^{db}_{\mu\kappa}\left[\gamma_5 P(x;0)\right]^{ab'}_{\kappa\nu} e^{-i\boldsymbol{P}\cdot\boldsymbol{x}}. \tag{5.33}$$

We can define the sequential source as

$$\xi(x)^{ab'}_{\kappa\nu} = \left[\gamma_5 P(x;0)\right]^{*ab'}_{\kappa\nu} e^{i\boldsymbol{P}\cdot\boldsymbol{x}}. \tag{5.34}$$

Inverting the Dirac operator on this source, we get the sequential propagator

$$\begin{aligned} S_{seq}(y;0) &= \sum_{\boldsymbol{x}} S_u(y;x)\xi(x) = \sum_{\boldsymbol{x}} S_u(y;x)\left[\gamma_5 P(x;0)\right]^* e^{i\boldsymbol{P}\cdot\boldsymbol{x}}. \\ \implies \left[\gamma_5 S_{seq}(y;0)\right]^* &= \sum_{\boldsymbol{x}} \left[\gamma_5 S_u(y;x)\right]^* \gamma_5 P(x;0) e^{-i\boldsymbol{P}\cdot\boldsymbol{x}}. \end{aligned} \tag{5.35}$$

This matches with what we have in Eq. (5.33). The down-part can then be computed as

$$\sum_{\boldsymbol{y}} \mathrm{Tr}\left[X S_d(y;0)\left\{\gamma_5 S_{seq}(y;0)\right]^*\right\}. \tag{5.36}$$

One can follow a similar procedure for the $\bar{u}Xu$ insertion as well. One important aspect of this method is that the sequential source depends on the sink x and the momentum p. Therefore, by construction, the momentum $\boldsymbol{p}$ and the time slice of the sink t_s gets fixed after the inversion. To vary either of these parameters, one needs to construct a new sequential source and invert the Dirac operator again. But the advantage of this method is that the sequential source does not depend on the insertion matrix X. This means, one does not need to repeat the inversion for each shape of the staple under calculation. This makes it possible to calculate a single sequential propagator and use it for all the different shapes of the staple.

5.4 Smearing

Smearing is a standard practice in lattice QCD to improve the signal-to-noise ratio in correlators. There are many different smearing techniques available. They are used to optimize the overlap of the interpolating operator with the ground state and reduce excited state contamination. In this work, we use APE smearing on the gauge links and Wuppertal smearing at the source and sink of quark propagators. We also use momentum smearing on the propagators to improve signal quality at large boost. Stout smearing is used on the gauge links entering into the construction of the staple shaped link to reduce power divergences usually present in the non-local operators.

5.4.1 APE smearing

APE smearing [133] is one of earliest introduced smearing techniques in lattice QCD. This reduces excited state effects in the correlators. In this method, the gauge links are scaled by the average of the staples connecting the same endpoints. The APE smearing step replaces the link as

$$U_\mu(x) \to U_\mu(x) + \alpha_{APE} \sum_{\nu\neq\mu} C_{\mu\nu} \tag{5.37}$$

where

$$C_{\mu\nu} = U_\nu(x)U_\mu(x+\hat{\nu})U_\nu(x+\hat{\mu}) + U_\nu(x-\hat{\mu})^\dagger U_\mu(x-\hat{\nu})U_\nu(x-\hat{\nu}+\hat{\mu}). \tag{5.38}$$

α_{APE} is the smearing parameter. After every smearing step, the link is projected back to $SU(3)$. In this work, we perform 50 steps of APE smearing with $\alpha_{APE} = 0.5$ for all point-to-all propagators.

5.4.2 Wuppertal smearing

For correlators built from point sources, it is difficult to suppress excited state contaminations at moderate time separations. However, going to larger time slices, we encounter poor signal-to-noise ratio, which is especially a problem for the nucleon correlation functions. A standard method in lattice QCD to suppress excited states in point-to-all propagators, is to use Wuppertal smearing [134].

In this method, the point source is smeared as follows

$$\xi_{sm}(t, \boldsymbol{x}) = \sum_{\boldsymbol{y}} F(\boldsymbol{x}, \boldsymbol{y}; U(t))\xi(t, \boldsymbol{y}), \tag{5.39}$$

where

$$F(\boldsymbol{x}, \boldsymbol{y}; U(t)) = \delta^{(3)}(\boldsymbol{x} - \boldsymbol{y}) + \alpha_{WUP} H(\boldsymbol{x}, \boldsymbol{y}; U(t)). \tag{5.40}$$

Here, α_{WUP} is the smearing parameter and H is the hopping matrix

$$H(\boldsymbol{x}, \boldsymbol{y}; U(t)) = \sum_{\mu=1}^{3} \left[U_\mu(t, \boldsymbol{x})\delta^{(3)}(\boldsymbol{y} - (\boldsymbol{x} + \hat{\mu})) + U_\mu^\dagger(t, \boldsymbol{x} - \hat{\mu})\delta^{(3)}(\boldsymbol{y} - (\boldsymbol{x} - \hat{\mu})) \right]. \tag{5.41}$$

For the quark field $q(x)$, this corresponds to the transformation

$$q(x) \to \frac{1}{1 + 6\alpha_{WUP}} \left[q(x) + \alpha_{WUP} \sum_{j=\pm1}^{\pm3} U_j(x) q(x + \hat{j}) \right]. \tag{5.42}$$

This smearing is applied to both source and sink of the propagator. We apply 50 steps of Wuppertal smearing with $\alpha_{WUP} = 4$.

5.4.3 Stout smearing

Stout smearing [135] is applied to the gauge links entering into the construction of the staple-shaped link. This is an analytic smearing technique constructed by taking the weighted sum of staples of the original link, as

$$C_\mu(x) = \sum_{\nu \neq \mu} \rho_{\mu\nu} \left[U_\nu(x) U_\mu(x + \hat{\nu}) U_\nu^\dagger(x + \hat{\mu}) + U_\nu^\dagger(x - \hat{\nu}) U_\mu(x - \hat{\nu}) U_\nu(x - \hat{\nu} + \hat{\mu}) \right]. \tag{5.43}$$

$\rho_{\mu\nu}$ are real valued smearing parameters. The matrix $Q_\mu(x)$ is then constructed as

$$Q_\mu(x) = \frac{i}{2} \left(\Omega_\mu^\dagger(x) - \Omega_\mu(x) \right) - \frac{i}{2N} \mathrm{Tr} \left(\Omega_\mu^\dagger(x) - \Omega_\mu(x) \right), \tag{5.44}$$

where

$$\Omega_\mu(x) = C_\mu(x) U_\mu^\dagger(x). \tag{5.45}$$

By construction, $Q_\mu(x)$ is traceless and Hermitian, therefore $e^{iQ_\mu(x)}$ is an element of $SU(3)$. The smearing step of the gauge links then are given by

$$U_\mu(x) \to e^{iQ_\mu(x)} U_\mu(x). \tag{5.46}$$

Due the property just mentioned, the new link is also in $SU(3)$ and hence no further projection is necessary. The most common choice for the smearing parameter is

$$\rho_{\mu\nu} = \rho_{stout}. \tag{5.47}$$

In case of purely spatial smearing, the parameters in the time direction are set to zero, i.e.

$$\rho_{\mu 0} = \rho_{0\nu} = 0. \tag{5.48}$$

Previous work [64] found that 5 steps of stout smearing is an optimal setup for the staple-shaped links. We use the same setup with $\rho = 0.129$.

5.4.4 Momentum smearing

Any calculation of partonic distributions require computing matrix elements at large momentum boosts. But larger boosts lead to worse signal-to-noise ratio in the correlators. To improve the signal quality at large boosts, a novel technique was proposed in [136]. This method is known as momentum smearing. This is essentially an extension of Wuppertal smearing that takes the momentum into account. The smearing applied to the quark field takes the form

$$q(x) \to \frac{1}{1+6\alpha}\left[q(x) + \alpha \sum_{j=\pm 1}^{\pm 3} U_{\hat{j}}(x) e^{-i\xi \boldsymbol{P}\cdot\hat{j}} q(x+\hat{j})\right]. \tag{5.49}$$

P is the hadron momentum. ξ is the smearing parameter.

This technique has been quite successful for the quasi-PDF case and previous work on this [137] found an optimal setup of $\xi = 0.6$ for the nucleon. We use the same setup for the quasi-TMDPDF calculation.

5.5 Computation of the staple-shaped link

The key part of TMDPDFs is the staple-shaped link which connects the quarks in the non-local operator that defines the quasi-TMDPDF and quasi-TMDWF. The shape of this staple depends on 3 parameters l, b and z. The staple-shape is a result of a product of 3 straight gauge links of length $l - z/2$ in the longitudinal direction, b in the transverse direction and $l + z/2$ in the opposite longitudinal direction respectively. The straight line on the lattice is just a product of the gauge links connecting the 2 lattice sites.

$$W_\mu(\boldsymbol{x}, l) = \prod_{i=0}^{l-1} U_\mu(\boldsymbol{x} + i\hat{z}), \tag{5.50}$$

where μ can be any particular direction.

So, for any given value of l, b and z, the staple-shaped link has a length of $2l + b + z$. Therefore, to construct such a staple, one needs to perform $2l + b + z$ products of $SU(3)$ fields defined on the whole lattice. If we want to calculate different shapes of the staple corresponding to $l = 0, 1, 2, ...l_{\text{max}}$, $b = 0, 1, 2, ...b_{\text{max}}$ and $z = 0, 1, 2, ...z_{\text{max}}$, we need to perform

$$\frac{l_{\text{max}}(l_{\text{max}} + 1)}{2} \times \frac{b_{\text{max}}(b_{\text{max}} + 1)}{2} \times \frac{z_{\text{max}}(z_{\text{max}} + 1)}{2} \tag{5.51}$$

such multiplications. In general, constructing N_{staple} different staple shapes would result in $O(N^2_{staple})$ products of $SU(3)$ fields, if we build each staple from scratch. This is computationally expensive. Especially as we go to larger lattices, the expense increases exponentially.

One solution is to calculate the staple-shaped link once and store it in memory. This is possible since the staple does not depend on the momentum, source or sink positions. So the stored staple can be used repeatedly as long as the longitudinal and transverse directions don't change. However, even for the smallest lattice of size $24^3 \times 48$, a single staple-shaped link would require ~ 80 MB of memory. Considering that we need hundreds of different staple shapes (not even considering different directions of the boost and transverse directions) for each gauge configuration, this is certainly not feasible in terms of available storage bandwidth. Moreover, if we take into account the bottleneck of loading and unloading these staples from and to disk, this method is not practical.

As a part of this thesis, I have developed an algorithm to solve this problem. The basic idea is to divide the staple into 3 parts, which are the straight Wilson lines as already mentioned, and build them individually step by step. The algorithm goes as follows. (For clarity, we use the notation z' to denote $z/2$)

(i) Iterate over values of l from 0 to l_{max}. For every increment of l, multiply the next link in the longitudinal direction to the existing line.

(ii) For every value of l, iterate over values of z' from 0 to z'_{max}. For every increment of z', build 2 longitudinal lines one of length $l - z'$ and the other of length $l + z'$.

(iii) For every value of l and z', iterate over values of b from 0 to b_{max}. For every increment of b, multiply the next link in the transverse direction to one of the longitudinal line.

(iv) Shift the other longitudinal line in the transverse direction by b and multiply it to the existing L-shaped line to get the staple shape.

Of course, one has to be careful with the direction of these individual steps and need to be consistent to form the correct staple shape. The algorithm steps are illustrated in Figure 5.1. A pseudo-code for the algorithm is described in Algorithm 1.

Following this algorithm, we need to do 1 product for each step of l, 2 products for each step of z' and b. This results in a total of $4 \cdot l_{\text{max}} \cdot z'_{\text{max}} \cdot b_{\text{max}}$ products of $SU(3)$ fields. And in general, for computing N_{staple} different staple shapes, the total number of products required is now $O(N_{staple})$. This is a significant reduction in the number of products and the effect can be easily observed in the computation time. In Figure 5.2, we show the performance of this optimized algorithm compared to the unoptimized one (where each staple is built from scratch). We show the time taken to build all the staple shapes using one gauge configuration from the ensembles cA211.53.24 and cB211.072.64, setting l_{max}, b_{max} and z'_{max} to half of the corresponding spatial lattice extent. The "v1" in the figure

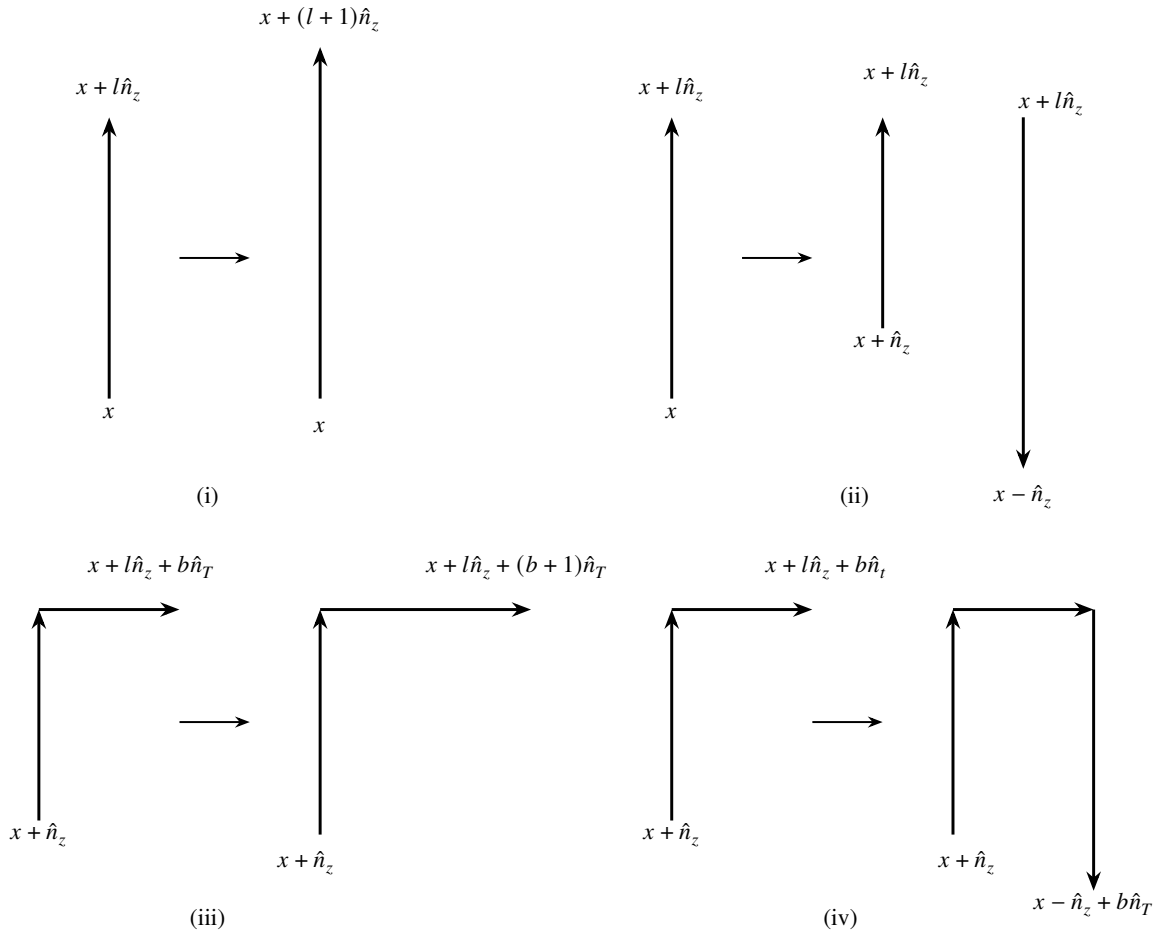

Figure 5.1: Illustration of the algorithm to construct the staple-shaped link. The algorithm is divided into 4 steps (i) Multiply the next link in the longitudinal direction, (ii) Build 2 longitudinal lines, (iii) Multiply the next link in the transverse direction and (iv) Shift the other longitudinal line in the transverse direction and multiply it to the existing L-shaped line.

is the algorithm presently described and "v2" is also using the current algorithm but building the transverse line in both the transverse directions ($\hat{n}_x$ and $\hat{n}_y$ in case the boost is along $\hat{n}_z$) at the same time. The time there is scaled by a factor of 0.5 to account for the fact that the total number of staples built is double.

Using this algorithm, for a fixed momentum and source-sink separation, we build the staples for positive and negative l, positive and negative b for both the transverse directions and positive and negative z'. We then repeat this by taking the boost along both positive and negative $\hat{n}_x$, $\hat{n}_y$ and $\hat{n}_z$ directions. All of this is averaged over for each gauge configuration to reduce statistical uncertainty. This results in a total of

$$N_{conf} \times N_{src} \times 6[\text{directions of boost}] \times 2[\pm l] \times 4[\pm b] \times 2[\pm z'] \tag{5.52}$$

measurements, where N_{src} is the number of source positions used for each gauge configuration.

Algorithm 1 Algorithm to construct the staple-shaped link

$W_1(x) = \mathbb{1}$
for $l = 0, 1, 2, ...l_{\max}$ **do**
  $W_1(x) \leftarrow W_1(x) \times U_z(x + l\hat{n}_z)$
  $W_2(x) \leftarrow W_1(x)$
  $W_3(x) \leftarrow W_1^{\dagger}(x)$
  for $z' = 0, 1, 2, ...z'_{\max}$ **do**
    $W_2(x) \leftarrow W_2(x) \times U_z^{\dagger}(x + z'\hat{n}_z)$
    $W_3(x) \leftarrow W_3(x) \times U_z^{\dagger}(x - (z' + 1)\hat{n}_z)$
    $W_4(x) \leftarrow W_2(x)$
    for $b = 0, 1, 2, ...b_{\max}$ **do**
      $W_4(x) \leftarrow W_4(x) \times U_T(x + l\hat{n}_z + b\hat{n}_T)$
      $W_3(x) \leftarrow W_3(x - \hat{n}_T)$
      $W_{staple}(x) \leftarrow W_4(x) \times W_3(x)$
    end for
  end for
end for

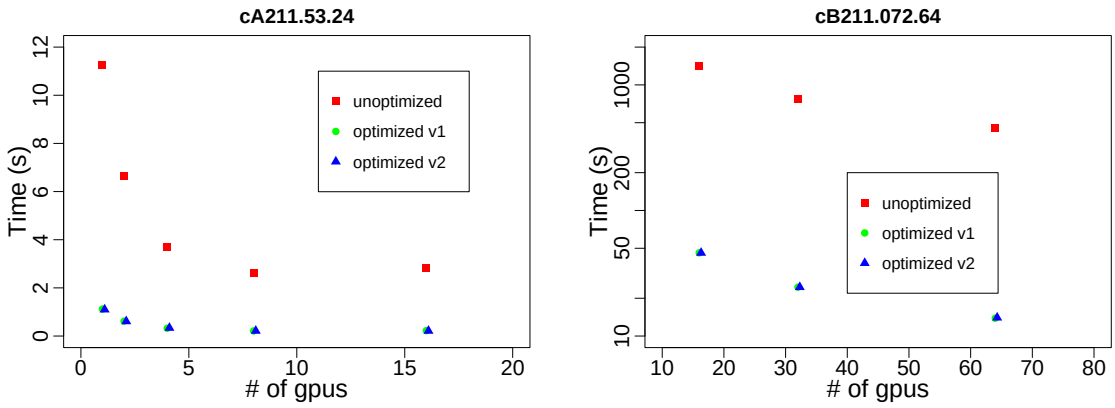

Figure 5.2: Comparison of the performance of the unoptimized and optimized staple building code. Note that in the right plot, the y-axis is made logarithmic in order to better visualize the scaling of the optimized code with number of GPUs.

CHAPTER 6

Results

In this chapter we will present the results obtained for the different observables on the lattice as discussed previously. We will start with the quasi-TMDPDF. Then we will discuss the renormalization of the staple-shaped operator and show the results for the three different approaches mentioned in Chapter 4. The results for the quasi-TMDWF will follow that. We will also discuss the results for the Collins-Soper kernel and the reduced soft function. Finally, we will perform the matching and show the results for the physical TMDPDF.

For all the computations presented in this work, we have built code for contractions using the library `PLEGMA` [138] (private repository maintained by the University of Cyprus and The Cyprus Institute), which is a GPU-enabled, memory distributed software package for lattice QCD calculations. For the propagator calculations, `PLEGMA` uses the MG solver implemented in the `QUDA` library [139–142]. Most of the computations were performed on the `QBiG` gpu cluster at Helmholtz Institut für Strahlen- und Kernphysik (HISKP) at the University of Bonn. A part of the production for the cA211.30.32 ensemble was performed in the scalable gpu partition of the `Marvin` cluster at the High Performance Computing Center of University of Bonn and at the `Cyclone` cluster of The Cyprus Institute under the project `p146`. The computation for the physical point ensemble (cB211.072.64) has been done at the `Booster` partition of the `Juwels` supercomputer at the Jülich Supercomputing Centre (JSC) under the project id `TMDPDF1`.

The post-production analysis has been done mainly using `R` [143] with the help of the `hadron` [144] library. For part of the analysis `Julia` [145] and `Python` [146] have also been used.

6.1 quasi-TMDPDF

$$f^{TMD}(x,b,\mu,\zeta) = H_f(\frac{\zeta_z}{\mu^2})\, e^{-\ln\left(\frac{\zeta_z}{\zeta}\right)K(b,\mu)}\, S_r^{\frac{1}{2}}(b,\mu)\, \tilde{f}(x,b,\mu,\zeta_z) + O\left(\frac{\Lambda_{QCD}}{\zeta_z}, \frac{M^2}{(P^z)^2}, \frac{1}{b^2\zeta_z}\right) \tag{6.1}$$

6.1.1 Bare quasi-beam function

The main ingredient in the calculation of the TMDPDF is the quasi-TMDPDF, which is obtained from the quasi-beam function calculated on the lattice. As a quick reminder, the "unsubtracted" quasi-beam

function can be extracted from the ratio of a 3-point and a 2-point nucleon correlator.

$$\frac{C^{3pt}(t_s, t, 0, P^z; b, l, z)}{C^{2pt}(t_s, 0, P^z)} \approx \frac{B_{0,\Gamma}(b, l, z, P^z) + c_2(e^{-\Delta E t} + e^{-\Delta E(t_s - t)}) + c_3 e^{-\Delta E t_s}}{1 + c_1 e^{-\Delta E t_s}}. \tag{6.2}$$

In Figure 6.1 we show the real and imaginary parts of such a ratio for 2 different staple shapes for the cA211.53.24 ensemble. In principle, one can perform a 2-state fit according to Eq. (6.2) to extract the bare quasi-beam function. But for large enough time separation ($0 << t << t_s$), we expect the excited state contamination to be negligible. We do observe a plateau in the ratio for the time slices $(t - t_s/2)/a \in [-2, 2]$ and therefore perform a constant fit in this range to extract $B_{0,\Gamma}(b, l, z, P^z)$.

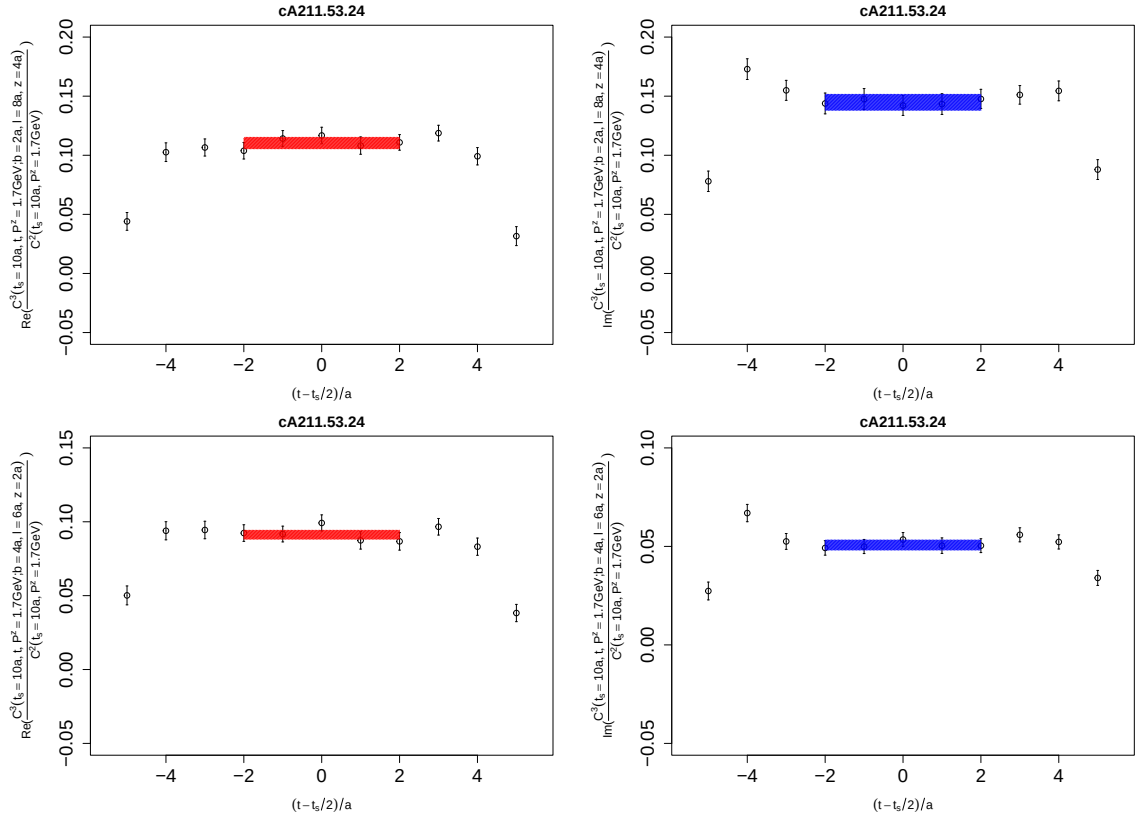

Figure 6.1: Real (left) and imaginary (right) parts of the ratio of 3-point and 2-point nucleon correlator for staple parameters $b = 2a = 0.18\,\text{fm}$, $l = 8a = 0.72\,\text{fm}$, $z = 4a = 0.36\,\text{fm}$ (top) and $b = 4a = 0.36\,\text{fm}$, $l = 6a = 0.54\,\text{fm}$, $z = 2a = 0.18\,\text{fm}$ (bottom) for $P^z = 6\pi/24a = 1.7\,\text{GeV}$ and $\Gamma = \gamma_0$ on the cA211.53.24 ensemble. The colored bands correspond to the fitted plateau.

In Figure 6.2 we show the real and imaginary parts of the ratio for a particular staple shape, for 3 different source sink separations, namely $t_s = 8a, 10a$ and $12a$, which correspond to a physical separation of $0.72\,\text{fm}, 0.93\,\text{fm}$ and $1.11\,\text{fm}$ respectively. We observe that in our chosen range of $(t - t_s/2)/a \in [-2, 2]$, the ratios for different source-sink separation are consistent with each other. For the imaginary case, there is a noticable excited state effect for $t_s = 8a$. It is possible that $8a$ is not large enough to suppress the excited state contamination. Going to larger time separations, however,

result in larger noise. Therefore, we choose $t_s = 10a$ as our source-sink separation for the rest of this work.

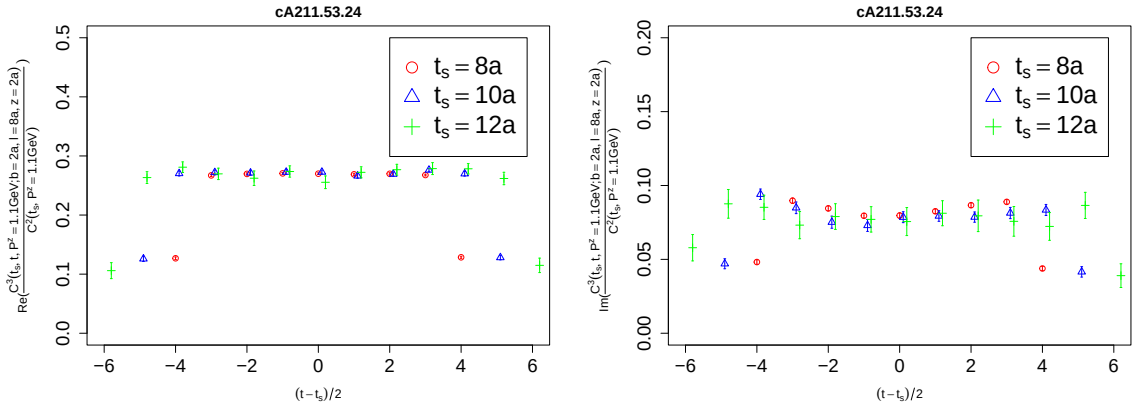

Figure 6.2: Real (left) and imaginary (right) parts of the ratio of 3-point and 2-point nucleon correlator for staple parameters $b = 2a = 0.18\,\text{fm}, l = 8a = 0.72\,\text{fm}, z = 2a = 0.18\,\text{fm}$ for source-sink separations $t_s = 8a, 10a$ and $12a$ for $P^z = 4\pi/24a = 1.1\,\text{GeV}$ and $\Gamma = \gamma_0$ on the cA211.53.24 ensemble. Note that the points for different t_s are slightly shifted horizontally for better visibility.

In Figure 6.3 we show the real and imaginary parts of the bare quasi-beam function $B_{0,\Gamma}$ for 2 different values of b and for $l = 6a, 8a$ and $10a$ for $P^z = 6\pi/24a = 1.7\,\text{GeV}$. In this work, we set $\Gamma = \gamma_0$. These results are obtained by averaging over all positive and negative directions of l, b and z using the following identities.

$$\begin{aligned} B(b,l,z,P^z) &= B^\dagger(b,l,z,-P^z), \qquad & B(b,l,z,P^z) &= B^\dagger(b,l,-z,P^z), \\ B(b,l,z,P^z) &= B^\dagger(b,-l,z,P^z), \qquad & B(b,l,z,P^z) &= B(-b,l,z,P^z). \end{aligned} \tag{6.3}$$

Following this identity, we observe the real part to be symmetric and the imaginary part to be anti-symmetric in z. As expected from theory [62], we observe the quasi-beam function to decay with l as $\sim e^{-l}$. The square root of the rectangular Wilson loop Z_E in Eq. (3.47) is expected to cancel this divergence. In the next section, we will show that such a cancellation indeed happens.

A similar behaviour of $\sim e^{-b}$ is also expected for the transverse separation. In Figure 6.4 we show the real and imaginary parts of the quasi-beam function for different values of b for fixed $l = 8a$ and observe this decay.

6.1.2 Renormalization

In Chapter 4, we discussed 3 different methods of nonperturbative renormalization of the staple-shaped operator. Here we present the results for the individual methods and compare the final renormalized quasi-beam function.

Starting with RI/MOM, the renormalization factors $Z^{\text{RI}}_{\Gamma\Gamma'}$ are calculated using Eq. (4.10). For this, we have used $N_f = 4$ (4 mass degenerate quark flavours) landau gauge fixed configurations with the same lattice parameters as the cA211.53.24 ensemble. We have used 40 such configurations for this calculation at the sea pion mass of 350 MeV. Sine we want to renormalize the staple-shaped operator for $\Gamma = \gamma_0$, following the discussion in Section 4.1, we consider the set of operators

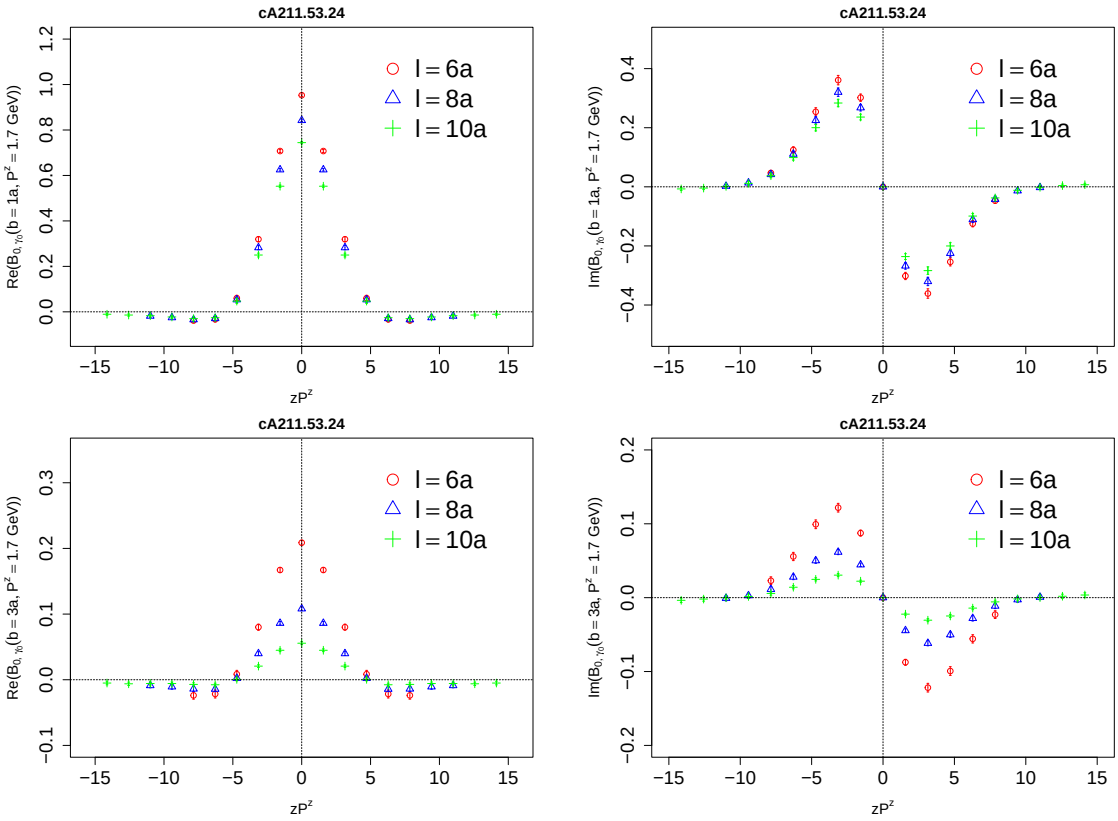

Figure 6.3: Real (left) and imaginary (right) parts of the bare quasi-beam function at $b = 1a = 0.09$ fm (top) and $b = 3a = 0.27$ fm (bottom).

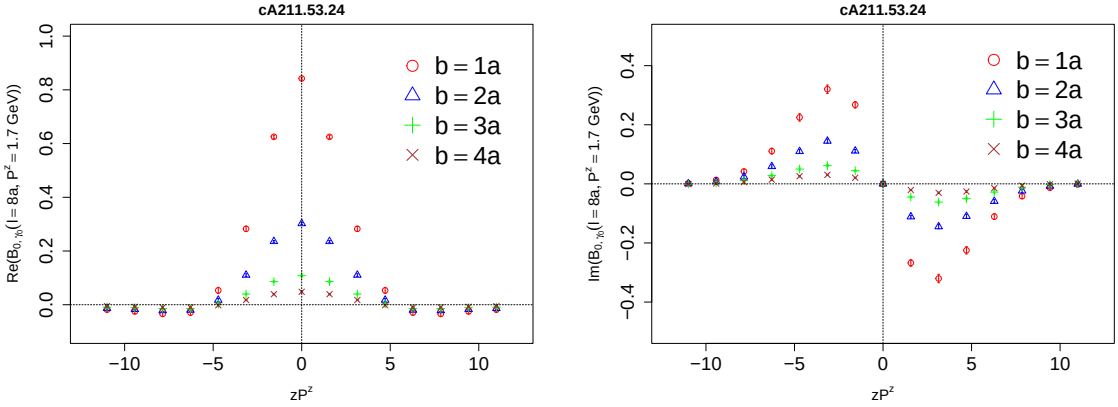

Figure 6.4: Real (left) and imaginary (right) parts of the bare quasi-beam function at $l = 8a = 0.72$ fm.

$\{\gamma_0, \gamma_0\gamma_2, \gamma_0\gamma_3, \gamma_5\gamma_1\}$. We set the renormalization scale μ_0 to $2\pi\left(\frac{6+0.5}{T}, \frac{3}{L}, \frac{3}{L}, \frac{3}{L}\right)$, where $T = 48$ and $L = 24$ are the temporal and spatial extents of the lattice respectively. Antiperiodic boundary conditions are used in the temporal direction. We have chosen an isotropic momentum in the spatial

directions and a "democratic" momentum which satisfies the condition

$$\sum_{\rho} \frac{\sin^4(ap_\rho/2)}{\left(\sin^2(ap_\rho/2)\right)^2}\Bigg|_{p=\mu_0} < 0.3, \tag{6.4}$$

in order to reduce Lorentz-noninvariant contributions in the vertex function.

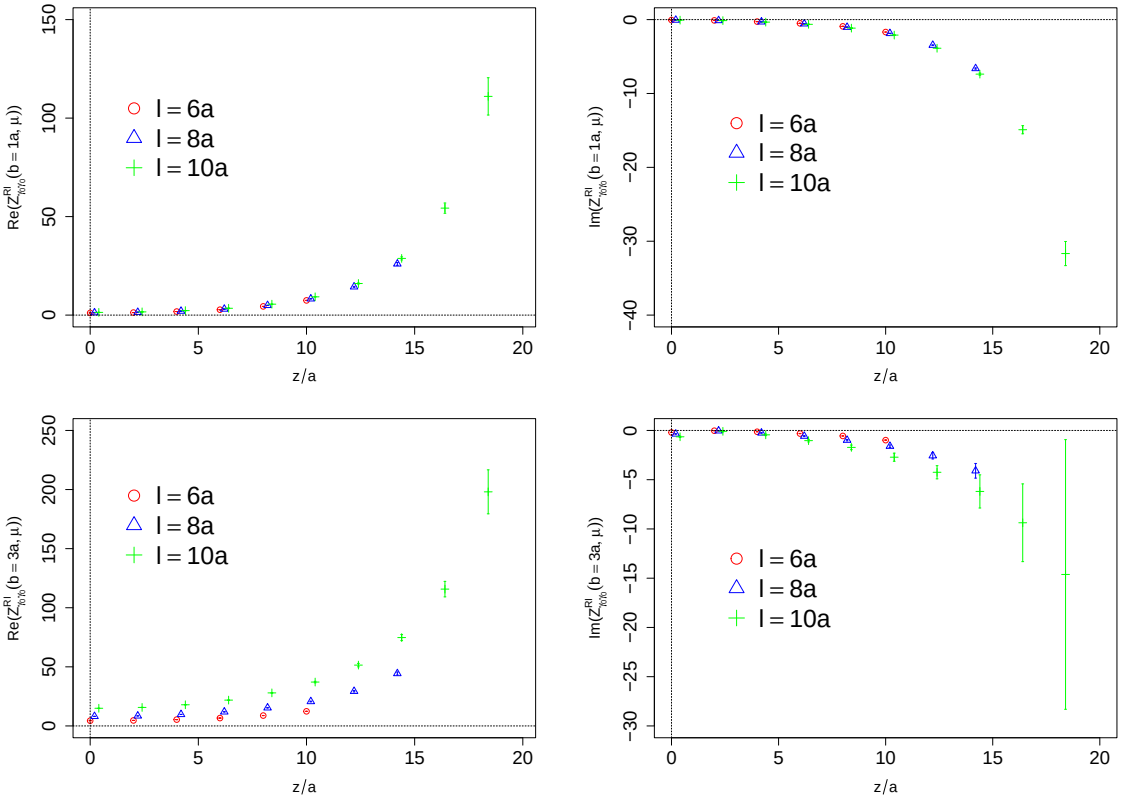

Figure 6.5: Real (left) and imaginary (right) parts of the diagonal RI/MOM renormalization factors for $b = 1a$ (top) and $b = 3a$ bottom.

In Figure 6.5 we show the renormalization factors for the diagonal part. In Figure 6.6 we show the contribution of the off-diagonal factors in the RI matrix normalized with respect to the diagonal factor at every staple shape. It is also interesting to see the renormalization factors at large transverse separations, since we are interested in the long distance nonperturbative regime. In Figure 6.7 we show the values of the RI/MOM factors with increasing values of b at a fixed length of l and z. The contribution of the off-diagonal elements which contribute to overall mixing seems quite negligible. Even at large distances the off-diagonal factors are $< 7\%$ of the corresponding diagonal one. Although the contribution for $\gamma_5\gamma_1$ is significantly larger compared to $\gamma_0\gamma_2$ and $\gamma_0\gamma_3$ and seems to be increasing with b, it is still well within 10%. We notice that the authors of Ref. [66] considered the entire set of Dirac structures for the operator mixing, and observe similar results to ours, if we take from Ref. [66] only the results from the operators that are allowed to mix with γ_0, according to our symmetry

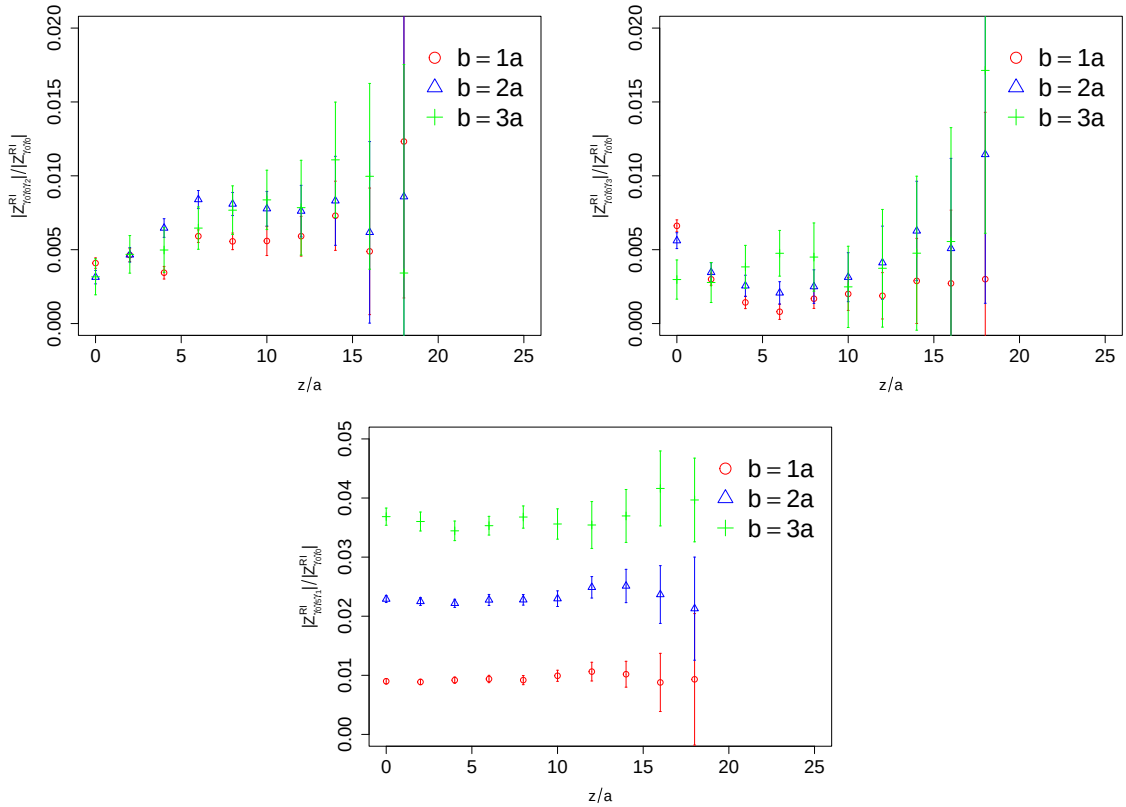

Figure 6.6: Contribution of the off-diagonal renormalization factors ($\gamma_0\gamma_2$ (top left), $\gamma_0\gamma_3$ (top right) and $\gamma_5\gamma_1$ (bottom)) compared to the diagonal one at $l = 10a$.

arguments. For example, their result for the contribution from $\gamma_5\gamma_1$ is much larger than that of $\gamma_0\gamma_2$ and $\gamma_0\gamma_3$, and there is a steady increase going to larger b values. For the values of b we use in this work, the magnitude of mixing for these operators found in Ref. [66] is also comparable to our findings.

Considering the diagonal contribution, however, we observe that the RI/MOM factors explode at large distances for both b and z. This makes the renormalization signficantly difficult at these larger shapes of the staple, since the quasi-beam function also decays exponentially with b. This exponential increase of the RI/MOM factors observed here could also be due to some residual divergences. This behaviour of the RI/MOM factors is also observed in Ref. [73].

In Figure 6.8 we show the RI/MOM renormalized quasi-beam function for $b = 1a$. We observe that there is no residual l dependence. So RI/MOM does indeed cancel the divergence associated to l, which is expected since the vertex function and the quasi-beam function contain the exact same shape of the staple. The error, however, increases significantly with z. This is due to the exponential increase of the RI/MOM factors with z as shown in Figure 6.5. In Figure 6.9 we observe the effect of mixing. The red points correspond to the full RI/MOM procedure where we consider the set of 4 operators that are allowed to mix. The blue points correspond to the case where we only consider the diagonal element in the renormalization matrix and set the off-diagonal elements to zero. We observe that these points are identical within errors. With this result, we can conclude that the mixing is negligible for the staple-shaped operator.

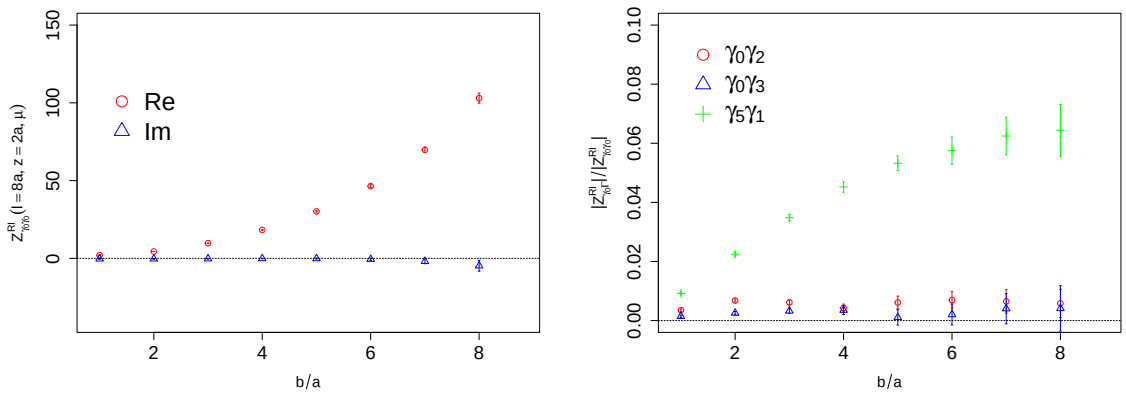

Figure 6.7: Diagonal (left) and off-diagonal (right) RI/MOM factors for increasing transverse separation b for a fixed $l = 8a$ and $z = 2a$.

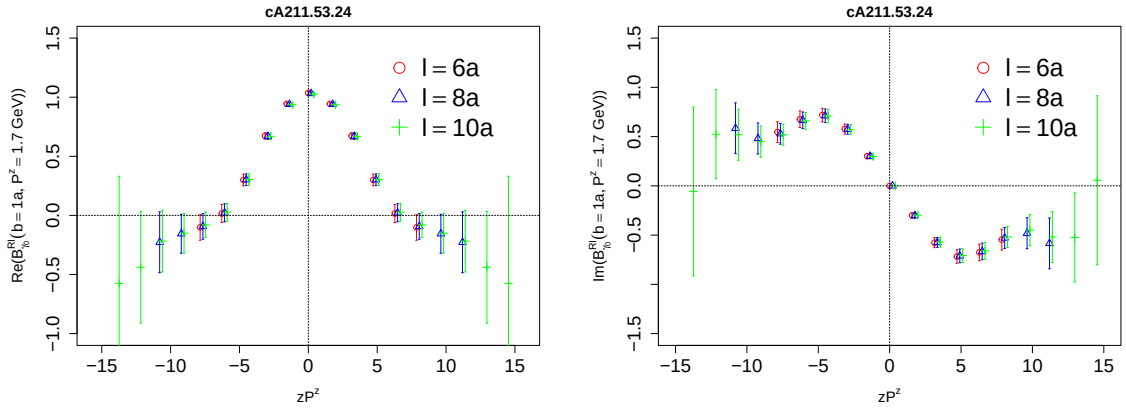

Figure 6.8: Real (left) and imaginary (right) parts of the RI/MOM renormalized quasi-beam function at $b = 1a$ for different lengths of l.

Since mixing is negligible, we can consider the other two renormalization methods discussed in Chapter 4. Firstly, we use the rectangular Wilson-loop to cancel the pinch-pole singularitiy associated with the length l of the staple, as well as the divergences associated with the cusps. To illustrate this point, in Figure 6.10 we show the unsubtracted quasi-beam function and the quasi-beam function after taking a ratio with $\sqrt{Z_E}$ for different values of l. We observe that after taking the ratio, the quasi-beam function reaches a plateau at $l \geq 6a$. This is a clear indication that the rectangular Wilson loop completely cancels the divergence associated with l.

The remaining UV divergences can be cancelled by using an appropriate multiplicative renormalization factor. The two methods we consider are SDR (see Sec. 4.3) and RI-short (see Sec. 4.4). The corresponding renormalization factors are

$$Z_{\text{SDR}} = \frac{1}{B_\Gamma(z = z_0, b = b_0, P^z = 0)} \tag{6.5}$$

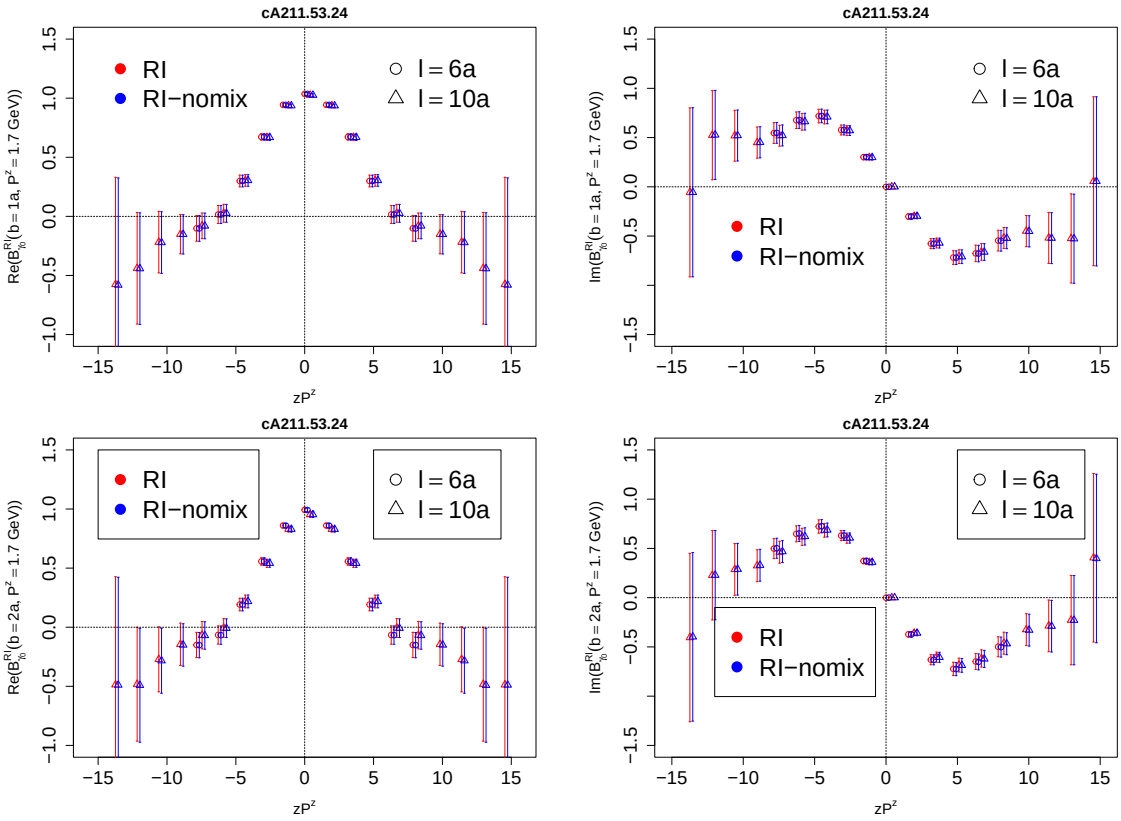

Figure 6.9: Real (left) and imaginary (right) parts of RI/MOM renormalized quasi-beam function at $b = 1a$ (top) and $b = 2a$ (bottom) for different lengths of l. The red points correspond to the full RI/MOM procedure where we consider the set of 4 operators that are allowed to mix. The blue points correspond to the case where we only consider the diagonal element in the renormalization matrix and set the off-diagonal elements to zero.

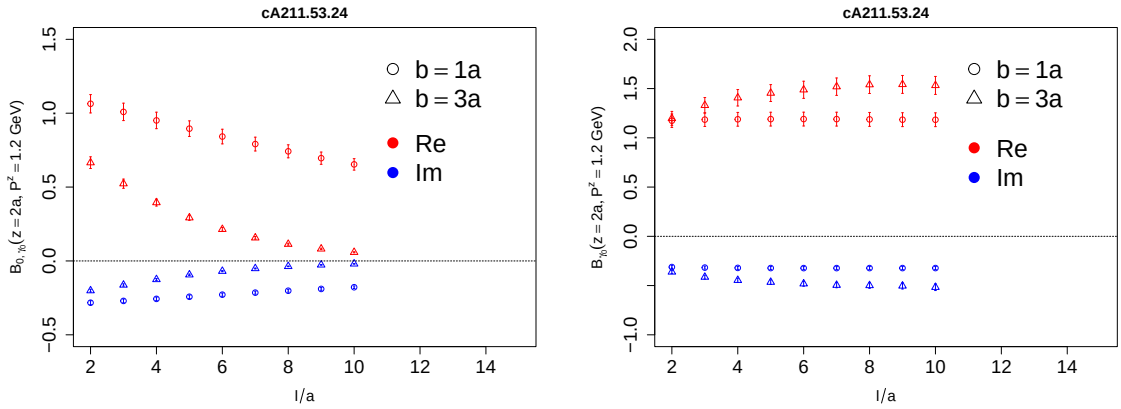

Figure 6.10: The unsubtracted quasi-beam function (left) and the effect of taking the ratio with the square root of the rectangular Wilson loop (right) for $l \in [2a, 10a]$.

and

$$Z_{\text{RI-short}} = Z^{RI}_{\gamma_0\gamma_0}(z_0, b_0, l, \mu_0) \times \sqrt{Z_E(2l, b_0)}. \tag{6.6}$$

Note that the B_Γ in Z_{SDR} already contains the $\sqrt{Z_E}$ factor, whereas in $Z_{\text{RI-short}}$, since the vertex function used in the RI/MOM procedure also includes the staple-shaped operator and the associated divergences, one needs to multiply the rectangular loop $\sqrt{Z_E}$ separately. The choice of b_0 and z_0 must be such that we are in a perturbative regime in order to make the conversion to $\overline{\text{MS}}$ scheme reliable. Assuming that we are at a short enough distance, the final result in the $\overline{\text{MS}}$ scheme should be independent of the values of b_0 and z_0. In Figure 6.11, we compare the renormalization factor in the $\overline{\text{MS}}$ scheme using the SDR and RI-short methods for different combinations of $b_0 \in \{1a, 2a\}$ and $z_0 \in \{0, 2a\}$. We observe that the real part of the factors from the two different schemes are comparable but not identical. This difference could be due to considerable $O(\alpha_s^2)$ corrections. We also note that the factors at $z_0 = 0$ and $z_0 = 2a$ are consistent at $b_0 = 1a$ but the difference increases at $b_0 = 2a$. This indicates a limitation in the perturbative conversion to $\overline{\text{MS}}$ at a transverse separation as low as $b = 2a$. We also observe that the imaginary part is zero for SDR and non-zero for RI-short. This is by construction, since the SDR factor is computed at zero momentum whereas the RI-short is obtained from vertex functions at non-zero momentum. At $z_0 = 0$, the imaginary part for the RI-short factors are closest to zero and increase significantly at $z_0 = 2a$. Taking these observations into account, we choose $b_0 = 1a$ and $z_0 = 0$ for both SDR and RI-short renormalization schemes.

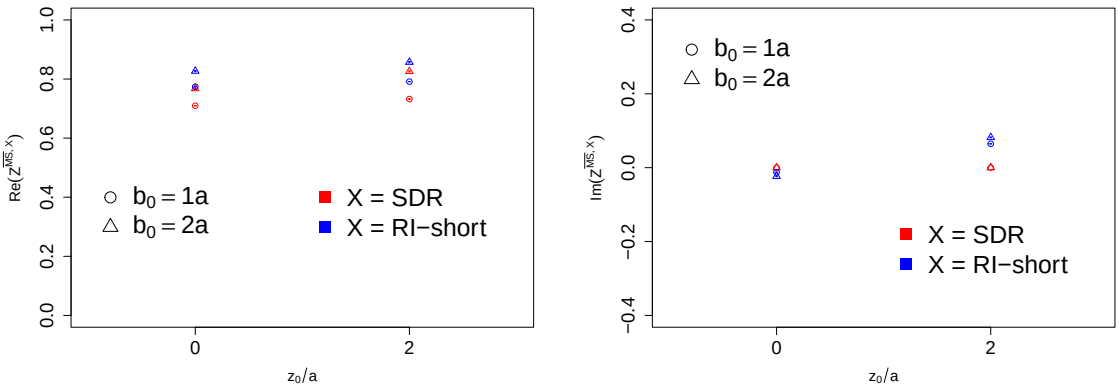

Figure 6.11: Real (left) and imaginary (right) parts of the renormalization factors in the $\overline{\text{MS}}$ scheme using the SDR and RI-short methods for different combinations of $b_0 \in \{1a, 2a\}$ and $z_0 \in \{0, 2a\}$.

In Figure 6.12, we compare the renormalized quasi-beam function using the 3 different methods. Considering the real part, we observe that at short distances, the results are comparable. But as z increases, the RI/MOM deviates from the other two methods. This could be due to the residual divergences present in the RI/MOM procedure [73]. The SDR and RI-short methods, on the other hand, are much more consistent and agree remarcably well for $zP^z \geq 5$. For the imaginary part, we observe a similar behaviour, only the deviation of RI/MOM from the other two methods is even more pronounced. We also note that the errors at large z are significantly more under control for the SDR and RI-short methods compared to the RI/MOM method. These results suggest that both the SDR and RI-short methods are more reliable for the nonperturbative renormalization of the staple-shaped operator.

Finally, we perform a conversion to $\overline{\text{MS}}$ using Eq. (4.19) and in Figure 6.13 we show the renormalized quasi-beam function in the $\overline{\text{MS}}$ scheme using both the SDR and the RI-short method. For more details on the computation of the conversion factors for the perturbative matching to $\overline{\text{MS}}$, see [131]. We

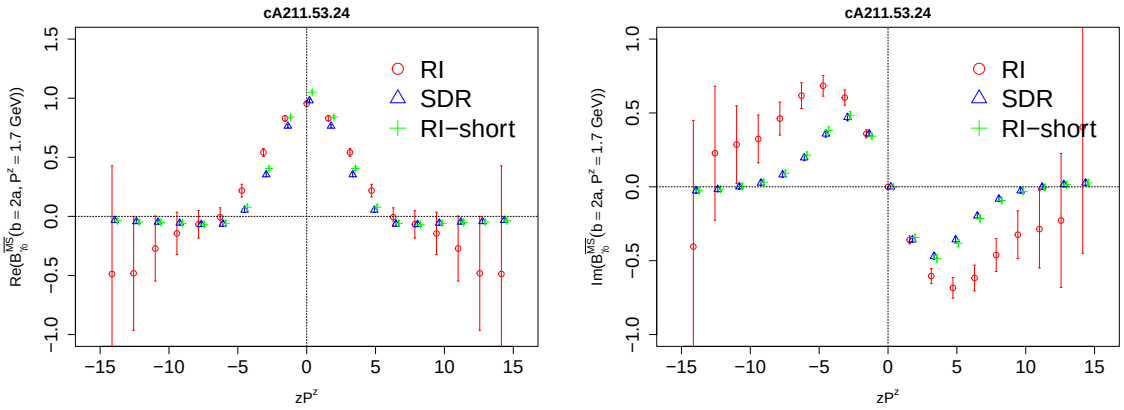

Figure 6.12: Real (left) and imaginary (right) parts of the nonperturbatively renormalized quasi-beam function using the three diffferent renormalization scheme at $b = 2a$ and $l = 10a$. Note that the results for different procedures are slightly shifted horizontally for better visibility.

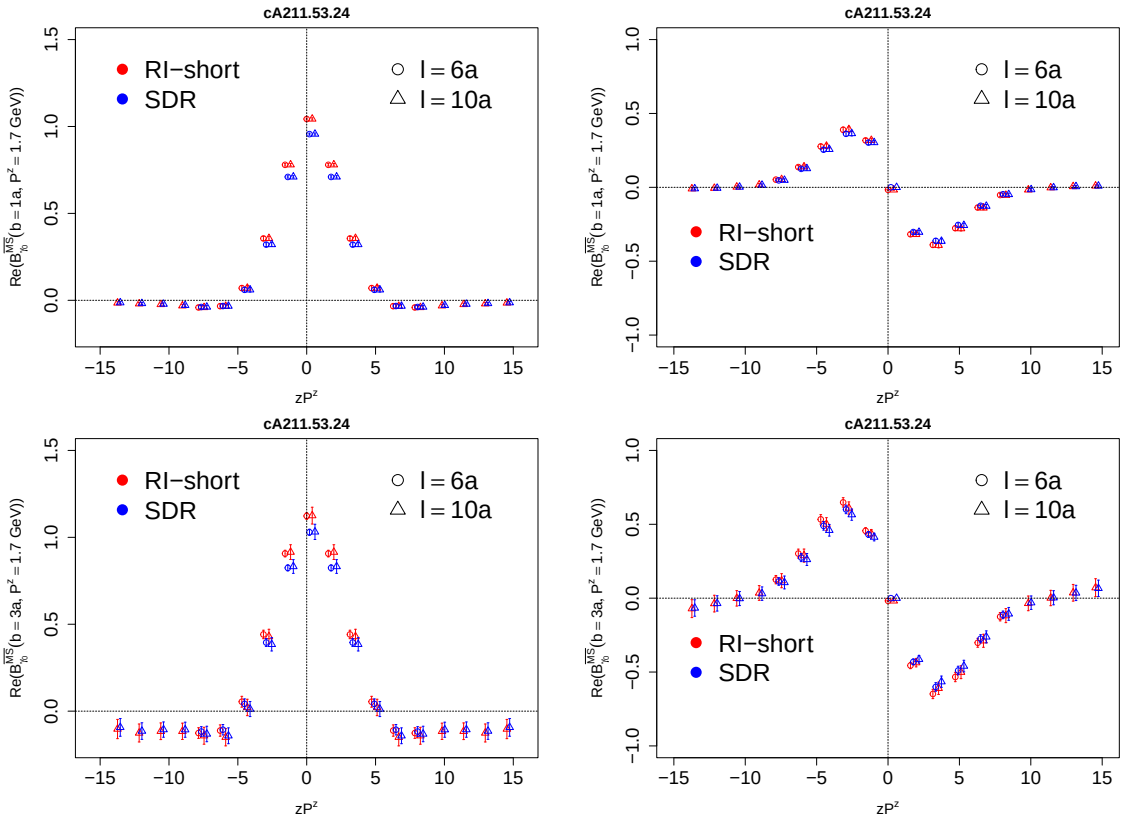

Figure 6.13: Real (left) and imaginary (right) parts of the quasi-beam function in the $\overline{\text{MS}}$ scheme using the SDR and RI-short method at $b = 1a$ (top) and $b = 3a$ (bottom).

observe a similar behaviour as before. The real part has some tension between the two methods at small values of z. At large distances, however, they agree very well. The imaginary part is consistent

between the two methods for all values of z.

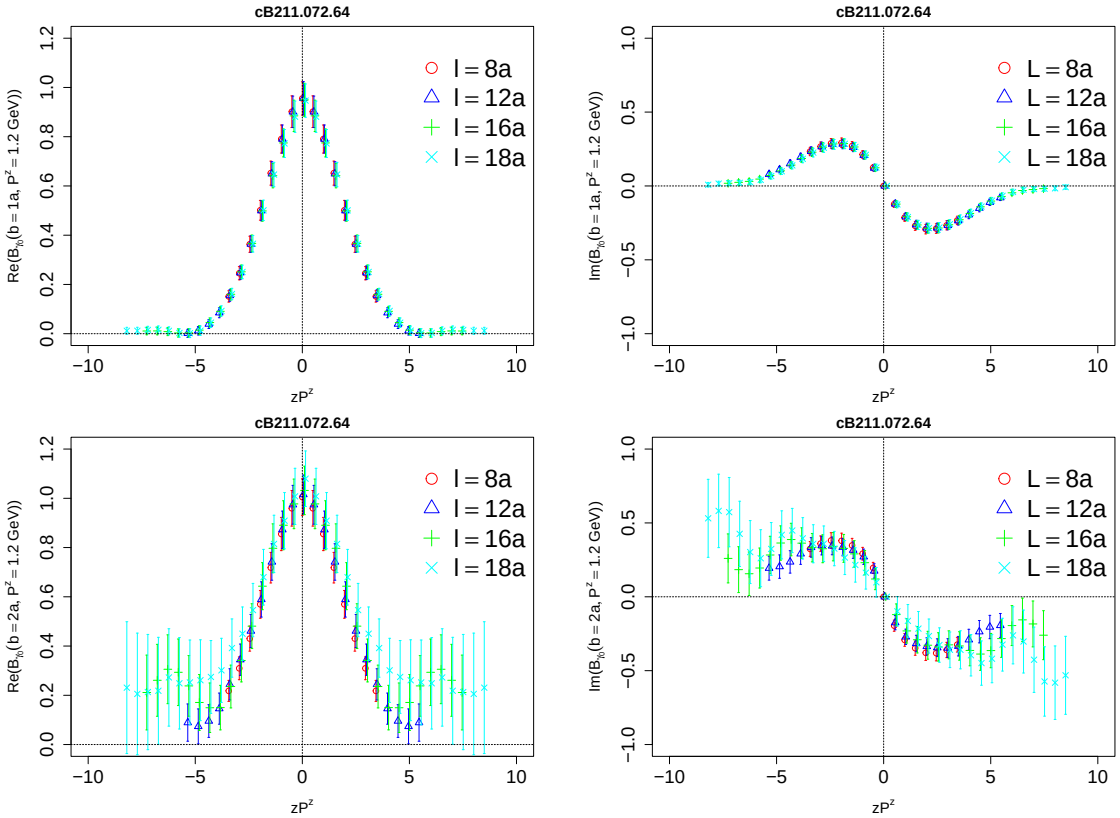

Figure 6.14: Real (left) and imaginary (right) parts of the quasi-beam function for the cB211.072.64 ensemble at $P^z = 10\pi/64a \sim 1.2\,\text{GeV}$ renormalized using the SDR scheme at $b = 1a$ (top) and $b = 2a$ (bottom). Results at different l are shifted horizontally for better visibility.

At this point we can also show the current status of the TMDPDF calculation on the physical ensemble cB211.072.64. In Figure 6.14 we show the SDR renormalized quasi-beam function at $b = 1a$ and $b = 2a$ for the physical ensemble at $P^z \sim 1.2\,\text{GeV}$. We observe again that the l dependence is completely cancelled by the rectangular Wilson loop. The results are significantly more noisy compared to the cA211.53.24 ensemble, which is expected. Since building longer staples is more expensive computationally and is also more noisy, we can set $l = 8a$ in future calculation and probe further in the transverse separation b.

Since the SDR and RI-short methods are consistent with each other, in the rest of this work, we use the SDR method for renormalization of the staple-shaped operator.

6.1.3 Renormalized quasi-TMDPDF

The quasi-TMDPDF is defined in the momentum space by performing a Fourier transform of the quasi-beam function.

$$\tilde{f}\left(x, b, \mu, \zeta_z\right) = \int_{-\infty}^{+\infty} \frac{P^z dz}{2\pi} e^{ixzP^z} B\left(z, b, \mu, P^z\right). \tag{6.7}$$

We perform a discrete Fourier transform on the quasi-beam function to obtain the quasi-TMDPDF. On the lattice, this results in a sum

$$\tilde{f}\left(x, b, \mu, \zeta_z\right) = \frac{P^z}{2\pi} \sum_{z=-z_{\max}}^{+z_{\max}} e^{ixzP^z} B\left(z, b, \mu, P^z\right), \tag{6.8}$$

which introduces a cutoff in z. Since the construction of the staple-shape also imposes a cutoff in z, namely $z_{\max} = (l-1)2/a$, for any given staple length l, we study the effect of this cutoff using that. In Figure 6.15 we show the quasi-TMDPDF for different values of l where $z_{\max}$ is set accordingly. We observe that at small value of b, the quasi-TMDPDF is consistent for all different values of l and correspondingly $z_{\max}$. At $b = 3a$ however, we observe small deviations especially at very small and large values of x. In particular we observe more oscillations for larger l and larger cutoff in z. This is expected since the data is more noisy at larger shapes of the staple-shaped operator. The results are still quite consistent with each other. One way to take into account the effect of the cutoff would be to follow [147] and extract the deviation into systematic errors. In this exploratory work, we fix $l = 8a$ and use the result for $z_{\max} = 14a$ for the rest of the calculations.

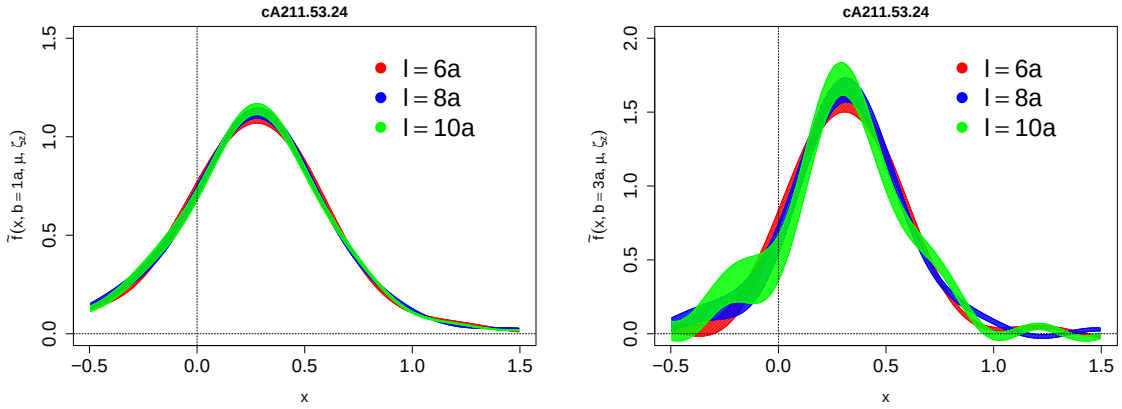

Figure 6.15: quasi-TMDPDF in the momentum space for different values of l for $b = 1a$ (left) and $b = 3a$ (right).

In Figure 6.16 we show the quasi-TMDPDF for b upto $4a \sim 0.36\,\text{fm}$. The quasi-TMDPDF is calculated at $P^z = 1.7\,\text{GeV}$ for both the lattice ensembles. All the functions at different b go smoothly to zero at large and small x. We observe that the peak increases with increasing b and also shifts slightly to larger x. This increment could partly be cancelled by the soft function and the Collins-Soper kernel and we expect to find a more consistent TMDPDF at larger transverse separations after we perform the matching.

6.2 Collins-Soper kernel

$$f^{TMD}(x, b, \mu, \zeta) = H_f\left(\frac{\zeta_z}{\mu^2}\right) e^{-\ln\left(\frac{\zeta_z}{\zeta}\right)K(b,\mu)} S_r^{\frac{1}{2}}(b, \mu)\, \tilde{f}(x, b, \mu, \zeta_z) + O\left(\frac{\Lambda_{QCD}}{\zeta_z}, \frac{M^2}{(P^z)^2}, \frac{1}{b^2\zeta_z}\right) \tag{6.9}$$

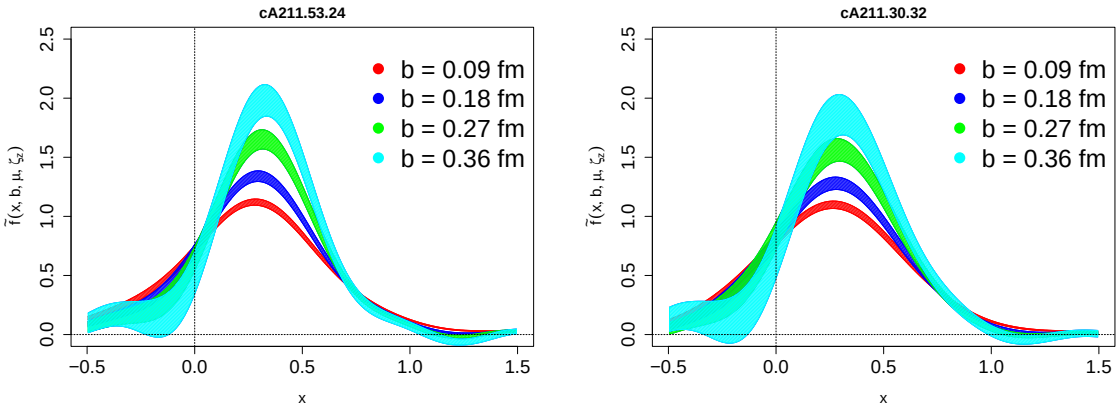

Figure 6.16: quasi-TMDPDF in the momentum space for different values of b for $l = 8a$ for cA211.53.24 (left) and cA211.30.32 (right).

We obtain the Coliins-Soper kernel by taking a ratio of the quasi-TMDWF at different rapidity (momentum boost) as defined in Eq. (3.58).

$$K(b,\mu) = \frac{1}{\frac{1}{2}\ln\left(\frac{\zeta_{z_1}}{\zeta_{z_2}}\right)} \ln\left(\frac{\tilde{\Psi}_{\bar{q}q}\left(x,b,\mu,\zeta_{z_1},\bar{\zeta}_{z1}\right)}{\tilde{\Psi}_{\bar{q}q}\left(x,b,\mu,\zeta_{z_2},\bar{\zeta}_{z2}\right)}\right) \tag{6.10}$$

where ζ_{z_1} and ζ_{z_2} are the two different rapidities. $\tilde{\Psi}$ is the quasi-TMDWF in the momentum space. As discussed in Section 5.2.2, we obtain the quasi-TMDWF from a two-point function between a pion and the staple-shaped operator. By taking a ratio of the two-point function with the ultra-local case, we extract the quasi-TMDWF as follows

$$\frac{C_\pi^{2pt}(b,l,z,t,P^z)}{C_\pi^{2pt}(0,0,0,t,P^z)} \approx \tilde{\psi}_{0,\Gamma}(b,l,z,P^z)[1 + c_0(b,l,z,P^z)e^{-\Delta E_\pi t}]. \tag{6.11}$$

In Figure 6.17 we show the aforementioned ratio at two different shapes of the staple. As we expect, a plateau is observed at large enough time separation. We obtain the quasi-TMDWF by fitting the ratio to a constant. The fitting range is set dynamically for different operators, depending on how quickly the plateu is reached.

Since the quasi-TMDWF has exactly the same operator as the quasi-beam function, the same arguments for renormalization (as discussed in previous section) apply. Therefore we use the rectangular Wilson loop to cancel the divergence associated with the length of the staple and the SDR method for the renormalization. In Figure 6.18 we show the renormalized quasi-TMDWF at two different momenta $8\pi/24a \sim 2.2\,\text{GeV}$ and $12\pi/24a \sim 3.4\,\text{GeV}$. We observe that in this case both the real and imaginary parts are symmetric with z. The imaginary part increases with increasing transverse separation. These observations are consistent with previous studies [65, 69, 70].

In a similar manner to the quasi-TMDPDF, we perform a discrete Fourier transform to obtain the quasi-TMDWF in the momentum space. In Figure 6.19 we show the quasi-TMDWF in the momentum space for $P^z = 8\pi/24a$. We observe a symmetric real part around $x = 0.5$. Since the imaginary part

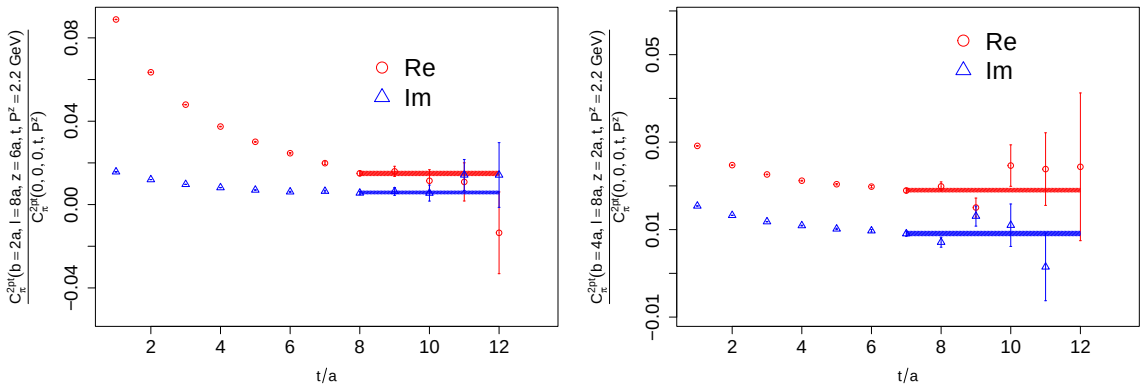

Figure 6.17: Extraction of the bare unsubtracted quasi-TMDWF for two different staple shapes. The bands indicate the fitted plateau and the range of the fit.

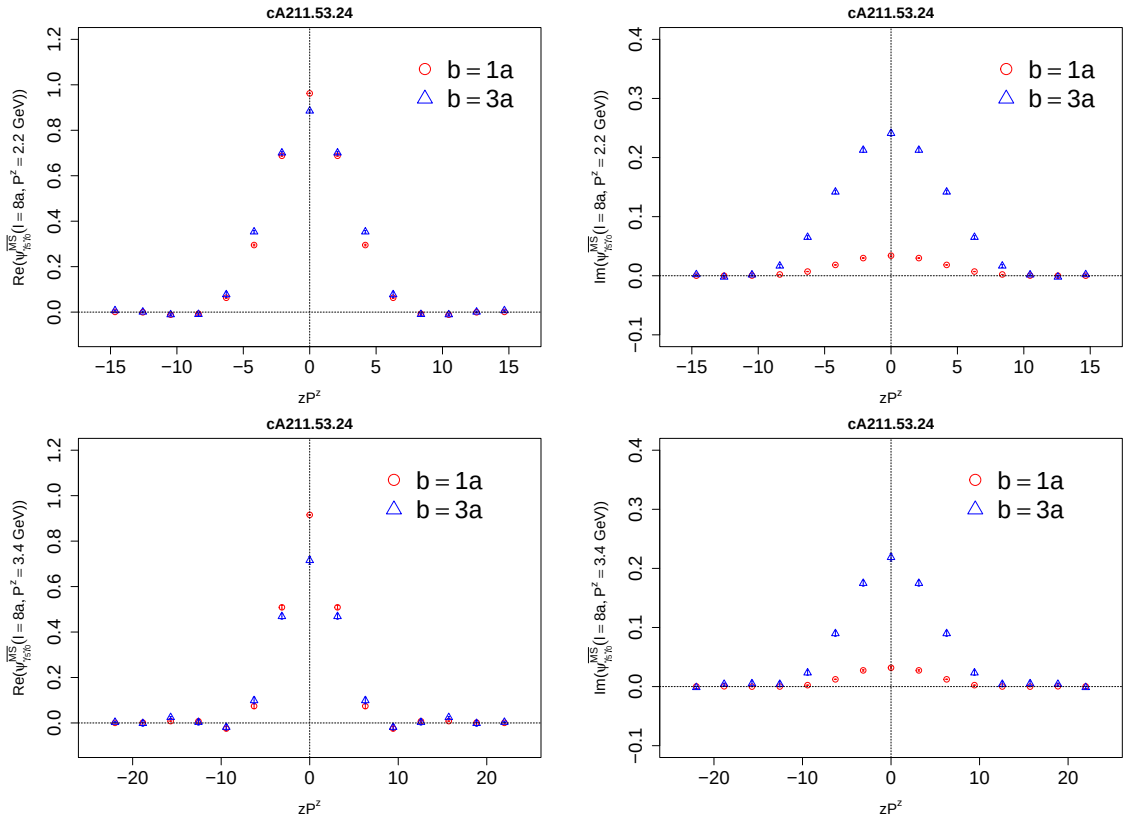

Figure 6.18: Real (left) and imaginary (right) parts of the quasi-TMDWF in the $\overline{\text{MS}}$ scheme using the SDR renormalization method at $P^z = 8\pi/24a \sim 2.2\,\text{GeV}$ (top) and $P^z = 12\pi/24a \sim 3.4\,\text{GeV}$ (bottom).

is symmetric, we see similar behaviour in the momentum space as well.

For Collins-Soper kernel, we take the ratio of the quasi-TMDWF at two different rapidities. In Figure 6.20 we show the ratio of the quasi-TMDWF at $P^z = 12\pi/24a$ and $8\pi/24a$. We expect this

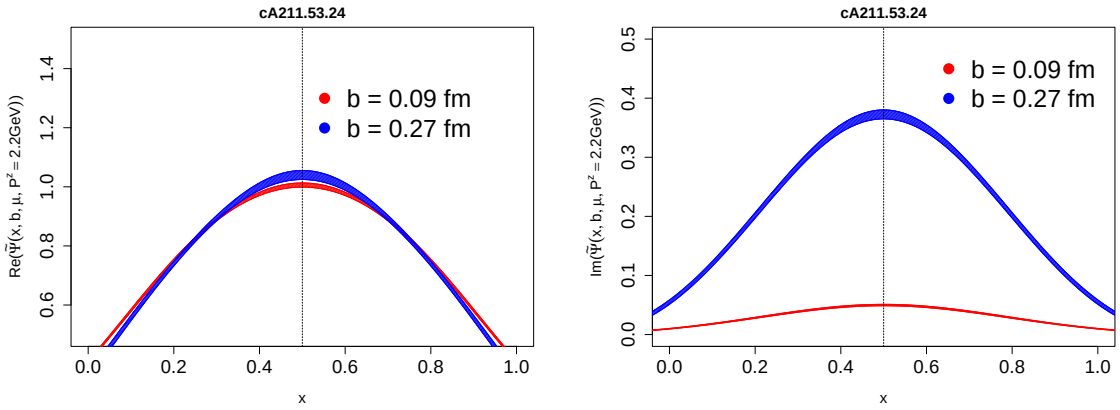

Figure 6.19: Real (left) and imaginary (right) parts of the quasi-TMDWF in the momentum space for $P^z = 8\pi/24a \sim 2.2\,\text{GeV}$ at $b = 1a$ (red) and $b = 3a$ (blue).

ratio to be independent of x and we observe a fairly constant behaviour for a large range of x. We fit a constant in the range $x \in [0.1, 0.9]$ to extract the value of this ratio. In principle, this ratio should be purely real. However, since the imaginary part of the quasi-TMDWF increases with b, we also observe a small imaginary part of the ratio at large b. Although it is much smaller than real part, it is still definitely non-zero. The authors of [69] also observed this and they included the imaginary part into their systematic uncertainties. In this work, we do not consider the imaginary part.

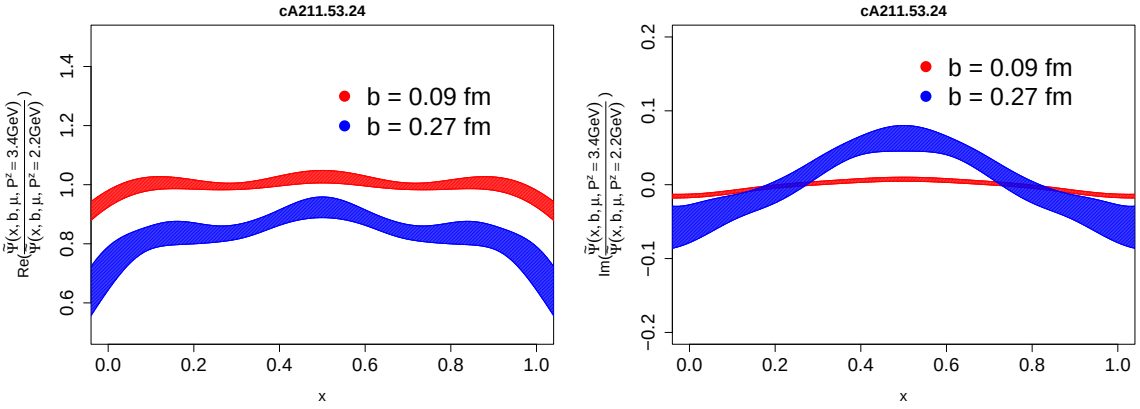

Figure 6.20: Real (left) and imaginary (right) parts of the ratio of quasi-TMDWFs in the momentum space.

Finally, we obtain the Collins-Soper kernel and also perform perturbative corrections upto 2-loop order using [148]

$$
\begin{aligned}
K(b,\mu) =& \frac{1}{\frac{1}{2}\ln\left(\frac{\zeta_{z_1}}{\zeta_{z_2}}\right)} \ln\left(\frac{\tilde{\Psi}_{\bar{q}q}\left(x,b,\mu,\zeta_{z_1},\bar{\zeta}_{z1}\right)}{\tilde{\Psi}_{\bar{q}q}\left(x,b,\mu,\zeta_{z_2},\bar{\zeta}_{z2}\right)}\right) - \frac{\alpha_s}{4\pi}C_F\left[4 - \ln\left(\frac{\zeta_{z_1}\zeta_{z_2}\bar{\zeta}_{z_1}\bar{\zeta}_{z_2}}{\mu^8}\right) \mp 4i\pi\right] \\
&- \frac{\alpha_s^2}{(4\pi)^2}C_F\left\{N_c\left(\frac{362}{27} + \frac{23\pi^2}{9} - 30\zeta_3\right) + C_F\left(4 - \frac{14\pi^2}{3} + 24\zeta_3\right) + N_f\left(-\frac{41}{27} - \frac{2\pi^2}{9}\right)\right. \\
&+ \left[N_c\left(-\frac{100}{9} + \frac{\pi^2}{3}\right) + N_f\frac{16}{9}\right]\frac{1}{2}\left(\ln\left(\frac{\zeta_{z_1}\zeta_{z_2}\bar{\zeta}_{z_1}\bar{\zeta}_{z_2}}{\mu^8}\right) \pm 4i\pi\right) \\
&+ \left[-N_c\frac{11}{9} + N_f\frac{2}{9}\right]\frac{1}{2}\left[\frac{1}{2}\ln\left(\frac{\zeta_{z_1}\zeta_{z_2}\bar{\zeta}_{z_1}\bar{\zeta}_{z_2}}{\mu^8}\right) + \ln\left(\frac{\left(P_1^z\right)^2}{\left(P_2^z\right)^2}\right) \pm 3i\pi\ln\left(\frac{\zeta_{z_1}\zeta_{z_2}\bar{\zeta}_{z_1}\bar{\zeta}_{z_2}}{\mu^8}\right)\right. \\
&\left.\left. - \ln\left(\frac{\zeta_{z_1}}{\mu^2}\right)\ln\left(\frac{\zeta_{z_2}}{\mu^2}\right) - \ln\left(\frac{\bar{\zeta}_{z_1}}{\mu^2}\right)\ln\left(\frac{\bar{\zeta}_{z_2}}{\mu^2}\right)\right]\right\} + O\left(\alpha_s^3\right).
\end{aligned}
\tag{6.12}
$$

In Figure 6.21 we show the Collins-Soper kernel calculated in this work and compare it to previous lattice studies. We observe that our results are consistent with the other studies. Our results at 2 different ensembles are also consistent with each other and completely agree at large enough b. A publication with these results is currently in preparation [148].

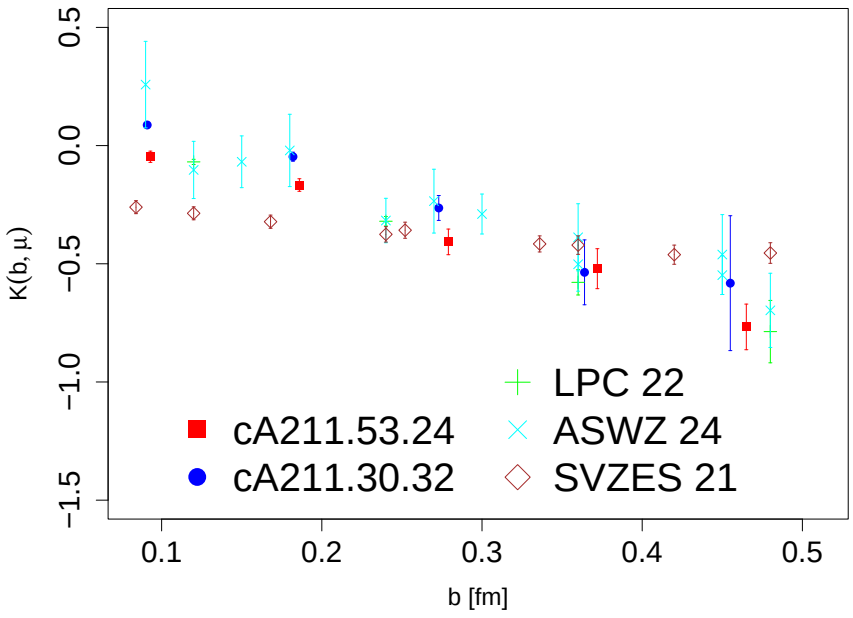

Figure 6.21: Our results for the Collins-Soper kernel compared with previous lattice calculations presented in LPC 22 [69], ASWZ 24 [71] and SVZES 21 [67].

6.3 Soft function

$$f^{TMD}(x,b,\mu,\zeta) = H_f\left(\frac{\zeta_z}{\mu^2}\right) e^{-\ln\left(\frac{\zeta_z}{\zeta}\right)K(b,\mu)} S_r^{\frac{1}{2}}(b,\mu)\, \tilde{f}(x,b,\mu,\zeta_z) + O\left(\frac{\Lambda_{QCD}}{\zeta_z}, \frac{M^2}{(P^z)^2}, \frac{1}{b^2\zeta_z}\right) \tag{6.13}$$

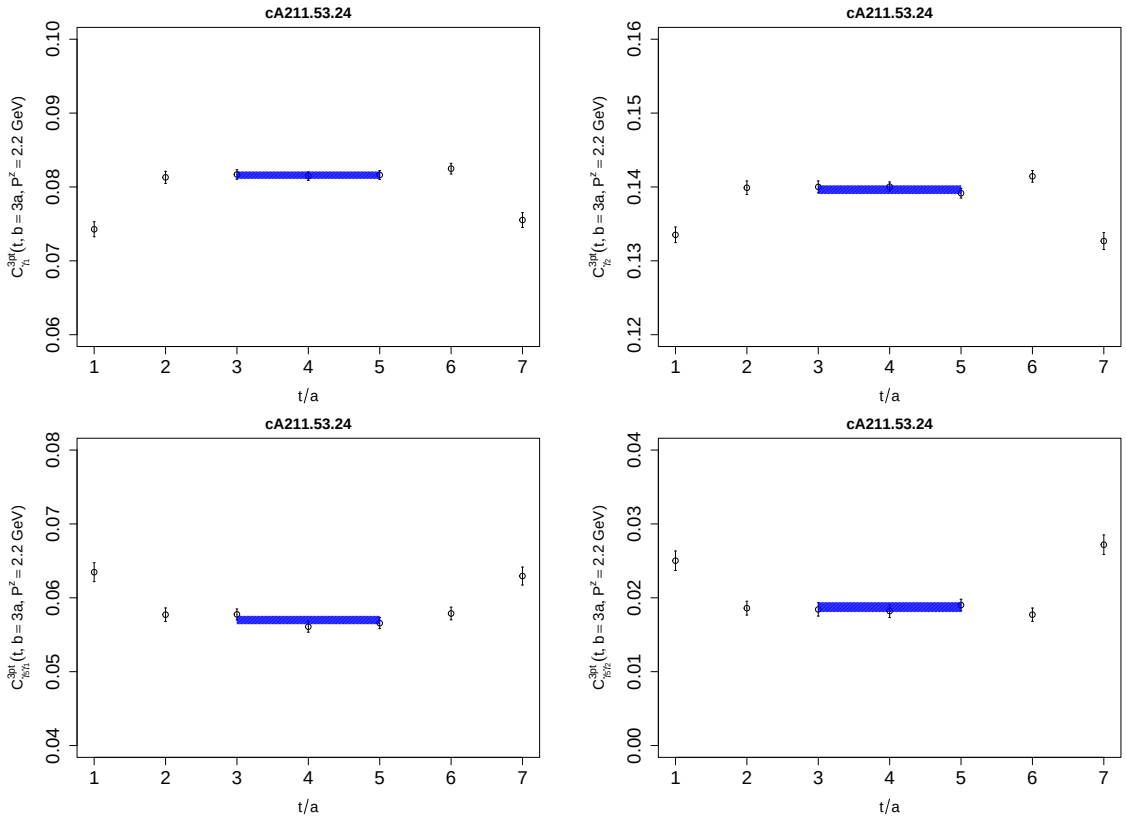

Figure 6.22: Pion 3-point correlators for γ_1 (top left), γ_2 (top right), $\gamma_5\gamma_1$ (bottom left) and $\gamma_5\gamma_2$ (bottom right) at $b = 3a$ and $P^z = 2.2\,\text{GeV}$. The shaded region indicates the fitted plateau from which the form factor is extracted.

Soft function takes the form of the following ratio

$$S_r(b,\mu) = \frac{\left\langle \pi\left(P'\right) \left| \bar{q}_2(b)\Gamma q_2(b)\bar{q}_1(0)\Gamma q_1(0) \right| \pi(P) \right\rangle}{\int_{-\infty}^{\infty} dx \int_{-\infty}^{\infty} dx' H_{F_\Gamma}\left(x,x',P,P',\mu\right) \tilde{\Psi}^{\dagger}_{\bar{q}q}\left(x',b,\mu,P'\right) \tilde{\Psi}_{\bar{q}q}(x,b,\mu,P)} \tag{6.14}$$

where the matching hard kernel H_{F_Γ} is given by [113]

$$H_{F_\Gamma}\left(x,x',P,P',\mu\right) = 1 + \frac{\alpha_s}{4\pi}C_F\left[h_0^\Gamma + 2\pi^2 + \ln^2\left(-\frac{|x'|}{|x|}\mp i\varepsilon\right)\right.$$
$$\left. + \ln^2\left(-\frac{|1-x'|}{|1-x|}\mp i\varepsilon\right) + h_1^\Gamma \ln\left(\frac{16|x||1-x|\,|x'|\,|1-x'|\,(P^z)^4}{\mu^4}\right)\right] + O\left(\alpha_s^2\right) \tag{6.15}$$

where

$$h_0^1 = h_0^{\gamma_5} = 4, h_0^{\gamma_\perp} = h_0^{\gamma_5\gamma_\perp} = -8, h_1^1 = h_1^{\gamma_5} = -2, h_1^{\gamma_\perp} = h_1^{\gamma_5\gamma_\perp} = 1. \tag{6.16}$$

In Figure 6.22 we show the 3-point correlator from which we can extract the meson form factor in the numerator of Eq. (6.14) for different Dirac Γ insertions at $b = 3a$ and $P^z = 8\pi/24a \sim 2.2\,\text{GeV}$. For the soft function, we build the combination $\gamma_\perp + \gamma_5\gamma_\perp$, since this cancels the higher twist contributions [64]. In Figure 6.23 we show the soft function calculated in this work and compare it to previous lattice calculation by LPC [65]. We observe that our results are comparable to the LPC calculation and have a similar behaviour with b. Our results for 2 different ensembles are also consistent with each other. A publication with these results is currently in preparation [148].

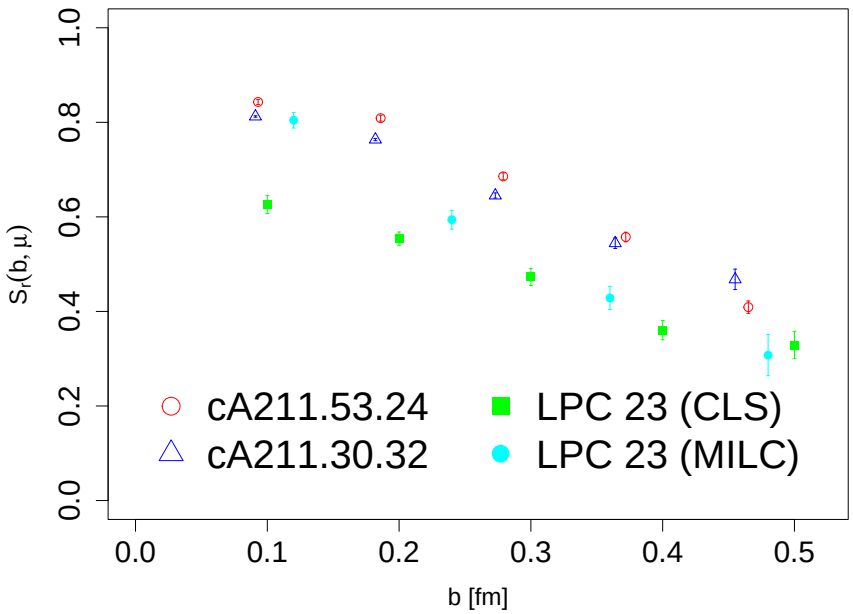

Figure 6.23: Our results for the reduced soft function compared with previous lattice calculation in [65].

6.4 Matching to physical TMDPDF

$$f^{TMD}(x,b,\mu,\zeta) = H_f(\frac{\zeta_z}{\mu^2})\, e^{-\ln\left(\frac{\zeta_z}{\zeta}\right)K(b,\mu)}\, S_r^{\frac{1}{2}}(b,\mu)\, \tilde{f}(x,b,\mu,\zeta_z) + O\left(\frac{\Lambda_{QCD}}{\zeta_z}, \frac{M^2}{(P^z)^2}, \frac{1}{b^2\zeta_z}\right) \tag{6.17}$$

Now that we have calculated all the ingredients on the right hand side, we can perform the matching to obtain the light-cone TMDPDF. The perturbative matching kernel H_f is given by [62]

$$H_f\left(\frac{\zeta_z}{\mu^2}\right) = 1 - \frac{\alpha_s}{4\pi}C_F\left[-4 + \frac{\pi^2}{6} + 2\ln\left(\frac{\zeta_z}{\mu^2}\right) - \ln^2\left(\frac{\zeta_z}{\mu^2}\right)\right] + O\left(\alpha_s^2\right) \tag{6.18}$$

where $C_F = 4/3$. However, since the Collins-Soper kernel and the reduced soft function also contain perturbative corrections, in order to perform a matching consistent upto $O(\alpha_s)$, we need to include all the necessary corrections. The final expression for the physical TMDPDF perturbatively matched up to 1-loop order is [148]

$$\begin{aligned}
f^{TMD}(x,b,\mu,\zeta) &= \tilde{f}(x,b,\mu,\zeta_z)\exp\left(-\ln\left(\zeta_z/\zeta\right)K_{LO}(b,\mu)\right) S_{r,LO}^{\frac{1}{2}} \\
&\times\left\{1 - \frac{\alpha_s}{4\pi}C_F\left[-4 + \frac{\pi^2}{6} + 2\ln\left(\frac{\zeta_z}{\mu^2}\right) - \ln^2\left(\frac{\zeta_z}{\mu^2}\right) - \ln\left(\frac{\zeta_z}{\zeta}\right)\left(4 - \ln\left(\frac{\zeta_{z1}\bar{\zeta}_{z1}\zeta_{zz}\bar{\zeta}_{z2}}{\mu^4}\right) \mp 4i\pi\right)\right.\right. \\
&+\frac{h_0^\Gamma}{2} + \frac{h_1^\Gamma}{2}\left(\ln\left(\frac{16\,(P^z)^4}{\mu^4}\right) + \frac{\mathrm{Re}\{J_1^*(J_2+J_3)\}}{|J_1|^2}\right) \\
&\left.\left.+\frac{\mathrm{Re}\{J_1^*(J_4+J_5)\} - (|J_2|^2+|J_3|^2) \pm 2\pi\mathrm{Im}\{J_1^*(J_2+J_3)\}}{|J_1|^2}\right] + O(\alpha_s^2)\right\}
\end{aligned} \tag{6.19}$$

where

$$\begin{aligned}
J_1 &= \int_{-\infty}^{\infty} dx\tilde{\Psi}\left(x,b,P^z\right) & J_2 &= \int_{-\infty}^{\infty} dx\tilde{\Psi}\left(x,b,P^z\right)\ln|x| \\
J_3 &= \int_{-\infty}^{\infty} dx\tilde{\Psi}\left(x,b,P^z\right)\ln|1-x| & J_4 &= \int_{-\infty}^{\infty} dx\tilde{\Psi}\left(x,b,P^z\right)\ln^2|x| \\
J_5 &= \int_{-\infty}^{\infty} dx\tilde{\Psi}\left(x,b,P^z\right)\ln^2|1-x|
\end{aligned} \tag{6.20}$$

Here $\tilde{f}(x,b,\mu,\zeta_z)$ is the quasi-TMDPDF, $K_{LO}(b,\mu)$ is the leading order Collins-Soper kernel which is obtained from the first term of Eq. (6.12), and $S_{r,LO}^{\frac{1}{2}}$ is the reduced soft function also at leading order which is obtained by setting $H = 1$ in Eq. (6.14). The colors in Eq. (6.19) indicate which part the different corrections belong to. The red part comes from the matching kernel of the quasi-TMDPDF and TMDPDF. The blue part comes from the Collins-Soper kernel which is identical to the 1-loop part in Eq. (6.12). The green part comes from the reduced soft function. This part is different compared to the Eq. (6.15). This particular form of the matching is obtained by taking the matching kernel out of the integral over x and x'. One then obtains the matching in terms of the 5 integrals J_i. The correction coming from the Collins-Soper kernel includes an "unphysical" imaginary part. We expect this to be cancelled by power mass corrections $O\left(\frac{\Lambda_{\mathrm{QCD}}^2}{\zeta_z}, \frac{M^2}{(P^z)^2}, \frac{1}{b^2\zeta_z}\right)$. In the present calculation, we have

ignored this imaginary part.

In Figure 6.24 we show the physical TMDPDF matched upto $O(\alpha_s)$ for transverse separations upto $b = 4a \sim 0.36\,\text{fm}$. We perform the matching at $\zeta = \mu^2 = 4\,\text{GeV}^2$. We observe that the TMDPDF is consistent for all values of b especially for $x > 0.4$.

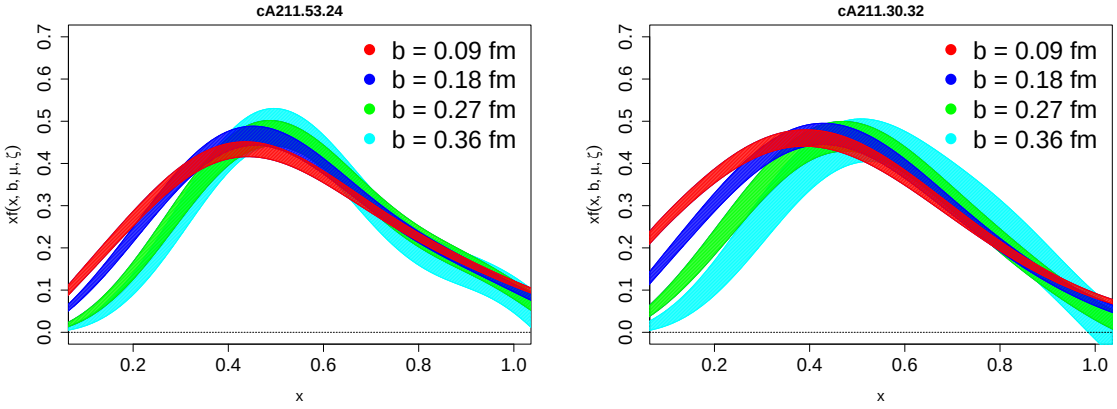

Figure 6.24: Physical TMDPDF matched upto $O(\alpha_s)$ for lattice ensembles cA211.53.24 (left) and cA211.30.32 (right). Both calculated at the same physical rapidity and matched to $\zeta = \mu^2 = 4\,\text{GeV}^2$.

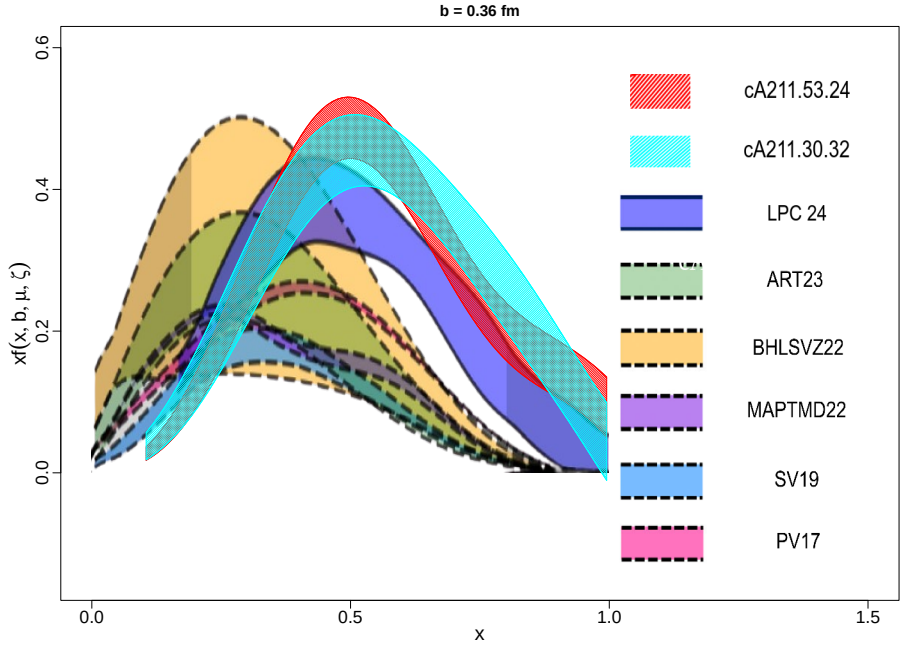

Figure 6.25: Comparison of our result to [72] at $b = 0.36\,\text{fm}$. The background plot is taken from Figure 19 of [72] where they compare their results to global fits performed in ART23 [29], BHLSVZ22 [30], MAPTMD22 [31], SV19 [32], and PV17 [33].

We compare our result to the recently published first calculation of the unpolarized TMDPDF on the lattice [72] for a comparable transverse separation in Figure 6.25. We must note that the LPC

calculation is much more involved. The authors of [72] performed their calculation on a physical point ensemble. They also used different heavier valence pion masses and different momenta and did an extrapolation to the physical pion mass and infinite momentum. They also did an estimate of the systematic uncertatities. It is still interesting how well our exploratory calculation agrees with their result. We also observe that our result from the 2 ensembles completely agree with each other. However, a more systematic study is needed to understand the pion mass dependence and finite volume effects. These results for the matching along with the full matching for the physical point ensemble will appear in a forthcoming publication [149].

CHAPTER 7

Summary and outlook

The main objective of this thesis was the calculation of the unpolarized transverse momentum dependent parton distribution functions for the nucleon in first principle using lattice QCD. For that purpose, we have calculated the quasi-TMDPDF, the Collins-Soper kernel and the reduced soft function nonperturbatively. We have systematically studied the renormalization of the underlying staple-shaped Wilson line quark bilinear operators and have shown that mixing from other operators is negligible. We have studied an already proposed alternative renormlization procedure called SDR and proposed a similar method using the RI/MOM scheme called RI-short. We found the results from the two different schemes to be compatible especially at large distances. We also found our calculation of the Collins-Soper kernel and the soft function to be comparable to previous lattice calculations. Finally, we performed a consistent matching to the light-cone TMDPDF up to 1-loop order in perturbation theory. We compared our result to a recently published calculation and found them to be consistent. Given the exploratory nature of this work, we find the results to be promising. We have also developed a more efficient method for computation of the staples which reduces the computational cost exponentially and would be useful for future calculations on larger lattice sizes.

These first results are not yet at the point to be useful for future extractions of TMDPDFs from experimental data. However, we believe that with the ongoing calculations on the physical pion mass ensemble and the upcoming work on the continuum extrapolation, we will be able to provide results that are useful for the global fits of TMDPDFs. We also intend to perform a thorough study of the systematic uncertainties in the future.

APPENDIX A

Conventions

In this work, the Dirac gamma matrices are defined according to the chiral representation, where

$$\gamma_\mu = \begin{pmatrix} 0 & e_\mu \\ e_\mu^\dagger & 0 \end{pmatrix} \tag{A.1}$$

with e_μ being the 2×2 matrices

$$e_0 = -\mathbb{1}_2, \qquad e_k = -i\sigma_k \tag{A.2}$$

where σ_k are the Pauli matrices

$$\sigma_1 = \begin{pmatrix} 0 & 1 \\ 1 & 0 \end{pmatrix}, \quad \sigma_2 = \begin{pmatrix} 0 & -i \\ i & 0 \end{pmatrix}, \quad \sigma_3 = \begin{pmatrix} 1 & 0 \\ 0 & -1 \end{pmatrix} \tag{A.3}$$

In this definition, one gets

$$\gamma_\mu = \gamma_\mu^\dagger, \qquad \{\gamma_\mu, \gamma_\nu\} = 2\delta_{\mu\nu} \tag{A.4}$$

One also defines

$$\gamma_5 = \gamma_0\gamma_1\gamma_2\gamma_3 \quad \Longrightarrow \quad \gamma_5 = \begin{pmatrix} 1 & 0 \\ 0 & -1 \end{pmatrix} \tag{A.5}$$

with the properties

$$\gamma_5 = \gamma_5^\dagger, \qquad \gamma_5^2 = \mathbb{1} \tag{A.6}$$

Bibliography

[1] J. Baggott, *Mass: The Quest to Understand Matter From Greek Atoms to Quantum Fields*, Oxford University Press UK, 2017.

[2] I. Newton, *Philosophiæ Naturalis Principia Mathematica*, England, 1687.

[3] J. Dalton, *A New System of Chemical Philosophy*, Manchester, England, 1808.

[4] A. Avogadro,
Essai d'une maniere de determiner les masses relatives des molecules elementaires des corps, et les proportions selon lesquelles elles entrent dans ces combinaisons,
Journal de Physique **73** (1811) 58.

[5] M. Faraday, *VI. Experimental researches in electricity.-Seventh Series*,
Phil. Trans. R. Soc. **124** (1834) 77.

[6] J. Thmoson, *Cathode Rays*, Philosophical Magazine Series 5 **44** (1897) 293.

[7] E. Rutherford, *The Scattering of α and β Particles by Matter and the Structure of the Atom*,
Philosophical Magazine Series 6 **21** (1911) 669.

[8] N. Bohr, *On the constitution of atoms and molecules*,
Philosophical Magazine Series 6 **26** (1913) 1.

[9] E. Rutherford, *Collisions of α particles with light atoms, IV. An anomalous effect in Nitrogen*,
Philosophical Magazine Series 6 **37** (1919) 581.

[10] J. Chadwick, *The Existence of a Neutron*, Proc. Roy. Soc. Lond. A **136** (1932) 692.

[11] H. Yukawa, *On the Interaction of Elementary Particles I*,
Proc. Phys. Math. Soc. Jap. **17** (1935) 48.

[12] C. M. G. Lattes, G. P. S. Occhialini and C. F. Powell,
Observations on the Tracks of Slow Mesons in Photographic Emulsions. 1,
Nature **160** (1947) 453.

[13] C. M. G. Lattes, G. P. S. Occhialini and C. F. Powell,
Observations on the Tracks of Slow Mesons in Photographic Emulsions. 2,
Nature **160** (1947) 486.

[14] M. Gell-Mann, *The Eightfold Way: A Theory of strong interaction symmetry*, (1961).

[15] Y. Ne'eman, *Derivation of strong interactions from a gauge invariance*,
Nucl. Phys. **26** (1961) 222, ed. by R. Ruffini and Y. Verbin.

[16] M. Gell-Mann, *A Schematic Model of Baryons and Mesons*, Phys. Lett. **8** (1964) 214.

[17] G. Zweig, "An SU(3) model for strong interaction symmetry and its breaking. Version 2", *DEVELOPMENTS IN THE QUARK THEORY OF HADRONS. VOL. 1. 1964 - 1978*, ed. by D. B. Lichtenberg and S. P. Rosen, 1964 22.

[18] O. W. Greenberg, *Spin and Unitary Spin Independence in a Paraquark Model of Baryons and Mesons*, Phys. Rev. Lett. **13** (1964) 598.

[19] R. Boussarie et al., *TMD Handbook*, (2023), arXiv: 2304.03302 [hep-ph].

[20] R. W. Mcallister and R. Hofstadter, *Elastic Scattering of 188-MeV Electrons From the Proton and the α Particle*, Phys. Rev. **102** (1956) 851.

[21] M. R. Yearian and R. Hofstadter, *Magnetic Form Factor of the Neutron*, Phys. Rev. **110** (1958) 552.

[22] E. D. Bloom et al., *High-Energy Inelastic e p Scattering at 6-Degrees and 10-Degrees*, Phys. Rev. Lett. **23** (1969) 930.

[23] R. P. Feynman, *Very high-energy collisions of hadrons*, Phys. Rev. Lett. **23** (1969) 1415, ed. by L. M. Brown.

[24] J. Ashman et al., *A measurement of the spin asymmetry and determination of the structure function g1 in deep inelastic muon-proton scattering*, Physics Letters B **206** (1988) 364, ISSN: 0370-2693, URL: https://www.sciencedirect.com/science/article/pii/0370269388915237.

[25] E.-C. Aschenauer et al., *The RHIC SPIN Program: Achievements and Future Opportunities*, (2015), arXiv: 1501.01220 [nucl-ex].

[26] S. Diehl, *Experimental exploration of the 3D nucleon structure*, Prog. Part. Nucl. Phys. **133** (2023) 104069.

[27] A. Airapetian et al., *Multiplicities of charged pions and kaons from semi-inclusive deep-inelastic scattering by the proton and the deuteron*, Phys. Rev. D **87** (2013) 074029, arXiv: 1212.5407 [hep-ex].

[28] M. Aghasyan et al., *Transverse-momentum-dependent Multiplicities of Charged Hadrons in Muon-Deuteron Deep Inelastic Scattering*, Phys. Rev. D **97** (2018) 032006, arXiv: 1709.07374 [hep-ex].

[29] V. Moos, I. Scimemi, A. Vladimirov and P. Zurita, *Extraction of unpolarized transverse momentum distributions from the fit of Drell-Yan data at N^4LL*, JHEP **05** (2024) 036, arXiv: 2305.07473 [hep-ph].

[30] M. Bury, F. Hautmann, S. Leal-Gomez, I. Scimemi, A. Vladimirov and P. Zurita, *PDF bias and flavor dependence in TMD distributions*, JHEP **10** (2022) 118, arXiv: 2201.07114 [hep-ph].

[31] A. Bacchetta, V. Bertone, C. Bissolotti, G. Bozzi, M. Cerutti, F. Piacenza, M. Radici and A. Signori, *Unpolarized transverse momentum distributions from a global fit of Drell-Yan and semi-inclusive deep-inelastic scattering data*, JHEP **10** (2022) 127, arXiv: 2206.07598 [hep-ph].

[32] I. Scimemi and A. Vladimirov, *Non-perturbative structure of semi-inclusive deep-inelastic and Drell-Yan scattering at small transverse momentum*, JHEP **06** (2020) 137, arXiv: 1912.06532 [hep-ph].

[33] A. Bacchetta, F. Delcarro, C. Pisano, M. Radici and A. Signori, *Extraction of partonic transverse momentum distributions from semi-inclusive deep-inelastic scattering, Drell-Yan and Z-boson production*, JHEP **06** (2017) 081, [Erratum: JHEP 06, 051 (2019)], arXiv: 1703.10157 [hep-ph].

[34] A. Accardi et al., *Electron Ion Collider: The Next QCD Frontier: Understanding the glue that binds us all*, Eur. Phys. J. A **52** (2016) 268, ed. by A. Deshpande, Z. E. Meziani and J. W. Qiu, arXiv: 1212.1701 [nucl-ex].

[35] K. G. Wilson, *Confinement of Quarks*, Phys. Rev. D **10** (1974) 2445, ed. by J. C. Taylor.

[36] P. Hagler, B. U. Musch, J. W. Negele and A. Schafer, *Intrinsic quark transverse momentum in the nucleon from lattice QCD*, EPL **88** (2009) 61001, arXiv: 0908.1283 [hep-lat].

[37] B. U. Musch, P. Hagler, M. Engelhardt, J. W. Negele and A. Schafer, *Sivers and Boer-Mulders observables from lattice QCD*, Phys. Rev. D **85** (2012) 094510, arXiv: 1111.4249 [hep-lat].

[38] B. Yoon, M. Engelhardt, R. Gupta, T. Bhattacharya, J. R. Green, B. U. Musch, J. W. Negele, A. V. Pochinsky, A. Schäfer and S. N. Syritsyn, *Nucleon Transverse Momentum-dependent Parton Distributions in Lattice QCD: Renormalization Patterns and Discretization Effects*, Phys. Rev. D **96** (2017) 094508, arXiv: 1706.03406 [hep-lat].

[39] K.-F. Liu, *Parton degrees of freedom from the path integral formalism*, Phys. Rev. D **62** (2000) 074501, arXiv: hep-ph/9910306.

[40] K.-F. Liu, *Parton Distribution Function from the Hadronic Tensor on the Lattice*, PoS **LATTICE2015** (2016) 115, arXiv: 1603.07352 [hep-ph].

[41] U. Aglietti, M. Ciuchini, G. Corbo, E. Franco, G. Martinelli and L. Silvestrini, *Model independent determination of the light cone wave functions for exclusive processes*, Phys. Lett. B **441** (1998) 371, arXiv: hep-ph/9806277.

[42] A. Abada, P. Boucaud, G. Herdoiza, J. P. Leroy, J. Micheli, O. Pene and J. Rodriguez-Quintero, *Preliminaries on a lattice analysis of the pion light cone wave function: A Partonic signal?*, Phys. Rev. D **64** (2001) 074511, arXiv: hep-ph/0105221.

[43] W. Detmold and C. J. D. Lin, *Deep-inelastic scattering and the operator product expansion in lattice QCD*, Phys. Rev. D **73** (2006) 014501, arXiv: hep-lat/0507007.

[44] V. Braun and D. Müller, *Exclusive processes in position space and the pion distribution amplitude*, Eur. Phys. J. C **55** (2008) 349, arXiv: 0709.1348 [hep-ph].

[45] B. U. Musch, P. Hagler, J. W. Negele and A. Schafer,
Exploring quark transverse momentum distributions with lattice QCD,
Phys. Rev. D **83** (2011) 094507, arXiv: 1011.1213 [hep-lat].

[46] X. Ji, *Parton Physics on a Euclidean Lattice*, Phys. Rev. Lett. **110** (2013) 262002,
arXiv: 1305.1539 [hep-ph].

[47] X. Ji, *Parton Physics from Large-Momentum Effective Field Theory*,
Sci. China Phys. Mech. Astron. **57** (2014) 1407, arXiv: 1404.6680 [hep-ph].

[48] A. V. Radyushkin, *Quasi-parton distribution functions, momentum distributions, and pseudo-parton distribution functions*, Phys. Rev. D **96** (2017) 034025,
arXiv: 1705.01488 [hep-ph].

[49] K. Orginos, A. Radyushkin, J. Karpie and S. Zafeiropoulos,
Lattice QCD exploration of parton pseudo-distribution functions,
Phys. Rev. D **96** (2017) 094503, arXiv: 1706.05373 [hep-ph].

[50] K.-F. Liu, *PDF in PDFs from Hadronic Tensor and LaMET*, Phys. Rev. D **102** (2020) 074502,
arXiv: 2007.15075 [hep-ph].

[51] Y.-Q. Ma and J.-W. Qiu,
Exploring Partonic Structure of Hadrons Using ab initio Lattice QCD Calculations,
Phys. Rev. Lett. **120** (2018) 022003, arXiv: 1709.03018 [hep-ph].

[52] R. S. Sufian, J. Karpie, C. Egerer, K. Orginos, J.-W. Qiu and D. G. Richards,
Pion Valence Quark Distribution from Matrix Element Calculated in Lattice QCD,
Phys. Rev. D **99** (2019) 074507, arXiv: 1901.03921 [hep-lat].

[53] X. Ji, P. Sun, X. Xiong and F. Yuan,
Soft factor subtraction and transverse momentum dependent parton distributions on the lattice,
Phys. Rev. D **91** (2015) 074009, arXiv: 1405.7640 [hep-ph].

[54] X. Ji, L.-C. Jin, F. Yuan, J.-H. Zhang and Y. Zhao,
Transverse momentum dependent parton quasidistributions, Phys. Rev. D **99** (2019) 114006,
arXiv: 1801.05930 [hep-ph].

[55] M. A. Ebert, I. W. Stewart and Y. Zhao,
Determining the Nonperturbative Collins-Soper Kernel From Lattice QCD,
Phys. Rev. D **99** (2019) 034505, arXiv: 1811.00026 [hep-ph].

[56] M. A. Ebert, I. W. Stewart and Y. Zhao,
Towards Quasi-Transverse Momentum Dependent PDFs Computable on the Lattice,
JHEP **09** (2019) 037, arXiv: 1901.03685 [hep-ph].

[57] M. A. Ebert, I. W. Stewart and Y. Zhao,
Renormalization and Matching for the Collins-Soper Kernel from Lattice QCD,
JHEP **03** (2020) 099, arXiv: 1910.08569 [hep-ph].

[58] X. Ji, Y. Liu and Y.-S. Liu, *TMD soft function from large-momentum effective theory*,
Nucl. Phys. B **955** (2020) 115054, arXiv: 1910.11415 [hep-ph].

[59] X. Ji, Y. Liu and Y.-S. Liu, *Transverse-momentum-dependent parton distribution functions from large-momentum effective theory*, Phys. Lett. B **811** (2020) 135946,
arXiv: 1911.03840 [hep-ph].

[60] A. A. Vladimirov and A. Schäfer,
Transverse momentum dependent factorization for lattice observables,
Phys. Rev. D **101** (2020) 074517, arXiv: 2002.07527 [hep-ph].

[61] M. A. Ebert, S. T. Schindler, I. W. Stewart and Y. Zhao,
One-loop Matching for Spin-Dependent Quasi-TMDs, JHEP **09** (2020) 099,
arXiv: 2004.14831 [hep-ph].

[62] X. Ji, Y.-S. Liu, Y. Liu, J.-H. Zhang and Y. Zhao, *Large-momentum effective theory*,
Rev. Mod. Phys. **93** (2021) 035005, arXiv: 2004.03543 [hep-ph].

[63] Q.-A. Zhang et al.,
Lattice-QCD Calculations of TMD Soft Function Through Large-Momentum Effective Theory,
Phys. Rev. Lett. **125** (2020) 192001, arXiv: 2005.14572 [hep-lat].

[64] Y. Li et al., *Lattice QCD Study of Transverse-Momentum Dependent Soft Function*,
Phys. Rev. Lett. **128** (2022) 062002, arXiv: 2106.13027 [hep-lat].

[65] M.-H. Chu et al.,
Lattice calculation of the intrinsic soft function and the Collins-Soper kernel,
JHEP **08** (2023) 172, arXiv: 2306.06488 [hep-lat].

[66] P. Shanahan, M. L. Wagman and Y. Zhao,
Nonperturbative renormalization of staple-shaped Wilson line operators in lattice QCD,
Phys. Rev. D **101** (2020) 074505, arXiv: 1911.00800 [hep-lat].

[67] M. Schlemmer, A. Vladimirov, C. Zimmermann, M. Engelhardt and A. Schäfer,
Determination of the Collins-Soper Kernel from Lattice QCD, (2021),
arXiv: 2103.16991 [hep-lat].

[68] P. Shanahan, M. Wagman and Y. Zhao,
Lattice QCD calculation of the Collins-Soper kernel from quasi-TMDPDFs,
Phys. Rev. D **104** (2021) 114502, arXiv: 2107.11930 [hep-lat].

[69] M.-H. Chu et al., *Nonperturbative determination of the Collins-Soper kernel from quasitransverse-momentum-dependent wave functions*, Phys. Rev. D **106** (2022) 034509,
arXiv: 2204.00200 [hep-lat].

[70] A. Avkhadiev, P. E. Shanahan, M. L. Wagman and Y. Zhao,
Collins-Soper kernel from lattice QCD at the physical pion mass,
Phys. Rev. D **108** (2023) 114505, arXiv: 2307.12359 [hep-lat].

[71] A. Avkhadiev, P. E. Shanahan, M. L. Wagman and Y. Zhao,
Determination of the Collins-Soper Kernel from Lattice QCD,
Phys. Rev. Lett. **132** (2024) 231901, arXiv: 2402.06725 [hep-lat].

[72] J.-C. He, M.-H. Chu, J. Hua, X. Ji, A. Schäfer, Y. Su, W. Wang, Y.-B. Yang, J.-H. Zhang and Q.-A. Zhang, *Unpolarized transverse momentum dependent parton distributions of the nucleon from lattice QCD*, Phys. Rev. D **109** (2024) 114513,
arXiv: 2211.02340 [hep-lat].

[73] K. Zhang, X. Ji, Y.-B. Yang, F. Yao and J.-H. Zhang,
Renormalization of Transverse-Momentum-Dependent Parton Distribution on the Lattice,
Phys. Rev. Lett. **129** (2022) 082002, arXiv: 2205.13402 [hep-lat].

[74] C. Alexandrou, S. Bacchio, K. Cichy, M. Constantinou, X. Feng, K. Jansen, C. Liu, A. Sen, G. Spanoudes, F. Steffens and J. Tarello, *Nonperturbative renormalization of asymmetric staple-shaped operators in twisted mass lattice QCD*, Phys. Rev. D **108** (2023) 114503, arXiv: 2305.11824 [hep-lat].

[75] A. Sen, *Nuclear parity violation from 4-quark operators*, unpublished, Rheinischen Friedrich-Wilhelms-Universität Bonn, 2021.

[76] C. Gattringer and C. B. Lang, *Quantum chromodynamics on the lattice*, vol. 788, Berlin: Springer, 2010, ISBN: 978-3-642-01849-7, 978-3-642-01850-3.

[77] H. J. Rothe, *Lattice Gauge Theories : An Introduction (Fourth Edition)*, vol. 43, World Scientific Publishing Company, 2012, ISBN: 978-981-4365-87-1, 978-981-4365-85-7.

[78] P. H. Ginsparg and K. G. Wilson, *A Remnant of Chiral Symmetry on the Lattice*, Phys. Rev. D **25** (1982) 2649.

[79] H. Neuberger, *More about exactly massless quarks on the lattice*, Phys. Lett. B **427** (1998) 353, arXiv: hep-lat/9801031.

[80] P. Hasenfratz, *Prospects for perfect actions*, Nucl. Phys. B Proc. Suppl. **63** (1998) 53, ed. by C. T. H. Davies, I. M. Barbour, K. C. Bowler, R. D. Kenway, B. J. Pendleton and D. G. Richards, arXiv: hep-lat/9709110.

[81] J. B. Kogut and L. Susskind, *Hamiltonian Formulation of Wilson's Lattice Gauge Theories*, Phys. Rev. D **11** (1975) 395.

[82] D. B. Kaplan, *A Method for simulating chiral fermions on the lattice*, Phys. Lett. B **288** (1992) 342, arXiv: hep-lat/9206013.

[83] R. Frezzotti, P. A. Grassi, S. Sint and P. Weisz, *Lattice QCD with a chirally twisted mass term*, JHEP **08** (2001) 058, arXiv: hep-lat/0101001.

[84] A. Shindler, *Twisted mass lattice QCD*, Phys. Rept. **461** (2008) 37, arXiv: 0707.4093 [hep-lat].

[85] B. Sheikholeslami and R. Wohlert, *Improved Continuum Limit Lattice Action for QCD with Wilson Fermions*, Nucl. Phys. B **259** (1985) 572.

[86] C. Alexandrou et al., *Simulating twisted mass fermions at physical light, strange and charm quark masses*, Phys. Rev. D **98** (2018) 054518, arXiv: 1807.00495 [hep-lat].

[87] C. W. Gardiner and D. P. Majumdar, *Effect of a transverse momentum distribution in the parton model*, Phys. Rev. D **2** (1970) 2040.

[88] F. E. Close, F. Halzen and D. M. Scott, *What Is the Transverse Momentum of Partons?*, Phys. Lett. B **68** (1977) 447.

[89] D. E. Soper, *Large Transverse Momentum Partons and Massive mu Pair Production*, Phys. Rev. Lett. **38** (1977) 461.

[90] G. Parisi and R. Petronzio, *Small Transverse Momentum Distributions in Hard Processes*, Nucl. Phys. B **154** (1979) 427.

[91] J. C. Collins and D. E. Soper, *Back-To-Back Jets in QCD*,
Nucl. Phys. B **193** (1981) 381, [Erratum: Nucl.Phys.B 213, 545 (1983)].

[92] J. C. Collins and D. E. Soper, *Back-To-Back Jets: Fourier Transform from B to K-Transverse*,
Nucl. Phys. B **197** (1982) 446.

[93] J. C. Collins, D. E. Soper and G. F. Sterman,
Factorization for One Loop Corrections in the Drell-Yan Process,
Nucl. Phys. B **223** (1983) 381.

[94] J. C. Collins, D. E. Soper and G. F. Sterman,
Factorization for Short Distance Hadron - Hadron Scattering, Nucl. Phys. B **261** (1985) 104.

[95] J. C. Collins, D. E. Soper and G. F. Sterman,
Transverse Momentum Distribution in Drell-Yan Pair and W and Z Boson Production,
Nucl. Phys. B **250** (1985) 199.

[96] G. T. Bodwin, *Factorization of the Drell-Yan Cross-Section in Perturbation Theory*,
Phys. Rev. D **31** (1985) 2616, [Erratum: Phys.Rev.D 34, 3932 (1986)].

[97] X.-d. Ji, J.-P. Ma and F. Yuan, *QCD factorization for spin-dependent cross sections in DIS and Drell-Yan processes at low transverse momentum*, Phys. Lett. B **597** (2004) 299,
arXiv: hep-ph/0405085.

[98] X.-d. Ji, J.-p. Ma and F. Yuan,
QCD factorization for semi-inclusive deep-inelastic scattering at low transverse momentum,
Phys. Rev. D **71** (2005) 034005, arXiv: hep-ph/0404183.

[99] J. C. Collins and T. C. Rogers, *Equality of Two Definitions for Transverse Momentum Dependent Parton Distribution Functions*, Phys. Rev. D **87** (2013) 034018,
arXiv: 1210.2100 [hep-ph].

[100] M. G. Echevarría, A. Idilbi and I. Scimemi, *Soft and Collinear Factorization and Transverse Momentum Dependent Parton Distribution Functions*, Phys. Lett. B **726** (2013) 795,
arXiv: 1211.1947 [hep-ph].

[101] J. Collins and T. C. Rogers, *Connecting Different TMD Factorization Formalisms in QCD*,
Phys. Rev. D **96** (2017) 054011, arXiv: 1705.07167 [hep-ph].

[102] A. Bacchetta, *Transverse Mometum Distributions*, 2012, URL:
https://www2.pv.infn.it/~bacchett/teaching/Bacchetta_Trento2012.pdf.

[103] J. Collins, *Foundations of perturbative QCD*, vol. 32, Cambridge University Press, 2013,
ISBN: 978-1-107-64525-7, 978-1-107-64525-7, 978-0-521-85533-4, 978-1-139-09782-6.

[104] A. Bacchetta, U. D'Alesio, M. Diehl and C. A. Miller,
Single-spin asymmetries: The Trento conventions, Phys. Rev. D **70** (2004) 117504,
arXiv: hep-ph/0410050.

[105] T. Muta, *Foundations of quantum chromodynamics. Second edition*, vol. 57, 1998.

[106] P. J. Mulders and R. D. Tangerman,
The Complete tree level result up to order 1/Q for polarized deep inelastic leptoproduction,
Nucl. Phys. B **461** (1996) 197, [Erratum: Nucl.Phys.B 484, 538–540 (1997)],
arXiv: hep-ph/9510301.

[107] D. Boer and P. J. Mulders, *Time reversal odd distribution functions in leptoproduction*, Phys. Rev. D **57** (1998) 5780, arXiv: hep-ph/9711485.

[108] V. Barone, A. Drago and P. G. Ratcliffe, *Transverse polarisation of quarks in hadrons*, Phys. Rept. **359** (2002) 1, arXiv: hep-ph/0104283.

[109] R. D. Tangerman and P. J. Mulders, *Intrinsic transverse momentum and the polarized Drell-Yan process*, Phys. Rev. D **51** (1995) 3357, arXiv: hep-ph/9403227.

[110] A. V. Manohar and M. B. Wise, *Heavy quark physics*, vol. 10, 2000, ISBN: 978-0-521-03757-0.

[111] M. A. Ebert, S. T. Schindler, I. W. Stewart and Y. Zhao, *Factorization connecting continuum & lattice TMDs*, JHEP **04** (2022) 178, arXiv: 2201.08401 [hep-ph].

[112] J. Collins, *New definition of TMD parton densities*, Int. J. Mod. Phys. Conf. Ser. **4** (2011) 85, ed. by I. Balitsky, A. Prokudin and A. Radyushkin, arXiv: 1107.4123 [hep-ph].

[113] Z.-F. Deng, W. Wang and J. Zeng, *Transverse-momentum-dependent wave functions and soft functions at one-loop in large momentum effective theory*, JHEP **09** (2022) 046, arXiv: 2207.07280 [hep-th].

[114] M. Constantinou, H. Panagopoulos and G. Spanoudes, *One-loop renormalization of staple-shaped operators in continuum and lattice regularizations*, Phys. Rev. D **99** (2019) 074508, arXiv: 1901.03862 [hep-lat].

[115] Y. Ji, J.-H. Zhang, S. Zhao and R. Zhu, *Renormalization and mixing of staple-shaped Wilson line operators on the lattice revisited*, Phys. Rev. D **104** (2021) 094510, arXiv: 2104.13345 [hep-ph].

[116] M. Constantinou and H. Panagopoulos, *Perturbative renormalization of quasi-parton distribution functions*, Phys. Rev. D **96** (2017) 054506, arXiv: 1705.11193 [hep-lat].

[117] K. Zhang, Y.-Y. Li, Y.-K. Huo, A. Schäfer, P. Sun and Y.-B. Yang, *RI/MOM renormalization of the parton quasidistribution functions in lattice regularization*, Phys. Rev. D **104** (2021) 074501, arXiv: 2012.05448 [hep-lat].

[118] V. M. Braun, A. Vladimirov and J.-H. Zhang, *Power corrections and renormalons in parton quasidistributions*, Phys. Rev. D **99** (2019) 014013, arXiv: 1810.00048 [hep-ph].

[119] X. Ji, Y. Liu, A. Schäfer, W. Wang, Y.-B. Yang, J.-H. Zhang and Y. Zhao, *A Hybrid Renormalization Scheme for Quasi Light-Front Correlations in Large-Momentum Effective Theory*, Nucl. Phys. B **964** (2021) 115311, arXiv: 2008.03886 [hep-ph].

[120] J.-C. He, M.-H. Chu, J. Hua, X. Ji, A. Schäfer, Y. Su, W. Wang, Y. Yang, J.-H. Zhang and Q.-A. Zhang, *Unpolarized Transverse-Momentum-Dependent Parton Distributions of the Nucleon from Lattice QCD*, (2022), arXiv: 2211.02340 [hep-lat].

[121] J.-W. Chen, T. Ishikawa, L. Jin, H.-W. Lin, J.-H. Zhang and Y. Zhao, *Symmetry properties of nonlocal quark bilinear operators on a Lattice*, Chin. Phys. C **43** (2019) 103101, arXiv: 1710.01089 [hep-lat].

[122] G. Martinelli, C. Pittori, C. T. Sachrajda, M. Testa and A. Vladikas, *A General method for nonperturbative renormalization of lattice operators*, Nucl. Phys. B **445** (1995) 81, arXiv: hep-lat/9411010.

[123] C. Alexandrou, K. Cichy, M. Constantinou, K. Hadjiyiannakou, K. Jansen, H. Panagopoulos and F. Steffens, *A complete non-perturbative renormalization prescription for quasi-PDFs*, Nucl. Phys. B **923** (2017) 394, arXiv: 1706.00265 [hep-lat].

[124] J. R. Green, K. Jansen and F. Steffens, *Improvement, generalization, and scheme conversion of Wilson-line operators on the lattice in the auxiliary field approach*, Phys. Rev. D **101** (2020) 074509, arXiv: 2002.09408 [hep-lat].

[125] K. Symanzik, *Continuum Limit and Improved Action in Lattice Theories. 2. O(N) Nonlinear Sigma Model in Perturbation Theory*, Nucl. Phys. B **226** (1983) 205.

[126] K. Symanzik, *Continuum Limit and Improved Action in Lattice Theories. 1. Principles and φ^4 Theory*, Nucl. Phys. B **226** (1983) 187.

[127] M. Constantinou, V. Lubicz, H. Panagopoulos and F. Stylianou, *O(a**2) corrections to the one-loop propagator and bilinears of clover fermions with Symanzik improved gluons*, JHEP **10** (2009) 064, arXiv: 0907.0381 [hep-lat].

[128] M. Constantinou, M. Costa, M. Göckeler, R. Horsley, H. Panagopoulos, H. Perlt, P. E. L. Rakow, G. Schierholz and A. Schiller, *Perturbatively improving regularization-invariant momentum scheme renormalization constants*, Phys. Rev. D **87** (2013) 096019, arXiv: 1303.6776 [hep-lat].

[129] C. Alexandrou, M. Constantinou and H. Panagopoulos, *Renormalization functions for Nf=2 and Nf=4 twisted mass fermions*, Phys. Rev. D **95** (2017) 034505, arXiv: 1509.00213 [hep-lat].

[130] M. Constantinou and H. Panagopoulos, *Improved renormalization scheme for nonlocal operators*, Phys. Rev. D **107** (2023) 014503, arXiv: 2207.09977 [hep-lat].

[131] G. Spanoudes, M. Constantinou and H. Panagopoulos, *Renormalization of asymmetric staple-shaped Wilson-line operators in lattice and continuum perturbation theory*, Phys. Rev. D **109** (2024) 114501, arXiv: 2401.01182 [hep-lat].

[132] G. Martinelli and C. T. Sachrajda, *A Lattice Study of Nucleon Structure*, Nucl. Phys. B **316** (1989) 355.

[133] M. Albanese et al., *Glueball Masses and String Tension in Lattice QCD*, Phys. Lett. B **192** (1987) 163.

[134] S. Gusken, *A Study of smearing techniques for hadron correlation functions*, Nucl. Phys. B Proc. Suppl. **17** (1990) 361, ed. by N. Cabibbo, E. Marinari, G. Parisi, R. Petronzio, L. Maiani, G. Martinelli and R. Pettorino.

[135] C. Morningstar and M. J. Peardon, *Analytic smearing of SU(3) link variables in lattice QCD*, Phys. Rev. D **69** (2004) 054501, arXiv: hep-lat/0311018.

[136] G. S. Bali, B. Lang, B. U. Musch and A. Schäfer, *Novel quark smearing for hadrons with high momenta in lattice QCD*, Phys. Rev. D **93** (2016) 094515, arXiv: 1602.05525 [hep-lat].

[137] C. Alexandrou, K. Cichy, M. Constantinou, K. Hadjiyiannakou, K. Jansen, A. Scapellato and F. Steffens, *Systematic uncertainties in parton distribution functions from lattice QCD simulations at the physical point*, Phys. Rev. D **99** (2019) 114504, arXiv: 1902.00587 [hep-lat].

[138] S. Bacchio, K. Hadjiyiannakou et al., *PLEGMA*, URL: https://github.com/cylqcd/PLEGMA.

[139] M. A. Clark, R. Babich, K. Barros et al., *QUDA*, URL: https://github.com/lattice/quda.

[140] M. A. Clark, R. Babich, K. Barros, R. C. Brower and C. Rebbi, *Solving Lattice QCD systems of equations using mixed precision solvers on GPUs*, Comput. Phys. Commun. **181** (2010) 1517, arXiv: 0911.3191 [hep-lat].

[141] R. Babich, M. A. Clark, B. Joo, G. Shi, R. C. Brower and S. Gottlieb, "Scaling lattice QCD beyond 100 GPUs", *International Conference for High Performance Computing, Networking, Storage and Analysis*, 2011, arXiv: 1109.2935 [hep-lat].

[142] M. A. Clark, B. Joó, A. Strelchenko, M. Cheng, A. Gambhir and R. C. Brower, "Accelerating lattice QCD multigrid on GPUs using fine-grained parallelization", *International Conference for High Performance Computing, Networking, Storage and Analysis*, 2016, arXiv: 1612.07873 [hep-lat].

[143] R Core Team, *R: A Language and Environment for Statistical Computing*, R Foundation for Statistical Computing, Vienna, Austria, 2021, URL: https://www.R-project.org/.

[144] B. Kostrzewa, J. Ostmeyer, M. Ueding and C. Urbach, *hadron: Analysis Framework for Monte Carlo Simulation Data in Physics*, R package version 3.1.0, 2020, URL: https://CRAN.R-project.org/package=hadron.

[145] J. Bezanson, A. Edelman, S. Karpinski and V. B. Shah, *Julia: A fresh approach to numerical computing*, SIAM review **59** (2017) 65, URL: https://doi.org/10.1137/141000671.

[146] G. Van Rossum and F. L. Drake Jr, *Python reference manual*, Centrum voor Wiskunde en Informatica Amsterdam, 1995.

[147] C. Alexandrou, K. Cichy, M. Constantinou, J. R. Green, K. Hadjiyiannakou, K. Jansen, F. Manigrasso, A. Scapellato and F. Steffens, *Lattice continuum-limit study of nucleon quasi-PDFs*, Phys. Rev. D **103** (2021) 094512, arXiv: 2011.00964 [hep-lat].

[148] C. Alexandrou, S. Bacchio, K. Cichy, M. Constantinou, A. Sen, G. Spanoudes, F. Steffens and J. Tarello, *Collins-Soper kernel and reduced soft function from twisted mass lattice QCD*, In preparation (2024).

[149] C. Alexandrou, S. Bacchio, K. Cichy, M. Constantinou, A. Sen, G. Spanoudes, F. Steffens and J. Tarello, *Unpolarized transverse momentum dependent parton distribution functions from twisted mass lattice QCD*, In preparation (2024).